

University of Windsor

Scholarship at UWindor

Electronic Theses and Dissertations

Theses, Dissertations, and Major Papers

2013

An Investigation of a Diesel Liquid Injector in a Simulated Exhaust Flow

Shouvik Dev
University of Windsor

Follow this and additional works at: <https://scholar.uwindsor.ca/etd>

Recommended Citation

Dev, Shouvik, "An Investigation of a Diesel Liquid Injector in a Simulated Exhaust Flow" (2013). *Electronic Theses and Dissertations*. 4970.

<https://scholar.uwindsor.ca/etd/4970>

This online database contains the full-text of PhD dissertations and Masters' theses of University of Windsor students from 1954 forward. These documents are made available for personal study and research purposes only, in accordance with the Canadian Copyright Act and the Creative Commons license—CC BY-NC-ND (Attribution, Non-Commercial, No Derivative Works). Under this license, works must always be attributed to the copyright holder (original author), cannot be used for any commercial purposes, and may not be altered. Any other use would require the permission of the copyright holder. Students may inquire about withdrawing their dissertation and/or thesis from this database. For additional inquiries, please contact the repository administrator via email (scholarship@uwindsor.ca) or by telephone at 519-253-3000ext. 3208.

AN INVESTIGATION OF A DIESEL LIQUID INJECTOR IN A
SIMULATED EXHAUST FLOW

By

Shouvik Dev

A Thesis
Submitted to the Faculty of Graduate Studies
through the Department of Mechanical, Automotive and Materials Engineering
in Partial Fulfillment of the Requirements for
the Degree of Master of Applied Science at the
University of Windsor

Windsor, Ontario, Canada

2013

© 2013 Shouvik Dev

An Investigation of a Diesel Liquid Injector in a Simulated Exhaust Flow

by

Shouvik Dev

APPROVED BY:

Dr. R. Barron
Department of Mathematics and Statistics

Dr. B. Zhou
Department of Mechanical, Automotive and Materials Engineering

Dr. M. Zheng, Advisor
Department of Mechanical, Automotive and Materials Engineering

Dr. P. Henshaw, Advisor
Department of Civil and Environmental Engineering

11 September 2013

DECLARATION OF ORIGINALITY

I hereby certify that I am the sole author of this thesis and that no part of this thesis has been published or submitted for publication.

I certify that, to the best of my knowledge, my thesis does not infringe upon anyone's copyright nor violate any proprietary rights and that any ideas, techniques, quotations, or any other material from the work of other people included in my thesis, published or otherwise, are fully acknowledged in accordance with the standard referencing practices. Furthermore, to the extent that I have included copyrighted material that surpasses the bounds of fair dealing within the meaning of the Canada Copyright Act, I certify that I have obtained a written permission from the copyright owner(s) to include such material(s) in my thesis and have included copies of such copyright clearances to my appendix.

I declare that this is a true copy of my thesis, including any final revisions, as approved by my thesis committee and the Graduate Studies office, and that this thesis has not been submitted for a higher degree to any other University or Institution.

ABSTRACT

Certain exhaust after-treatment devices used in modern diesel engines need an injector to spray a liquid, including a fuel, into the exhaust stream. For optimum performance, it is desired that the liquid must atomize and vaporize before it enters the device. The spray of an after-treatment injector was simulated in a computational fluid dynamics (CFD) suite, and showed that evaporation increased with increase in the gas flow rate and gas temperature.

The results of the calculations were used to design an experimental setup to study a diesel after-treatment injector. Water was injected into air flowing with a speed of 1.4 m/s and at temperature of 423 K. High speed imaging and phase Doppler anemometry (PDA) were used to identify regions of high particle count. In these regions, diameter decreased with increasing vertical and horizontal distance from the injector. The vertical velocity of the particles was found to increase marginally with increasing vertical distance from the injector tip.

DEDICATION

To the wonderful family I am blessed with – my mother, father and sister.

ACKNOWLEDGEMENTS

I am deeply grateful to my thesis advisors, Dr. Ming Zheng and Dr. Paul Henshaw. Their guidance, wisdom, support, and encouragement have not only made this work possible but have also contributed immensely to my professional development.

I would like to thank my thesis committee members, Dr. Ronald Barron, Dr. Biao Zhou, and the Chair of Defense, for their insightful feedback.

I consider myself very fortunate to be a member of the Clean Diesel Engine Laboratory, University of Windsor. I would like to thank all my colleagues – Dr. Meiping Wang, Dr. Shui Yu, Dr. Tadanori Yanai, Xiaoye Han, Kelvin Xie, Marko Jeftic, Prasad Divekar, Tongyang Gao, Qingyuan Tan, Geraint Bryden, and Christopher Aversa for their support and feedback. I am grateful to Xiaoye Han for his invaluable advice during the design and build of the experimental setup. I would like to thank Kelvin Xie, Xiaoye Han, and Dr. Shui Yu for their help with setting up and running of the laser experiments. I would also like to thank Prasad Divekar for his assistance with the programming, control systems, and for the countless other ways he stepped up to help.

I am grateful to University of Windsor staff member Bruce Durfy for his assistance and advice during the machining and fabrication of the experimental setup.

I would like to thank Convergent Science for the use of their simulation suite. Furthermore, the Canada Research Chair program, NSERC, CFI, OIT, AUTO21, the University of Windsor, Ford Motor Company, and other OEMs are gratefully acknowledged for their support of the research at the Clean Diesel Engine Laboratory.

Finally, I would like to thank my family – my parents and my sister for their love and support. This work is dedicated to them.

TABLE OF CONTENTS

DECLARATION OF ORIGINALITY	iii
ABSTRACT	iv
DEDICATION	v
ACKNOWLEDGEMENTS	vi
LIST OF TABLES	x
LIST OF FIGURES	xi
LIST OF APPENDICES	xiv
LIST OF SYMBOLS AND ABBREVIATIONS	xv
1. INTRODUCTION	1
1.1. Background	1
1.2. Diesel After-treatment Technologies	5
1.2.1. Diesel oxidation catalyst (DOC).....	5
1.2.2. Diesel particulate filter (DPF)	6
1.2.3. Selective catalytic reduction (SCR).....	7
1.2.4. Lean NOx trap (LNT).....	7
1.3. Diesel After-treatment Injection.....	9
1.4. CONVERGE CFD Simulation.....	10
1.4.1. Stage I: Geometry input.....	10
1.4.2. Stage II: Simulation parameters	10
1.4.3. Stage III: Calculation and post-processing	10
1.5. Phase Doppler Anemometry (PDA).....	12
1.6. Structure of the Thesis.....	14
2. NUMERICAL ESTIMATION OF EVAPORATION	15

2.1. Droplet Atomization and Evaporation	15
2.2. Classical Evaporation Model	17
2.3. Results and Discussion.....	19
3. CFD SIMULATION STUDY	23
3.1. Objective of the Simulation Study	23
3.2. Simulation Parameters.....	23
3.3. Simulation Results.....	26
3.3.1. Effect of flow rate.....	27
3.3.2. Time progression of spray	30
3.3.3. Effect of increasing temperature.....	33
3.3.4. Velocity of droplets	35
3.3.5. Sauter mean diameter vs. time.....	40
4. EXPERIMENTAL SETUP	41
4.1. Test Chamber – Design and Construction.....	41
4.2. Injection System Setup.....	43
4.3. High Speed Imaging.....	48
4.3.1. Front illumination	48
4.3.2. Back illumination (diffuser screen photography).....	48
4.4. Coordinate System for PDA Measurement.....	51
4.5. Laser Setup for PDA and Data Acquisition	52
5. RESULTS AND DISCUSSION.....	56
5.1. High Speed Imaging.....	56
5.1.1. Front lit imaging	56
5.1.2. Back lit imaging.....	62
5.2. Phase Doppler Anemometry Tests with Water as Test Liquid	66

5.2.1. Time based results for X-direction sweep	67
5.2.2. Time based results for Z-direction sweep on the injector axis	72
5.2.3. Velocity distribution	74
5.2.4. Diameter distribution.....	77
5.2.5. Vertical velocity	79
5.3. Phase Doppler Anemometry Tests with Diesel as Test Liquid.....	82
6. CONCLUDING REMARKS	84
6.1. Summary of Results	84
6.2. Future Scope of Work	86
REFERENCES/BIBLIOGRAPHY.....	87
APPENDIX A: MATLAB code for calculation of steady state evaporation constant	91
APPENDIX B: Injector Driver and PDA Sync Program in LabView™	93
APPENDIX C: Data Acquisition Program in LabView™	94
VITA AUCTORIS	95
LIST OF PUBLICATIONS	96

LIST OF TABLES

Table 1.1. Outline of analytical and empirical studies presented in this thesis	14
Table 2.1. Factors affecting overall rate of evaporation [20]	15
Table 3.1. Simulation conditions	24
Table 3.2. Summary of simulation runs.....	26

LIST OF FIGURES

Figure 1.1. CAFE standard for passenger cars MY 2016-2025 [2]	2
Figure 1.2. CAFE standard for light trucks MY 2016-2025 [2]	3
Figure 1.3. EPA emission standards for heavy duty highway vehicles [5]	3
Figure 1.4. Diesel oxidation catalyst – cutaway section.....	5
Figure 1.5. Diesel particulate filter (DPF) in filtering mode	6
Figure 1.6. Lean NOx trap operating in adsorption mode (adapted from [9]).....	7
Figure 1.7. Lean NOx trap operating in regeneration mode (adapted from [9])	8
Figure 1.8. An after-treatment system layout with diesel fuel doser (adapted from [17]) .	9
Figure 1.9. CONVERGE – types of simulation parameters	11
Figure 1.10. Operating principle of PDA (image sourced from [19])	13
Figure 2.1. Evaporation of 100 μm n-heptane droplet with increasing temperature	20
Figure 2.2. Evaporation of 200 μm n-heptane droplet with increasing temperature	21
Figure 2.3. Evaporation of 100 μm DF-2 droplet with increasing temperature	21
Figure 2.4. Evaporation of 200 μm DF-2 droplet with increasing temperature	22
Figure 3.1. CONVERGE geometry input and coordinate system	25
Figure 3.2. Simulation time scale	27
Figure 3.3. Diameter distribution – 0 g/s, 10 ms, 423 K.....	28
Figure 3.4. Diameter distribution – 15 g/s, 10 ms, 423 K.....	28
Figure 3.5. Diameter distribution – 20 g/s, 10 ms, 423 K.....	29
Figure 3.6. Diameter distribution – 25 g/s, 10 ms, 423 K.....	29
Figure 3.7. Diameter distribution – 30 g/s, 10 ms, 423 K.....	30
Figure 3.8. Diameter distribution – 15 g/s, 15 ms, 423 K.....	31
Figure 3.9. Diameter distribution – 15 g/s, 20 ms, 423 K.....	31
Figure 3.10. Diameter distribution – 15 g/s, 25 ms, 423 K.....	32
Figure 3.11. Diameter distribution – 15 g/s, 30 ms, 423 K.....	32
Figure 3.12. Diameter distribution – 15 g/s, 30 ms, 473 K.....	33
Figure 3.13. Diameter distribution – 15 g/s, 30 ms, 523 K.....	34
Figure 3.14. Liquid mass in the chamber vs. simulation time	34
Figure 3.15. XZ-Velocity of air in the chamber – 15 g/s, 20 ms, 423 K	35
Figure 3.16. X-Velocity magnitude distribution – 0 g/s, 15 ms, 423 K.....	36

Figure 3.17. X-velocity magnitude distribution – 15 g/s, 15 ms, 423 K	37
Figure 3.18. X-velocity magnitude distribution – 30 g/s, 15 ms, 423 K	37
Figure 3.19. Z-velocity distribution – 0 g/s, 15 ms, 423 K.....	38
Figure 3.20. Z-velocity distribution – 15 g/s, 15 ms, 423 K.....	39
Figure 3.21. Time vs. Sauter mean diameter at different flow rates.....	40
Figure 4.1. CAD drawing of the finished chamber structure.....	42
Figure 4.2. Assembly of the optical window	43
Figure 4.3. Bosch Departronic System (Left: Shut-off and doser valve, Right: Injector) 45	
Figure 4.4. Water injection system	45
Figure 4.5. Pololu MD01B circuit diagram	46
Figure 4.6. LabVIEW front panel of injection control program.....	47
Figure 4.7. Delivery vs. injection duration	47
Figure 4.8. Front illuminated high speed imaging.....	49
Figure 4.9. Back illuminated high speed imaging	50
Figure 4.10. Measurement plane and coordinate system.....	52
Figure 4.11. Phase Doppler anemometry setup	54
Figure 4.12. Overall experimental setup for PDA	55
Figure 5.1. 6 ms – First appearance of liquid (Left: Without flow, Right: With flow)	57
Figure 5.2. 12 ms – Development of Cone (Left: Without flow, Right: With flow).....	58
Figure 5.3. 18 ms – Developed cone (Left: Without flow, Right: With flow)	58
Figure 5.4. 24 ms – Cone breakup (Left: Without flow, Right: With flow).....	59
Figure 5.5. 30 ms – Breakup and end of spray (Left: Without flow, Right: With flow) ..	59
Figure 5.6. 36 ms – Evaporation (Left: Without flow, Right: With flow).....	60
Figure 5.7. 42 ms – Evaporation (Left: Without flow, Right: With flow).....	60
Figure 5.8. 48 ms – Evaporation (Left: Without flow, Right: With flow).....	61
Figure 5.9. 54 ms – Evaporation (Left: Without flow, Right: With flow).....	61
Figure 5.10. 6 ms – First appearance of liquid (Left: Without flow, Right: With flow) ..	62
Figure 5.11. 12 ms – Development of cone (Left: Without flow, Right: With flow).....	63
Figure 5.12. 18 ms – Cone formation (Left: Without flow, Right: With flow)	63
Figure 5.13. 24 ms – Cone breakup (Left: Without flow, Right: With flow).....	64
Figure 5.14. 30 ms – Breakup and end of spray (Left: Without flow, Right: With flow) 64	

Figure 5.15. 36 ms – Evaporation (Left: Without flow, Right: With flow).....	65
Figure 5.16. 42 ms – Evaporation (Left: Without flow, Right: With flow).....	65
Figure 5.17. 48 ms – Evaporation (Left: Without flow, Right: With flow).....	66
Figure 5.18. Particle count at Z=30	67
Figure 5.19. Particle count at Z=0	68
Figure 5.20. Particle count at Z=70	69
Figure 5.21. Particle mean diameter at Z=70.....	71
Figure 5.22. Particle mean horizontal velocity at Z=70.....	71
Figure 5.23. Particle count at X=0 for Z=0 and Z=70	72
Figure 5.24. Particle mean diameter at X=0	73
Figure 5.25. Particle count at X=0	73
Figure 5.26. Horizontal velocity distribution at X=0 and time bin #1.....	74
Figure 5.27. Horizontal velocity distribution at X=40 and time bin #3.....	75
Figure 5.28. Mean horizontal velocity vs. X-coordinate at time bin #3	76
Figure 5.29. Mean horizontal velocity distribution at Z=70 and time bin #4.....	76
Figure 5.30. Particle mean diameter vs. X-coordinate at time bin#3	77
Figure 5.31. Particle mean diameter vs. X-coordinate at time bin#3	78
Figure 5.32. Particle mean diameter vs. X-coordinate at time bin#4	79
Figure 5.33. Particle count for Z-component at Z=50	80
Figure 5.34. Z-velocity distribution at X=30 and time bin #3	81
Figure 5.35. Z-velocity distribution at X=60 and time bin #3	81
Figure 5.36. Diesel PDA result – particle diameter distribution.....	82
Figure 5.37. Diesel PDA result – particle Z-velocity distribution.....	83

LIST OF APPENDICES

APPENDIX A: MATLAB code for calculation of steady state evaporation constant.....	91
APPENDIX B: Injector Driver and PDA Sync Program in LabView™	93
APPENDIX C: Data Acquisition Program in LabView™	94

LIST OF SYMBOLS AND ABBREVIATIONS

Symbols

λ	Incident wave length	[m]
λ_{st}	Steady state evaporation constant	[m ² /s]
θ	Beam intersection half angle	[radian]
ψ	Elevation angle	[radian]
φ	Scattering angle	[radian]
ρ	Fluid density	[kg/m ³]
ρ_F	Density of fuel at steady state temperature	[kg/m ³]
σ	Surface tension	[N/m]
bar g	Gauge pressure	[bar]
B	Steady state transfer number	[-]
B _M	Mass transfer number	[-]
B _T	Thermal transfer number	[-]
c _{Pg}	Specific heat at constant pressure for the vapor-gas mixture	[J/kg-K]
d _f	Fringe spacing	[m]
D ₀	Initial droplet diameter	[m]
D	Particle diameter	[m]
f _D	Doppler frequency	[s ⁻¹]
k _g	Steady state thermal conductivity of vapor-gas mixture	[W/m-K]

l	Characteristic length	[m]
L	Latent heat of vaporization	[J/kg]
M_A	Molecular mass of air	[g/mol]
M_F	Molecular mass of fuel	[g/mol]
n_{rel}	Refractive index	[-]
p	Ambient pressure	[N/m ²]
p_{Fs}	Vapor pressure at the surface of droplet	[N/m ²]
t	Time	[s]
T_∞	Ambient temperature	[K]
T_s	Drop surface temperature	[K]
v	Relative velocity between liquid and gas medium	[m/s]
We	Weber number	[-]
Y_{Fs}	Mass fraction of the fuel vapor at liquid surface	[-]

Abbreviations

CAFE	Corporate average fuel economy
CARB	California Air Resources Board
CPU	Central processing unit
CFD	Computational fluid dynamics
CFL	Courant–Friedrichs–Lewy (number)
DAQ	Data acquisition
DOC	Diesel oxidation catalyst
DPF	Diesel particulate filter
EGR	Exhaust gas recirculation
EPA	Environmental Protection Agency
fps	Frames per second
FPGA	Field programmable gated array
GB	Gigabyte
HC	Hydrocarbon
LAS	Laser absorption scattering
LDA	Laser Doppler anemometry
LED	Light emitting diode
LISA	Linearized instability sheet atomization
LNT	Lean NO _x trap
mpg	miles per gallon

MAF	Mass air flow (rate)
NI	National Instruments
NMHC	Non-methane hydrocarbon
NO _x	Oxides of nitrogen – NO and NO ₂
PDA	Phase Doppler anemometry
PIV	Particle image velocimetry
PM	Particulate matter
PWM	Pulse width modulation
PM	Particulate matter
RNG	Renormalized-group
RT	Real time
SCR	Selective catalytic reduction
SMD	Sauter mean diameter
TAB	Taylor analogy breakup
TKE	Turbulence kinetic energy

1. INTRODUCTION

1.1. Background

The diesel engine has been the mainstay for the commercial vehicle industry worldwide due to its superior fuel efficiency and torque delivery. Diesel passenger cars have also seen sales volumes comparable to gasoline powered vehicles in many parts of Europe and Asia. North American markets however, have only recently seen an interest in diesel passenger cars as a viable alternative to gasoline hybrid vehicles with similar or lower running costs. For manufacturers, fuel efficient diesels offer the opportunity to improve their corporate average fuel economy (CAFE). The CAFE regulations were introduced by the United States Congress in 1975 and have strived to improve the overall fuel efficiency of a manufacturer's vehicle fleet by putting penalties on exceeding the regulated limits [1]. The upcoming CAFE regulations for the period of 2016 to 2025 are shown in Figure 1.1 and Figure 1.2 for passenger cars and light trucks respectively [2]. The upper and lower thresholds correspond to the maximum permissible fuel consumption (expressed in miles per gallon) for the smallest and largest vehicle footprints respectively. The overall improvement in fuel efficiency targeted is at least 47 percent and 22 percent over ten years (2016-2025) for the largest passenger vehicles and trucks respectively.

On the other hand, the exhaust emission limits have seen drastic reductions over the past two decades. Emission control strategies generally require consumption of energy which leads to drop in the fuel efficiency. Unlike Europe, North American emission regulations set by the Environmental Protection Agency (EPA) and California Air Resources Board (CARB) do not broadly distinguish between gasoline and diesel engine emissions for passenger and light duty use [3-4]. Moreover, on-highway heavy duty diesel engines used in trucks and buses have to meet stringent nitrogen oxide (NO_x) and particulate matter (PM) emission regulations as well – which have traditionally been higher for diesel engines compared to gasoline engines. Figure 1.3 illustrates the NO_x, PM and hydrocarbon (HC) standards for heavy duty trucks over a 12 year period [5]. Meeting these emission standards has been possible through the development of a multitude of

strategies and technologies over the last decade. However, as these technologies mature, the focus of manufacturers and researchers has shifted to strategies aimed at minimizing the impact of emission control on fuel economy and cost of the vehicle [5-7]. For instance, programs such as the United States Department of Energy’s “SuperTruck” aim to demonstrate a 50% improvement in the overall freight efficiency of the Class 8 tractor-trailer category of trucks [8]. The success of such programs and achievement of CAFE targets hinges on the optimization of all vehicle systems including emission control.

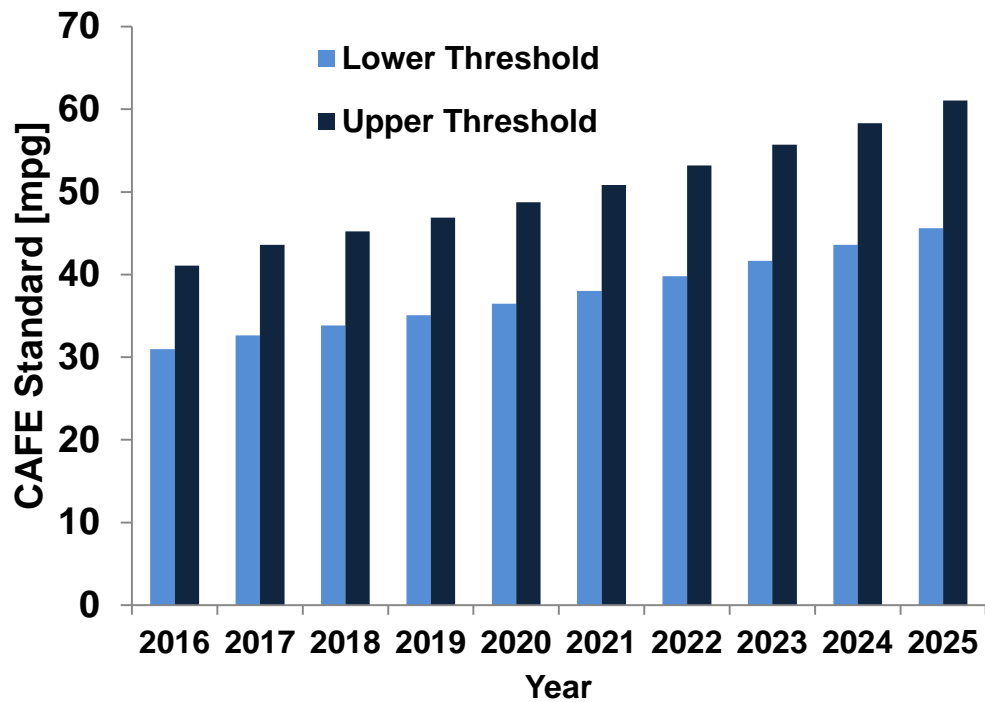


Figure 1.1. CAFE standard for passenger cars MY 2016-2025 [2]

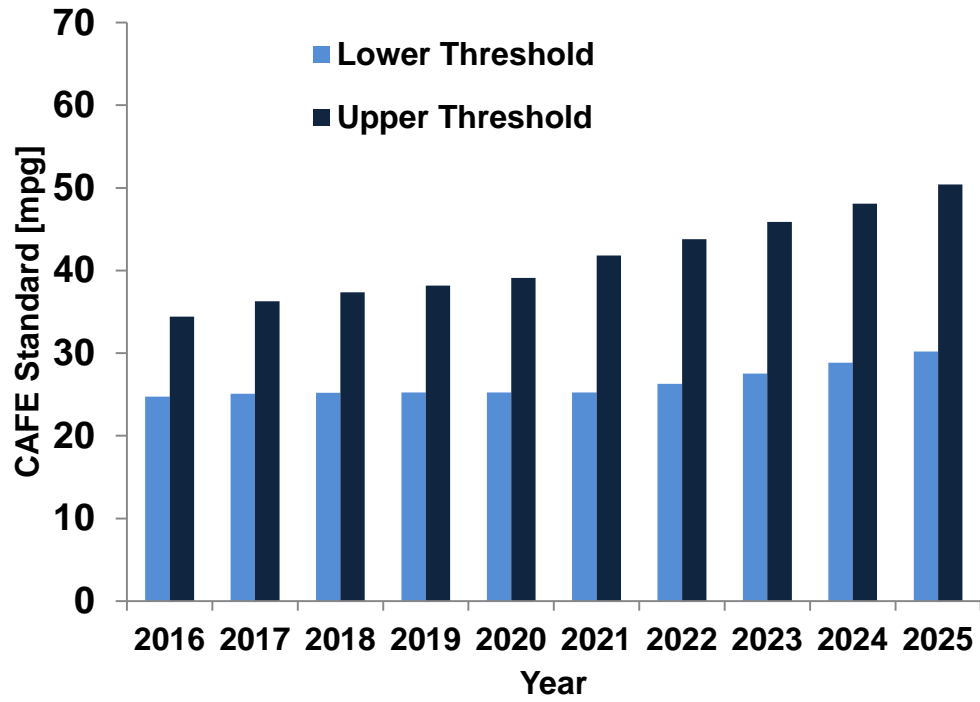


Figure 1.2. CAFE standard for light trucks MY 2016-2025 [2]

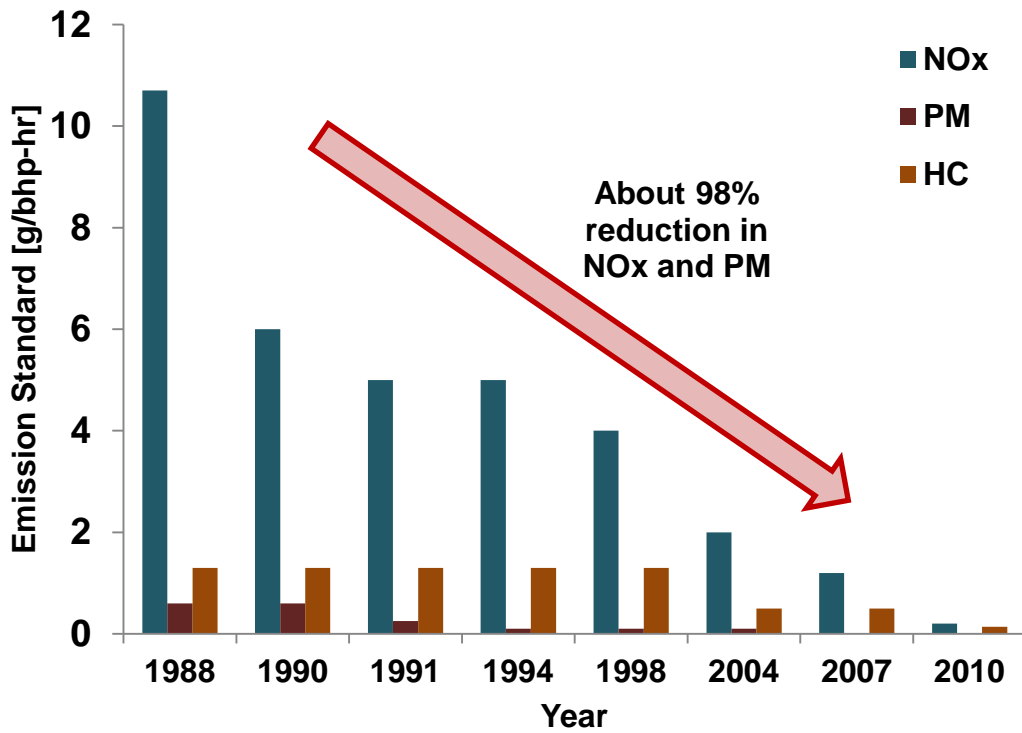


Figure 1.3. EPA emission standards for heavy duty highway vehicles [5]

The diesel emission control strategies can be divided into two categories – in-cylinder and exhaust after-treatment [9]. In-cylinder technologies include advanced fuel and air management systems incorporating engine hardware such as variable valve timing (VVT), exhaust gas recirculation (EGR), and dual fuels. Exhaust after-treatment technologies include the diesel particulate filter (DPF), diesel oxidation catalyst (DOC), selective catalytic reduction (SCR), and lean NO_x trap (LNT). Modern diesel engines use a combination of these technologies.

The diesel exhaust after-treatment often requires supplemental injection of diesel or a water-based urea solution into the exhaust stream to control NO_x and/or PM. The focus of this study is the behaviour of a diesel after-treatment injector. The liquid spray discharged by the injector is affected by the velocity and temperature of the flowing exhaust gas. The objective therefore, is to study the properties of the combined flow, which results from this interaction between the liquid and gas phases. In the exhaust stream, the injected liquid atomizes into particles which are expected to be suspended in the flow. Eventually, the liquid particles reduce in size and finally vaporize. By measuring the liquid droplet diameter and velocity over a length, downstream from the point of injection, the extent of the evaporation can be estimated.

The understanding of liquid evaporation in the exhaust is of utmost importance in the design of efficient after-treatment systems. The fuel should atomize and vaporize completely before reaching the after-treatment device in order to avoid hot spots, or the fuel passing through the device untreated, leading to HC emissions. Conditions for proper vaporization will be more difficult to achieve as petroleum based diesel fuels are blended with low volatility biodiesel fuels. Moreover, like any aspect of automotive design, there are packaging constraints for the exhaust after-treatment system. Finally, with increasingly stringent fuel consumption standards, the design of the system has to be optimized so that the fuel penalty is minimized.

Subsequent sections briefly describe the diesel after-treatment technologies as well as the simulation and empirical tools used in this study.

1.2. Diesel After-treatment Technologies

1.2.1. Diesel oxidation catalyst (DOC)

A diesel oxidation catalyst is primarily used to oxidize the hydrocarbons and carbon monoxide in the diesel exhaust stream. These hydrocarbons have either been injected in the cylinder or in the exhaust stream. A secondary purpose is to convert the nitrogen monoxide (NO) in the exhaust stream to nitrogen dioxide (NO₂). Increasing the composition of NO₂ in the exhaust stream is found to improve the performance of subsequent NO_x reduction systems such as SCR and LNT. Furthermore, the oxidation of the hydrocarbons raises the temperature of diesel exhaust, which is typically much lower than that of gasoline exhaust. The elevated temperature facilitates destruction of NO_x and soot further downstream. DOCs usually use precious metals like platinum, or palladium as a catalyst [10-11]. The catalyst is dispersed in a high surface area wash coat such as alumina (Al₂O₃) that is supported on a honeycomb monolith usually made of ceramic. Figure 1.4 illustrates a section of the DOC honeycomb structure.



Figure 1.4. Diesel oxidation catalyst – cutaway section

1.2.2. Diesel particulate filter (DPF)

A diesel particulate filter is used to capture and destroy the particulate matter in the diesel exhaust. A conventional DPF operates alternately between two modes – filtration and regeneration [12-13]. The most commonly used DPF is the wall-flow monolith made of ceramic. This consists of parallel channels, half of which are blocked in the downstream end and half are blocked in the upstream end (Figure 1.5). In the filtration mode, the exhaust is forced to flow through the porous walls of the filter thereby capturing the particulate matter on the wall surface. The pressure drop across the filter is monitored to determine when sufficient particles have accumulated in the filter. The regeneration mode is initiated during which the particles are combusted by increasing the temperature of the exhaust. This heat energy is provided by burning fuel. In a typical configuration, the DPF might be located after the DOC so that the DOC can raise the exhaust gas temperature.

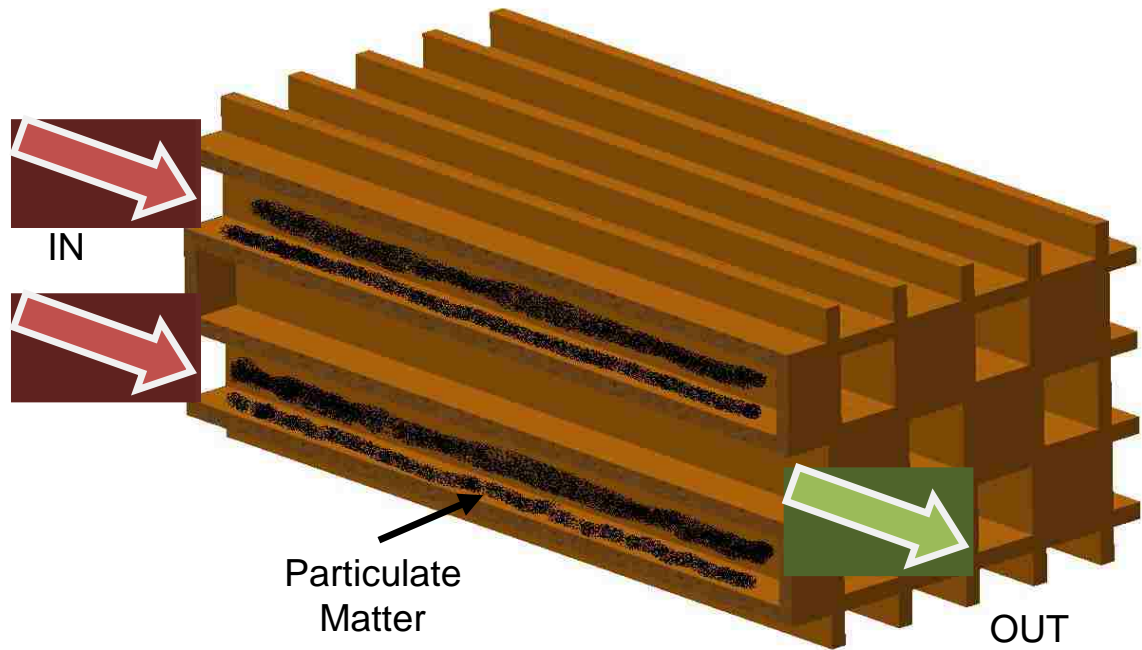


Figure 1.5. Diesel particulate filter (DPF) in filtering mode

1.2.3. Selective catalytic reduction (SCR)

The selective catalytic reduction device reduces NO_x to inert nitrogen and water using a reducing agent such as ammonia (NH₃) or fuel hydrocarbon. For the former, there are two ways to introduce ammonia into the exhaust. In an ammonia-SCR unit, urea solution is sprayed into the exhaust stream (typically a 32% urea and 68% water by volume solution) [14-15]. When heated, the urea solution breaks up into carbon dioxide and ammonia. In a hydrocarbon-SCR unit, fuel is injected into the exhaust stream which is used to generate carbon monoxide and hydrogen [16]. The CO and H₂ can then be used to generate ammonia during the lean NO_x trap (LNT) regeneration. Thus, fuel can be used directly to reduce NO_x. The SCR convertor typically consists of a ceramic structure with zeolites, precious metals, or metal oxides as the active catalyst.

1.2.4. Lean NO_x trap (LNT)

The lean NO_x trap is used to capture and destroy NO_x in the exhaust. It operates in two modes – adsorption mode and regeneration mode [9]. In the adsorption mode, NO_x reacts with a metal oxide such as barium oxide (BaO) to form a nitrate – barium nitrate (Ba(NO₃)₂) on the reactor surface. This way, the NO_x is ‘trapped’ in the LNT device. As more NO_x is stored, the number of storage sites reduces and more NO_x passes through the LNT untreated (NO_x slip).

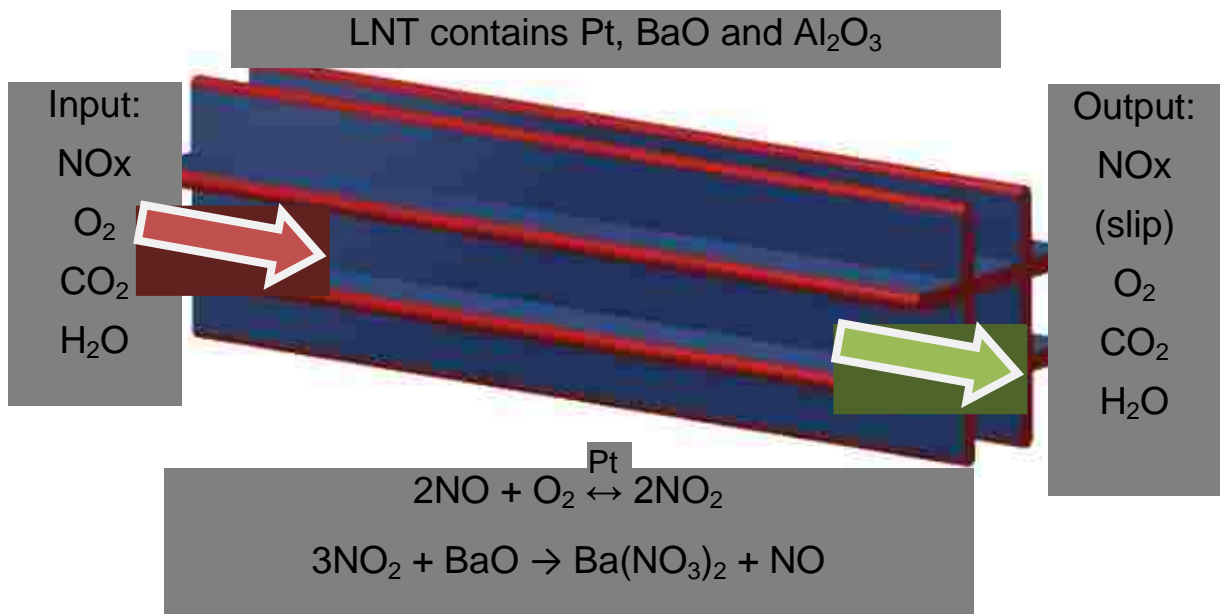


Figure 1.6. Lean NO_x trap operating in adsorption mode (adapted from [9])

To free up the storage sites, the LNT switches to regeneration mode. Regeneration requires fuel supplied either through a late in-cylinder injection or in the exhaust stream. This fuel reacts with the barium nitrate in the presence of a precious metal catalyst to finally produce nitrogen and barium oxide. In this way, the regeneration restores the barium oxide storage sites for NOx entrapment again. Figure 1.6 and Figure 1.7 illustrate the LNT reaction chemistry during the two modes.

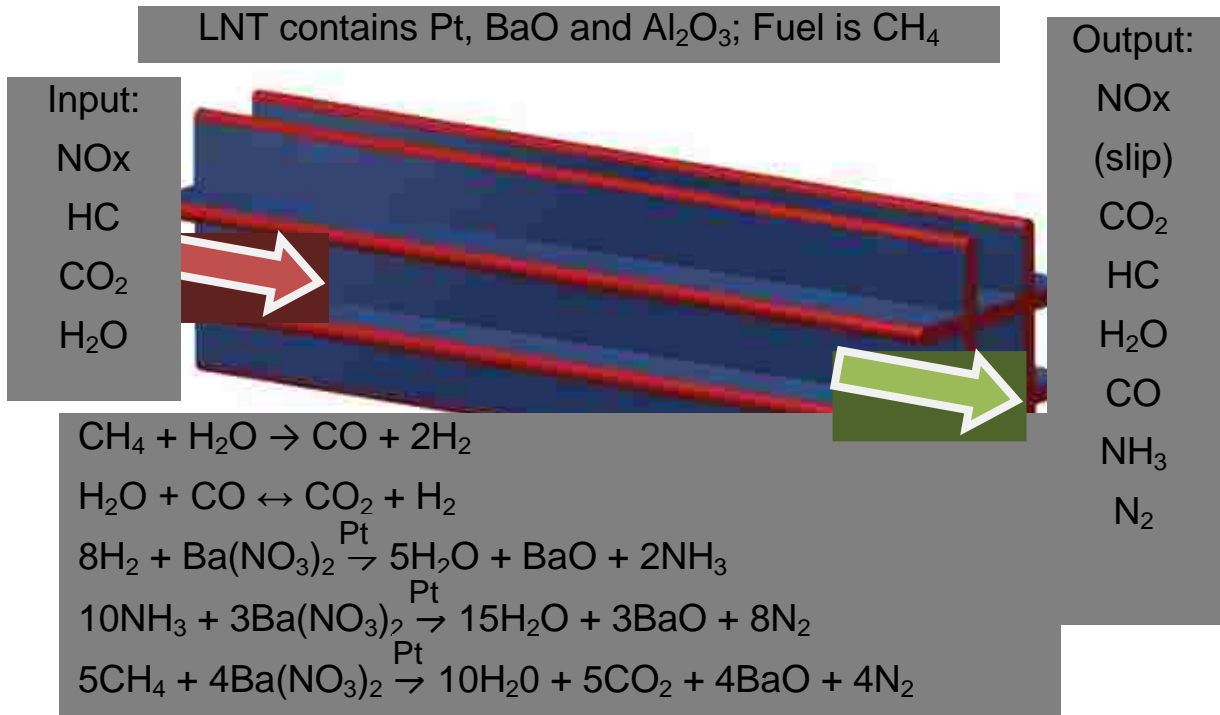


Figure 1.7. Lean NOx trap operating in regeneration mode (adapted from [9])

1.3. Diesel After-treatment Injection

From section 1.2, it is evident that the fuel plays an important role in the functioning of after-treatment devices of a modern diesel engine powertrain. Again, there are two ways to introduce the fuel into the exhaust stream – either in-cylinder or directly into the exhaust stream. This work focuses on injection into the exhaust stream.

The injection of a liquid or gaseous substance into the exhaust is also known as dosing. Dosing has two primary purposes – to raise the temperature of the exhaust gas, and / or introduce a chemical reagent. As an example, a fuel-based after-treatment system may be configured as shown in Figure 1.8 [17]. This approach does not require a separate system to deliver urea solution and instead utilizes the onboard fuel supply. It consists of a fuel dosing system, pipes to aid mixing, followed by a fuel reformer. The fuel reformer generates hydrogen and carbon monoxide from the diesel. The hydrogen and carbon monoxide are used to reduce the NO_x stored as nitrates in the LNT. During this LNT regeneration, ammonia is released which is utilized subsequently in the SCR unit downstream. The added advantage of a LNT-SCR system is that the NO_x which inevitably slips during the LNT regeneration can be treated in the SCR. The fuel reformer also manages the exhaust temperature to regenerate the DPF located between the LNT and SCR.

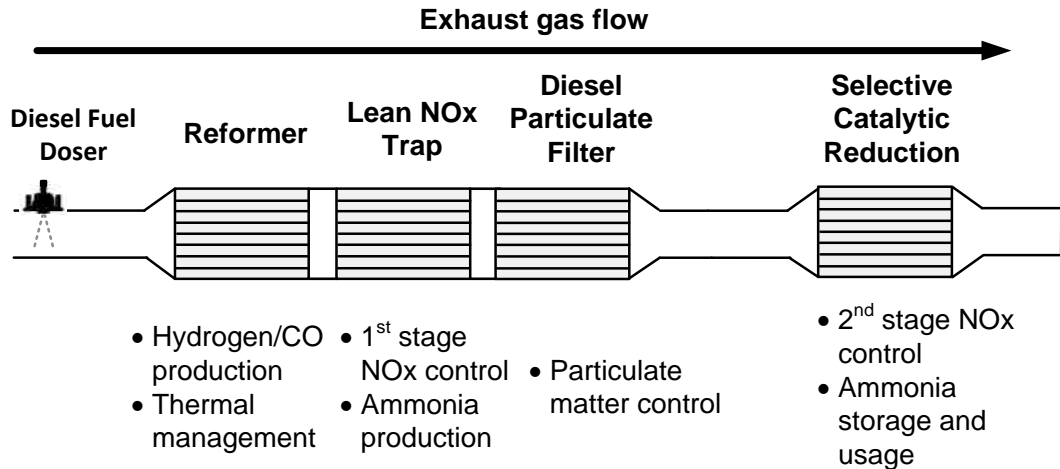


Figure 1.8. An after-treatment system layout with diesel fuel doser (adapted from [17])

1.4. CONVERGE CFD Simulation

CONVERGE is a widely used commercially available computational fluid dynamics (CFD) suite developed by Convergent Science, Inc. Various types of steady state and transient multi-phase fluid flows can be simulated. CONVERGE version 1.4 was used to simulate the spray and provide a basis to design a system to measure the spray using PDA. The simulation workflow can be divided into three stages described below [18].

1.4.1. Stage I: Geometry input

The geometry defines the boundaries which contain the fluids. A 3-dimensional CAD model representing the surfaces of the experimental setup is created. Features which do not affect the fluid flow are excluded from the model. The pre-processor program divides the entire surface into triangular 2-dimensional cells. Further, the cells must be assigned boundaries which represent distinct features such as inflow and outflow surfaces. The pre-processor program generates a mesh from the surface file and stores the coordinates into a data file.

1.4.2. Stage II: Simulation parameters

Simulation calculations are based on mathematical models. The mathematical models to be used, their parameters, initial and boundary conditions are all defined in this stage. Figure 1.9 shows a diagram of the various inputs that were required to simulate the experimental conditions of this study.

1.4.3. Stage III: Calculation and post-processing

The CFD solver balances the mass, momentum, and energy across the mesh and generates output files with the calculation results. The results can be analyzed graphically in MATLAB. In this study, for instance, the spray calculation results can be analyzed to determine the spray particle velocity and diameter, and estimate the spray evaporation.

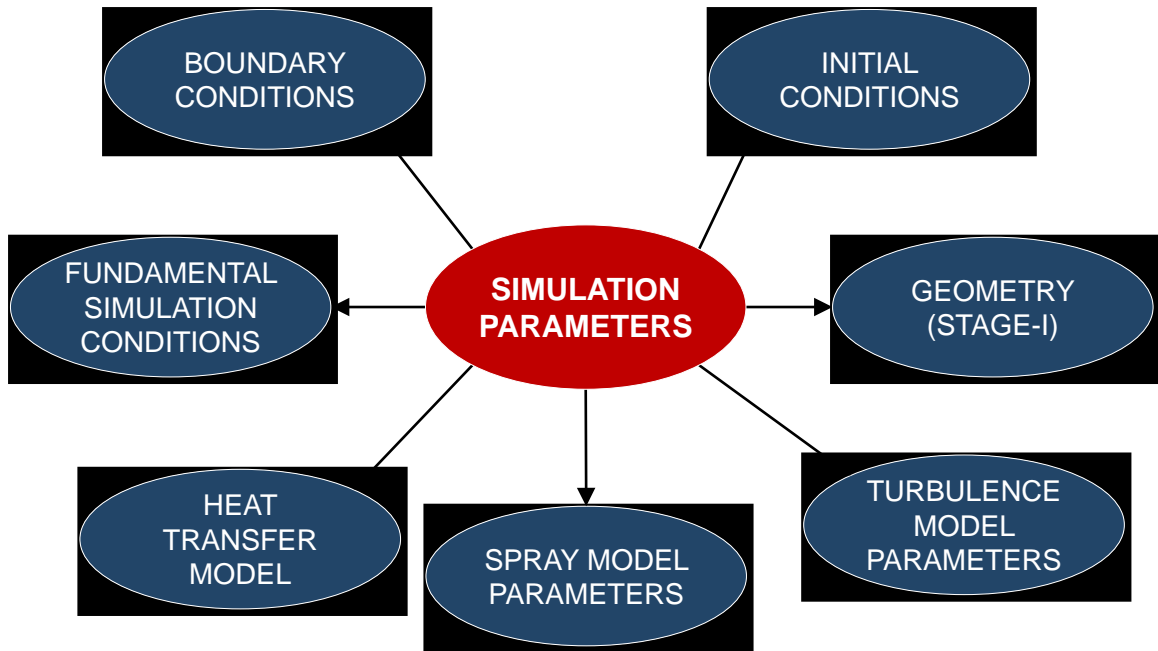


Figure 1.9. CONVERGE – types of simulation parameters

1.5. Phase Doppler Anemometry (PDA)

Phase Doppler Anemometry is a widely accepted, non-intrusive optical measurement technique used to measure the size and velocity of non-opaque spherical particles [1918]. Two coherent, collimated and monochromatic laser beams intersect to produce an interference pattern in the form of light and dark fringes. This pattern forms what is called the measurement volume. When a particle passes through this measurement volume, the frequency of the scattered light is proportional to the velocity component of the particle coplanar with the laser beams. To measure the diameter, two or three detectors are placed at different angles. Each detector receives the light signal at a different phase. The phase shift between the signals is proportional to the diameter of the particle. PDA has been used to make point by point measurements of the diameter and velocity of water, and diesel particles. Figure 1.10 illustrates the operating principle of PDA.

The fringe spacing, d_f , is defined as –

$$d_f = \frac{\lambda}{2} \sin \theta \quad (1.1)$$

where λ is the wave length and θ is the half-angle between two laser beams.

The Doppler frequency f_D provides information about the time required by the particle to cross one fringe spacing. This gives the velocity of the particle as –

$$V = d_f / \text{time} = d_f * f_D \quad (1.2)$$

If the light scattering is dominated by reflection, the phase of the signal is given by the relation –

$$\Phi = \frac{2\pi D}{\lambda} \times \frac{\sin \theta \sin \psi}{\sqrt{(2(1 - \cos \theta \cos \psi \cos \phi))}} \quad (1.3)$$

If the light scattering is dominated by refraction, the phase of the signal is given by the relation –

$$\Phi = \frac{-2\pi D}{\lambda} \frac{n_{rel} \sin \theta \sin \psi}{\sqrt{(2(1 + \cos \theta \cos \psi \cos \varphi)(1 + n_{rel}^2 - n_{rel}(\sqrt{2(1 + \cos \theta \cos \psi \cos \varphi)}))}} \quad (1.4)$$

where D , λ , θ , ψ , φ , n_{rel} refer to particle diameter, incident light wavelength, beam intersection half angle, elevation angle, scattering angle, and refractive index respectively (refer to Figure 1.10).

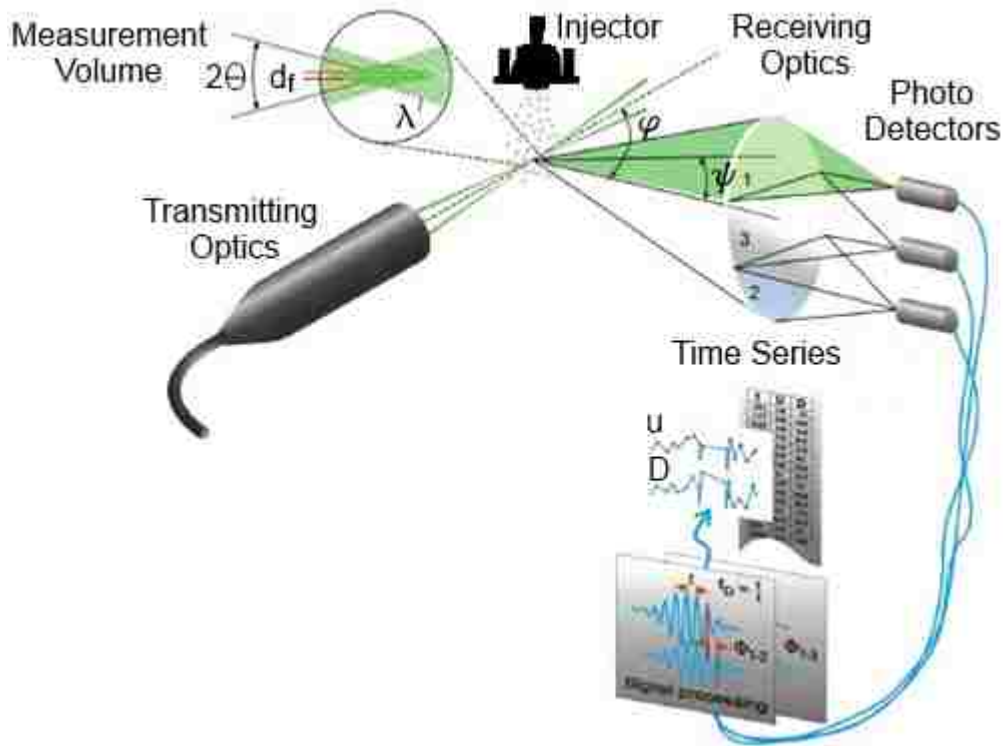


Figure 1.10. Operating principle of PDA (image sourced from [19])

The pre-conditions for application of PDA include an experimental setup with at least two directions of optical access. Moreover, the particles should be spherical and the refractive indices of the particle and the medium have to be known. Particle sizes usually range from $0.5 \mu\text{m}$ to a few millimeters.

1.6. Structure of the Thesis

This study is divided into two parts – analytical, and empirical. In the analytical part, evaporation models, a fundamental evaporation calculation, and a review of select literature on the spray breakup and evaporation are presented in Chapter 2. Taking the analysis further, the computational fluid dynamics (CFD) suite CONVERGE™ was used as a design tool to evaluate the experimental setup and conditions. The CFD study is described in Chapter 3, in which various flow conditions were simulated to study the impact on the fuel spray. Chapter 4 describes the optically accessible experimental setup which was designed and built to study a diesel after-treatment liquid injection subject to heated gas flow to simulate engine exhaust conditions. High speed imaging was used to make a qualitative assessment of the spray. Measurements were performed using Phase Doppler anemometry (PDA). The empirical results are described in Chapter 5. The analytical and empirical studies presented in this thesis are outlined in Table 1.1.

Table 1.1. Outline of analytical and empirical studies presented in this thesis

Test liquid	Gas flow condition	CFD simulation	High speed imaging	PDA measurement
Water	With flow	×	✓	✓
	Without flow	×	✓	×
Diesel (or surrogate)	With flow	✓	×	×
	Without flow	✓	×	✓

2. NUMERICAL ESTIMATION OF EVAPORATION

2.1. Droplet Atomization and Evaporation

In an after-treatment setup, the fuel should be completely vaporized and mixed with the exhaust gas for optimal performance. During evaporation, there is a transfer of both mass and heat simultaneously between the gas and liquid phases [20]. The liquid phase absorbs heat from the surrounding gas through conduction and convection. As it evaporates, the vapor mass mixes with the gas phase through convection and diffusion. Table 2.1 summarizes the factors which determine the overall rate of evaporation.

Table 2.1. Factors affecting overall rate of evaporation [20]

Gas Phase	Liquid Phase	Others
Pressure Temperature Transport properties such as flux, diffusion, thermal conductivity, viscosity	Temperature Volatility Diameter of drops	Velocity of liquid drops relative to the gas

The general purpose of an injector is to produce a liquid structure from which drops can break off easily. Larger liquid structures break up into smaller ones through the process of atomization. Evaporation is a surface phenomenon. Atomization increases the available surface area the liquid is exposed to, and therefore increases the transfer of heat [20].

Spray breakup and evaporation have been extensively studied over the years. Empirical studies on sprays generally involve optical techniques such as PDA, LDA, particle image velocimetry (PIV), and high speed imaging. Husted *et al* compared PIV and PDA droplet velocity measurement techniques on water mist nozzles [21]. Nishida *et al.* studied spray and mixture properties of an evaporating diesel fuel spray using ultraviolet-visible laser absorption scattering (LAS) technique [22]. Daviault *et al.* characterized a hollow cone spray of diesel proof oil using PDA [23].

Studies on cross-flow of gas with respect to the injector axis have been limited. Kitamura and Takahashi investigated the stability of different types of liquid jets subjected to a perpendicular air flow using high speed imaging [24]. They found that the breakup length – that is, the distance from the tip of the jet to the point at which the jet starts to disintegrate, reduces with increasing air velocity. It was concluded that the effect of air flow on the jet stability increases as its Weber number increases, defined by –

$$We = \frac{\rho v^2 l}{\sigma} \quad (2.1)$$

where ρ , v , l , and σ are the fluid density, relative velocity, characteristic length and surface tension respectively. A study on mono-dispersed droplets in a cross-flow air stream was performed by Park *et al* using PDA and high speed imaging [25]. The increasing Weber number was found to increase the deformation rate of a droplet during the initial breakup stage.

Studies on after-treatment injection have focused on design optimization. Jeong *et al.* examined a low pressure diesel after-treatment injector under different supply pressures using laser diffraction and high speed imaging [26]. Bamber *et al.* reported on the development of an exhaust fuel injection system for use in a comprehensive after-treatment system such as the one described in Section 1.3 [17].

A variety of mathematical models on evaporation have also been proposed. Their accuracy and applicability, however, is subject to debate. Chin *et al.* developed calculation procedures for estimating the steady state value of the evaporation constant and the length of heat-up period for a number of liquid hydrocarbon fuels [27]. Over the length of the heat-up period, a drop attains a uniform temperature and reaches a steady state at which point all the heat transfer into the drop is used to vaporize the liquid. Abramzon and Sirignano proposed a droplet vaporization model for combustion calculations in which they countered the assumptions of a unitary Lewis number (implying thermal diffusivity is equal to mass diffusivity), and that transfer effects on a moving droplet are regarded the same as a stagnant one [28]. Chrigui *et al.* presented a model combining the Abramzon-Sirignano evaporation model with other sub-models

such as dispersion and turbulence by using the Eulerian-Lagrangian approach. The model was validated through Laser / Phase Doppler Anemometry (LDA/PDA) tests [29]. Kryukov *et al.* point out that most CFD codes use hydrodynamic models in which the vapor on the surface of the droplet is saturated [30]. They claimed that a kinetic model represents the mass transfer between the liquid and gas more accurately compared to hydrodynamic models.

Despite its shortcomings, the classical evaporation model originally based on the works of Godsave and Spalding can be used to make a reasonable estimate of the lifetime of a fuel drop [31-32]. The following sections describe the methodology and calculations of a simplified mathematical model to estimate the evaporation rate. Certain relationships in the model have been derived empirically. Hence, it can be applied to a limited number of hydrocarbon fuels only.

2.2. Classical Evaporation Model

The classical evaporation theory, also known as the ‘D² law’ relates the reduction of droplet diameter to time under steady state conditions as –

$$D_0^2 - D^2 = \lambda_{st} t \quad (2.2)$$

where D_0 , D , t , and λ_{st} are the initial droplet diameter, the droplet diameter after a time period t , and steady state evaporation constant respectively.

The following assumptions are made for the calculation of the steady state evaporation constant [29] –

- Drop is spherical
- Fuel is a pure liquid having a well-defined boiling point
- Radiation heat transfer is negligible
- Secondary atomization and coalescence of droplets are neglected
- No influence of surface tension – uniform pressure around the droplet
- Uniform physical properties of the surrounding fluid and liquid-vapor thermal equilibrium on the droplet surface

- Ambient air is not soluble in the droplet fluid
- No chemical reactions

The calculation procedure stated herein has been explained by Lefebvre [20]. As stated earlier, the results are applicable to only certain hydrocarbons or hydrocarbon fuel blends such as n-heptane or diesel oil (DF-2) since certain equations have been derived empirically.

In the equations below, p is the ambient pressure, p_{Fs} is the vapor pressure at the surface of the droplet, M_A is the molecular mass of air, M_F is the molecular mass of fuel, Y_{Fs} is the mass fraction of the fuel vapor at liquid surface, T_∞ is the ambient temperature, T_s is the drop surface temperature, L is the latent heat of vaporization, B is the steady state transfer number, B_M is the mass transfer number, B_T is the thermal transfer number, k_g is the steady state thermal conductivity of the vapor-gas mixture, ρ_F is the density of fuel at steady state temperature, c_{Pg} is the specific heat at constant pressure for the vapor-gas mixture.

The objective of this calculation is to estimate the steady state evaporation constant, λ_{st} , for a single droplet of fuel. The thermal transfer number, B_T , is the ratio of the available enthalpy to the heat required to evaporate the fuel. The mass transfer number, B_M , is the ratio of the mass fraction of the fuel vapor to mass fraction of the liquid fuel. At the steady state condition, the entire heat transfer is used to vaporize the fuel. Therefore –

$$B_M = B_T = B \quad (2.3)$$

The fuel mass fraction is calculated initially from –

$$Y_{Fs} = \left[1 + \frac{M_A}{M_F} \left(\frac{p}{p_{Fs}} - 1 \right) \right]^{-1} \quad (2.4)$$

Next, the mass transfer number can be calculated by –

$$B_M = \frac{Y_{Fs}}{1 - Y_{Fs}} \quad (2.5)$$

Finally, the thermal transfer number is –

$$B_T = \frac{c_{Pg}(T_\infty - T_s)}{L} \quad (2.6)$$

B_M and B_T are calculated over a range of values from below and up to the boiling point of the fuel and each are plotted with respect to temperature on a single graph. The point where the plots meet is $B_M = B_T = B$ (transfer number) and the temperature at that point is the steady state temperature at the surface of the fuel droplet.

With ‘B’ known, the steady state evaporation constant can be calculated as –

$$\lambda_{st} = \frac{8k_g \ln(1+B)}{c_{Pg}\rho_F} \quad (2.7)$$

The steady state evaporation constant was calculated for two fuels, n-heptane and DF-2 at four ambient temperatures – 423 K, 473 K, 523 K, and 573 K. Two initial droplet diameters of 100 μm , and 200 μm were assumed. It is to be noted that the value of evaporation constant does not depend on the initial diameter assumed.

2.3. Results and Discussion

Equation 2.2 was used to estimate the time required for the mass of a droplet of fuel to reduce by 90%. Figure 2.1 and Figure 2.2 show the droplet lifetime plots for n-heptane with initial droplet diameters of 100 and 200 μm , respectively. As the ambient temperature increases, the droplet lifetime reduces. For the given temperature range of 423 to 573 K, the lifetime of the 100 μm droplet reduces from approximately 90 to 40 ms. The 200 μm drop takes approximately 380 to 180 ms to evaporate.

For the heavier diesel (DF-2) fuel, a sharp fall in droplet lifetime is calculated beyond 423 K (Figure 2.3 and Figure 2.4). The 100 μm DF-2 droplet has a lifetime between 225 to 50 ms while the 200 μm droplet has a lifetime between 900 to 200 ms.

To put these results into perspective of an after-treatment system, a flow speed of 1 m/s at 423 K would require a 200 μm DF-2 droplet to travel 0.9 m (0.9 s X 1 m/s) for it to evaporate. The more the flow speed and higher the temperature, lower the time required

for the fuel to evaporate. The exhaust flow speed and temperature can be determined for a given engine, engine speed, and load. The injector characteristics (such as droplet distribution, cone angle) can be evaluated. From a design perspective, a conservative estimate of the length of the after-treatment system can be derived to allow complete evaporation of the fuel.

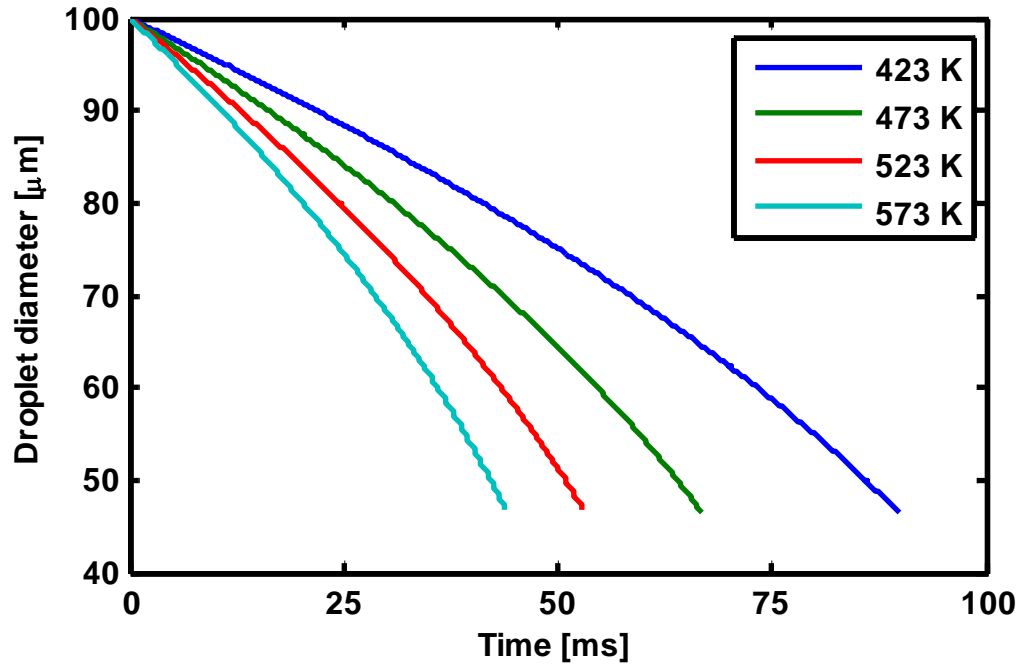


Figure 2.1. Evaporation of 100 μm n-heptane droplet with increasing temperature

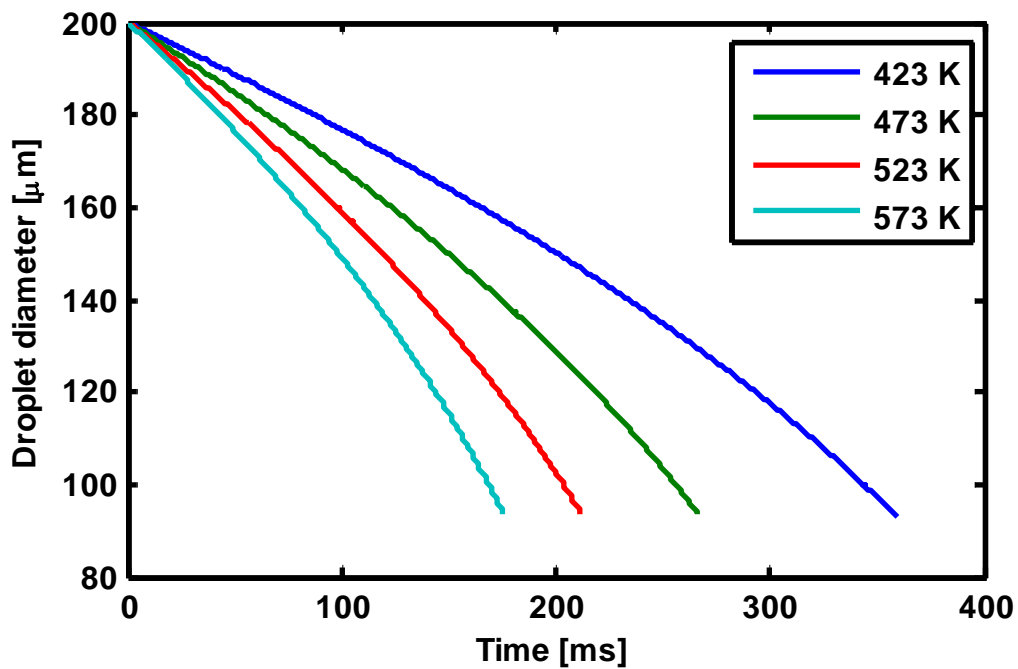


Figure 2.2. Evaporation of 200 μm n-heptane droplet with increasing temperature

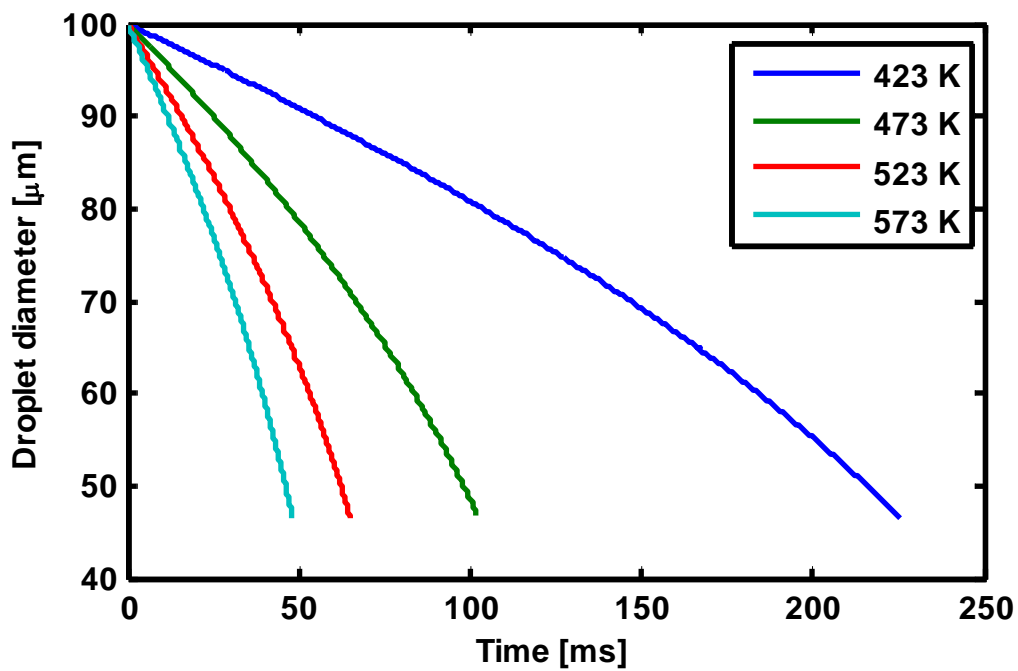


Figure 2.3. Evaporation of 100 μm DF-2 droplet with increasing temperature

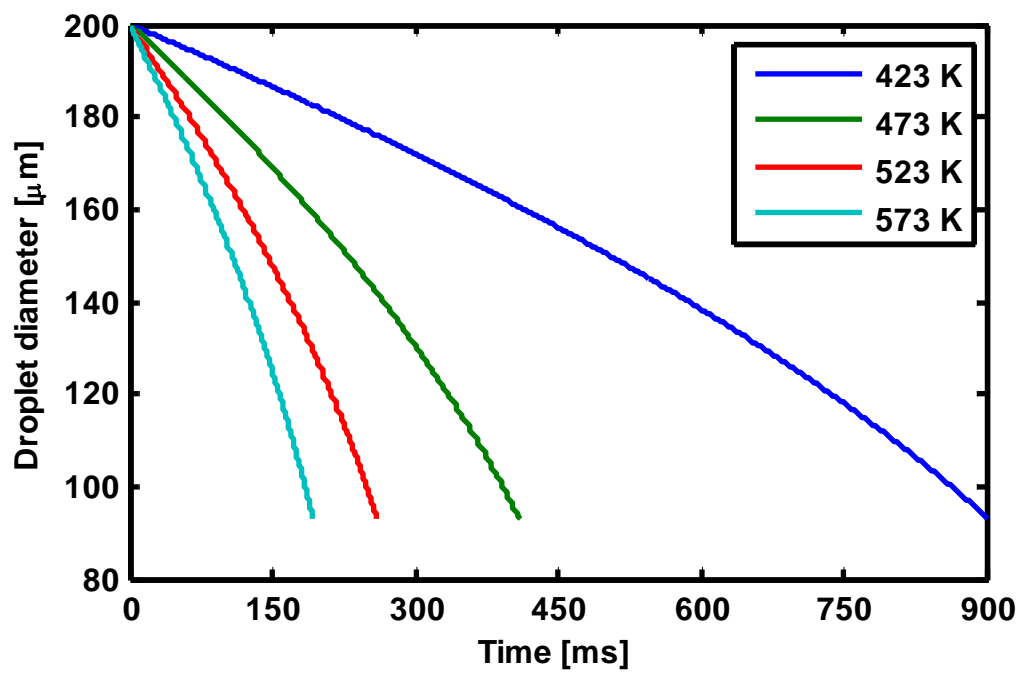


Figure 2.4. Evaporation of 200 μm DF-2 droplet with increasing temperature

3. CFD SIMULATION STUDY

3.1. Objective of the Simulation Study

The CONVERGE CFD suite was used to evaluate the design of the experimental setup and get an understanding of how the spray would react to a cross-flow of gas and change in the gas temperature. The simulated flow and temperature conditions were set to within the constraints of the experimental setup envisioned.

3.2. Simulation Parameters

The CONVERGE solver was run in transient mode for time-based output. The total simulation time period was set to 80 ms. n-Heptane was used as the liquid phase – it being a popular choice as a diesel surrogate. Simulation times of greater than 80 ms were considered unnecessary as the spray was found to evaporate completely within that time period for all test cases. The major simulation parameters are summarized in Table 3.1.

The geometry input was based on the test chamber design which would provide significant optical access to observe and measure the spray. The geometry file used to generate the mesh is shown in Figure 3.1. ‘P1’ represents the origin and the location of the injector. The coordinate axes and the direction of flow are indicated in the figure as well. The flow into the chamber (through the dark yellow colored boundary) was treated as steady and laminar. Hence, the initial and boundary conditions for turbulent kinetic energy and turbulent energy dissipation were assumed to be zero.

The conservation equations were solved using finite volume method with second order upwind scheme. The convergence tolerance was 10^{-4} for momentum and density, 10^{-7} for pressure, and 10^{-3} for turbulent kinetic energy and turbulent energy dissipation. The minimum and maximum calculation time steps were 0.05 and 5 μ s respectively. The simulation code adjusted the time step between the minimum and maximum value based on the Courant–Friedrichs–Lewy (CFL) number.

The injector used in this study was a Bosch Departronic2 diesel fuel injector which produced a hollow cone of liquid with a 43 degree cone angle. The cone angle and the

injection model inputs were based on the data provided by the OEM (original equipment manufacturer) and the measurements made in the author's laboratory. CONVERGE uses two droplet breakup models for hollow cone sprays. Linearized instability sheet atomization (LISA) is used to model the breakup of liquid sheets into ligaments of liquids. Taylor analogy breakup (TAB) is used to model breakup of the ligaments into smaller particles [18].

The renormalized-group (RNG) k- ϵ model was used to model the air flow.

Table 3.1. Simulation conditions

Parameter	Value	Unit
Simulation run time	80	ms
Calculation minimum dt	0.05	μ s
Calculation maximum dt	5	μ s
Output file generation frequency	2	s ⁻¹
Computational cell size	5 X 5 X 5	mm
Total computational cells	41756 (generated by pre-processor)	-
Turbulence model	RNG k- ϵ	-
Initial turbulent kinetic energy	0	m ² /s ²
Initial turbulent energy dissipation	0	m ² /s ³
Initial and boundary pressure	101325	N/m ²
Initial and boundary temperature	423 / 473 / 523	K
Boundary inflow	0 / 15 / 20 / 25 / 30	g/s
Boundary turbulent kinetic energy	0	m ² /s ²
Boundary turbulent energy dissipation	0	m ² /s ³
Injection species	n-heptane (C ₇ H ₁₆)	-
Flow species	Air (77% N ₂ , 23% O ₂)	-
Injection start	5	ms
Injection duration	20	ms
Injected mass	97	mg

Parameter	Value	Unit
Injected liquid temperature	298	K
Droplet breakup model	Primary – LISA; Secondary – TAB	-
Injection pressure	6	bar g
Injector and spray geometry	As per the OEM part used for experiment	-

Five values of air flow rate and three temperatures are reported in this study. Table 3.2 outlines the conditions of the simulation runs while all the other parameters remained constant. The program was run on a desktop PC with 3.5 GHz Intel i7 CPU and 12 GB of memory. Each run took approximately 5 hours of computation time.

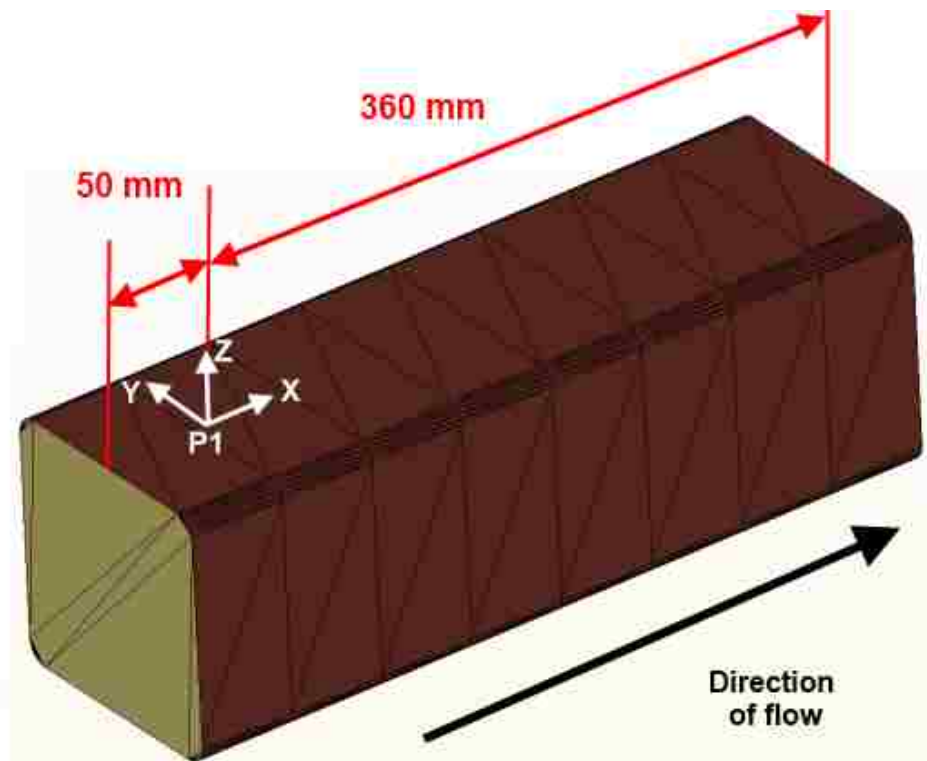


Figure 3.1. CONVERGE geometry input and coordinate system

Table 3.2. Summary of simulation runs

Simulation no.	Mass flow rate [g/s]	Gas temperature [K]
1	0	423
2	15	423
3	20	423
4	25	423
5	30	423
6	15	473
7	15	523

3.3. Simulation Results

All the results presented herein are at $Y=0$. Hence, the viewing plane is a centrally located ZX plane based on the coordinate system (Figure 3.1). This was chosen for direct comparison with the PDA results in Chapter 5. The only differences between the simulation and the empirical coordinate systems are the direction of the Z-axis and the location of the origin. The central viewing plane allows the hollow conical shape of the spray to be seen as two ligaments of liquid. The figure captions indicate the mass flow rate of the gas, the time stamp, and the gas temperature respectively. Figure 3.2 shows the simulation time scale with the injection start and end points. The color bar on the right side of each of the figures (Figure 3.3 to Figure 3.20) divides the diameter or velocity range into 64 colors or bins. Each filled circle represents a liquid particle. Hence, the total number of liquid droplets on the viewing plane at a particular time is given by the total number of circles. The location of the circle is the location of the liquid droplet on the ZX plane. The particle's diameter or velocity is indicated by the color of the circle.

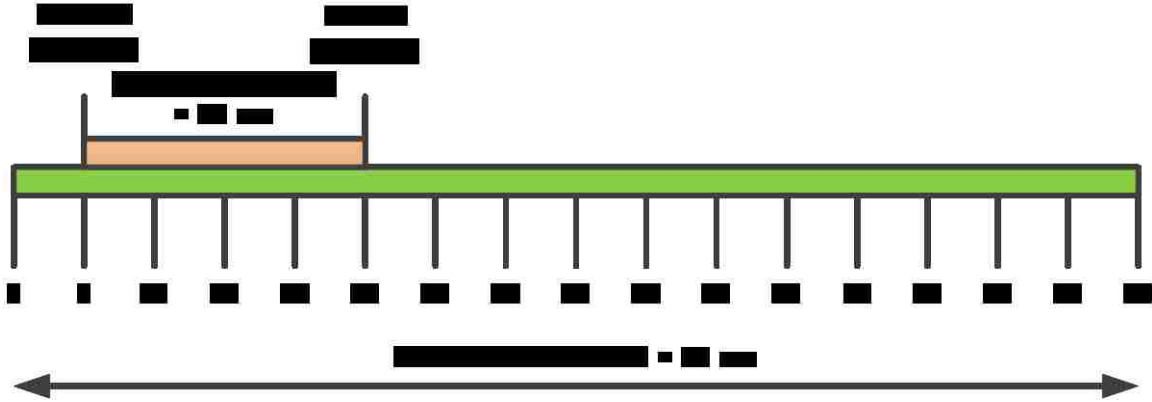


Figure 3.2. Simulation time scale

3.3.1. Effect of flow rate

The first set of simulation results (Figure 3.3 to Figure 3.7) show the calculations of particle diameter at 10 ms time stamp – 5 ms after the start of injection. The air temperature was 423 K. Without air flow (Figure 3.3, 0 g/s), the spread of the spray was quite symmetrical across the Z-axis. The largest particles ($>40 \mu\text{m}$) tended to follow the original cone profile. The smaller particles were predicted to be on the inner surface of the cone. As the air flow rate increased (Figure 3.4 to Figure 3.7), the average particle diameter remained around $22 \mu\text{m}$. However, the spray was no longer symmetrical. With increasing air flow rate, it shifted towards the positive X-direction (in the direction of the air flow) with the smallest particles being shifted to the downstream half of the cone and also forming a group of particles about 30 mm downstream of the injector axis. The empty space of the hollow cone reduced as particles moved in from negative to positive X-direction. The particles were seen to travel no more than 50 mm in the positive X-direction at this instant.

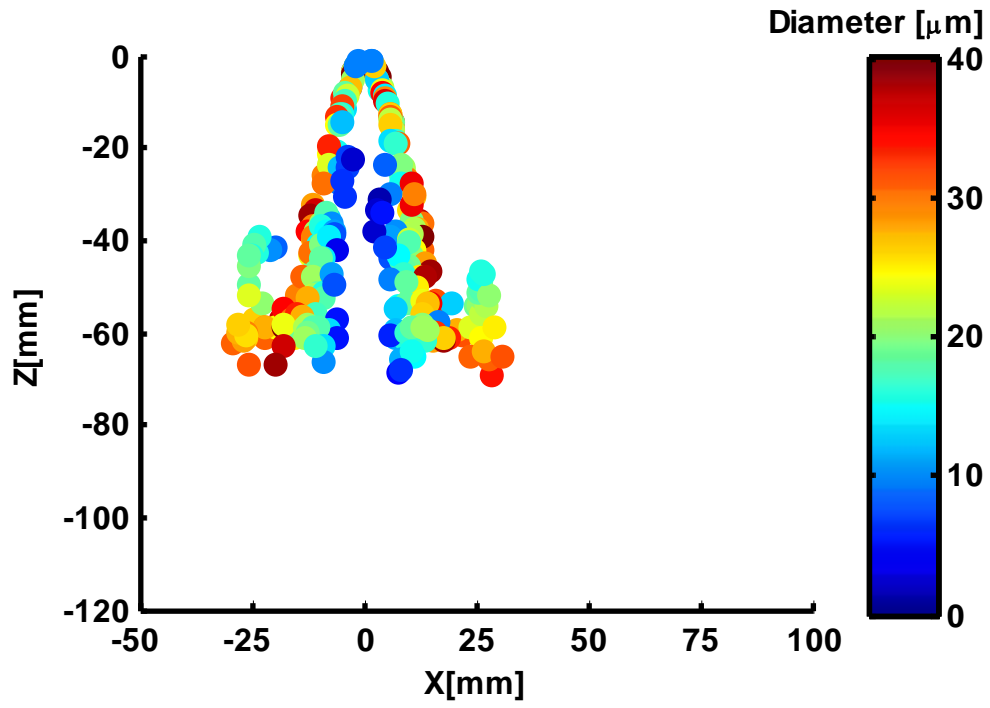


Figure 3.3. Diameter distribution – 0 g/s, 10 ms, 423 K

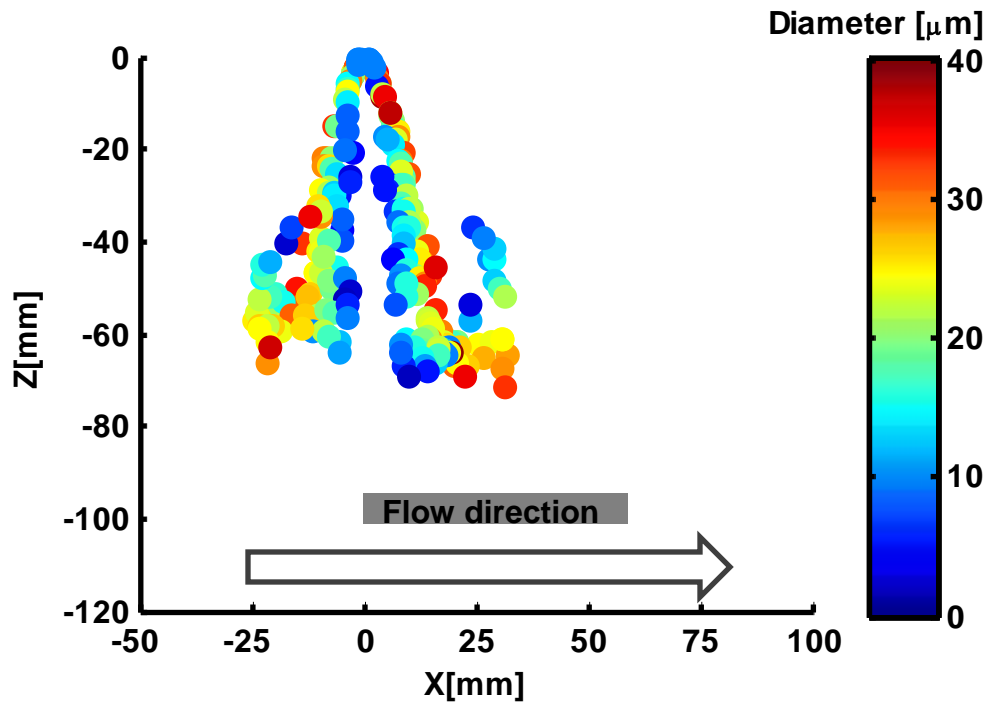


Figure 3.4. Diameter distribution – 15 g/s, 10 ms, 423 K

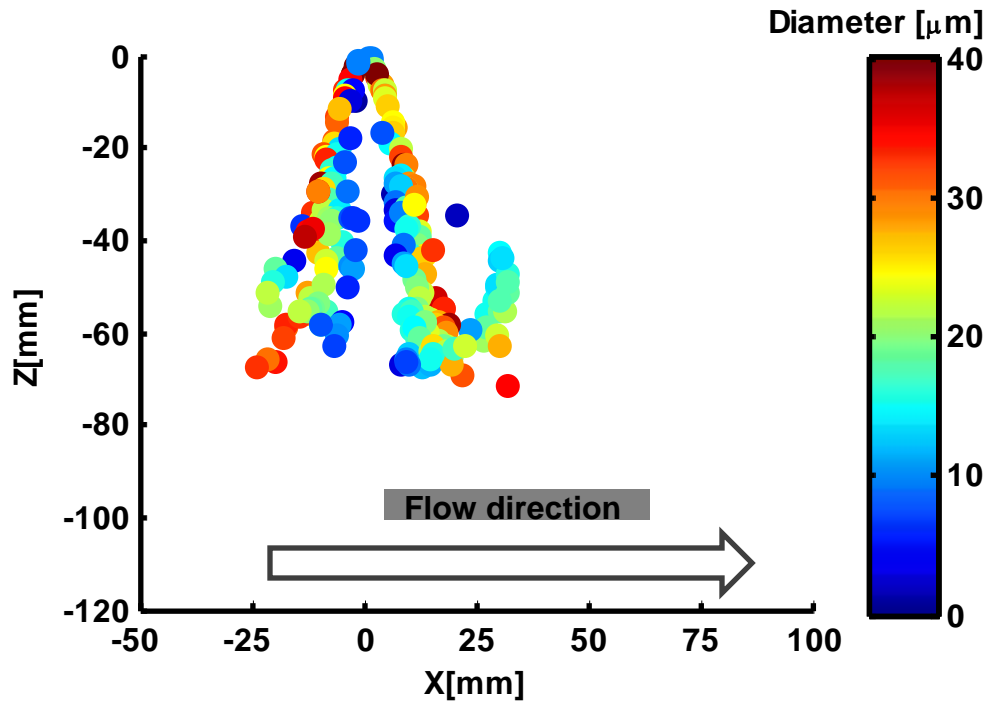


Figure 3.5. Diameter distribution – 20 g/s, 10 ms, 423 K

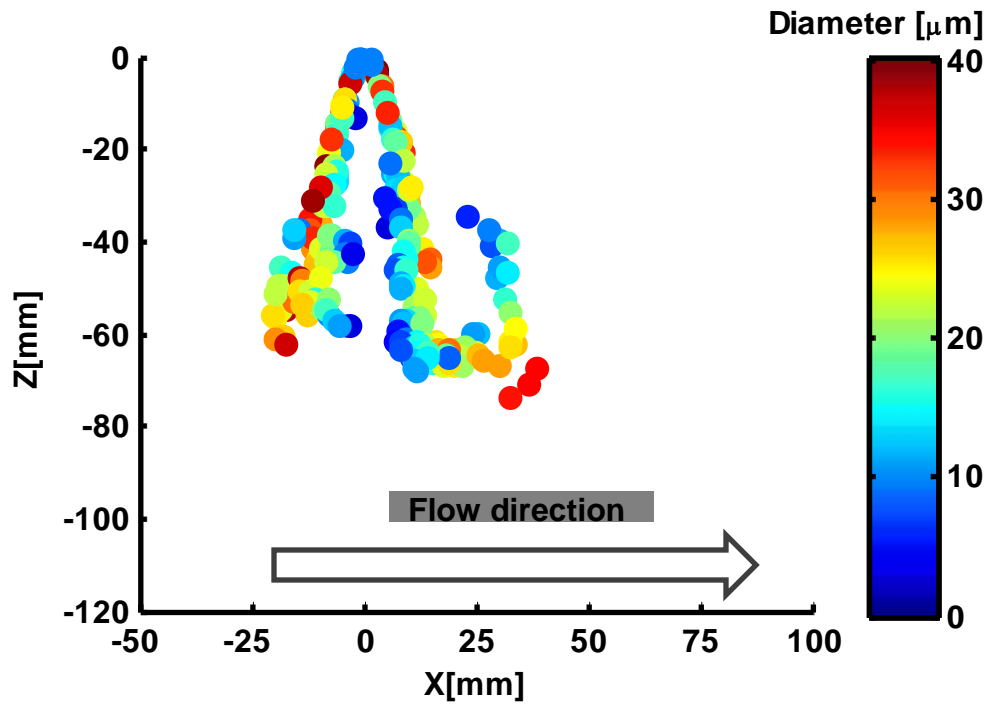


Figure 3.6. Diameter distribution – 25 g/s, 10 ms, 423 K

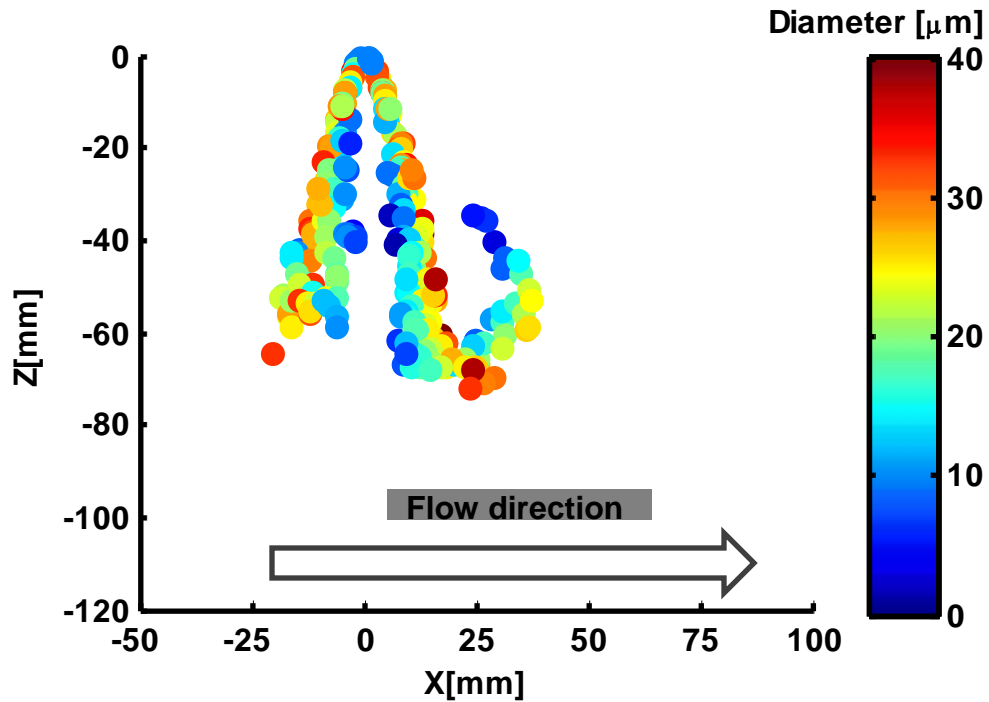


Figure 3.7. Diameter distribution – 30 g/s, 10 ms, 423 K

3.3.2. Time progression of spray

Figure 3.8 to Figure 3.11 show the progress of the spray with time, for an air mass flow rate of 15 g/s at 423 K. Half-way through the injection, at 15 ms, the first of the particles began to reach the bottom of the chamber. The shift of the spray towards the direction of the air flow is evident. There was a conglomeration of particles near the bottom made up of particles broken off from the cone, particles which broke off earlier being swept by the flow, and particles hitting the bottom of the chamber and bouncing back. Later, at 20 ms, the field greater than 25 mm downstream started to clear due to evaporation and transport of droplets downstream from the injector axis. At this time, some mid-range particles had traveled up to 75 mm in the positive X-direction. Further at 25 ms, the injection was about to end. At 30 ms, the remnants of the spray were seen in the lower half of the chamber with most particles having a diameter below 20 μm . All the particles had evaporated before the 100 mm mark from the injector axis at little over 50 ms.

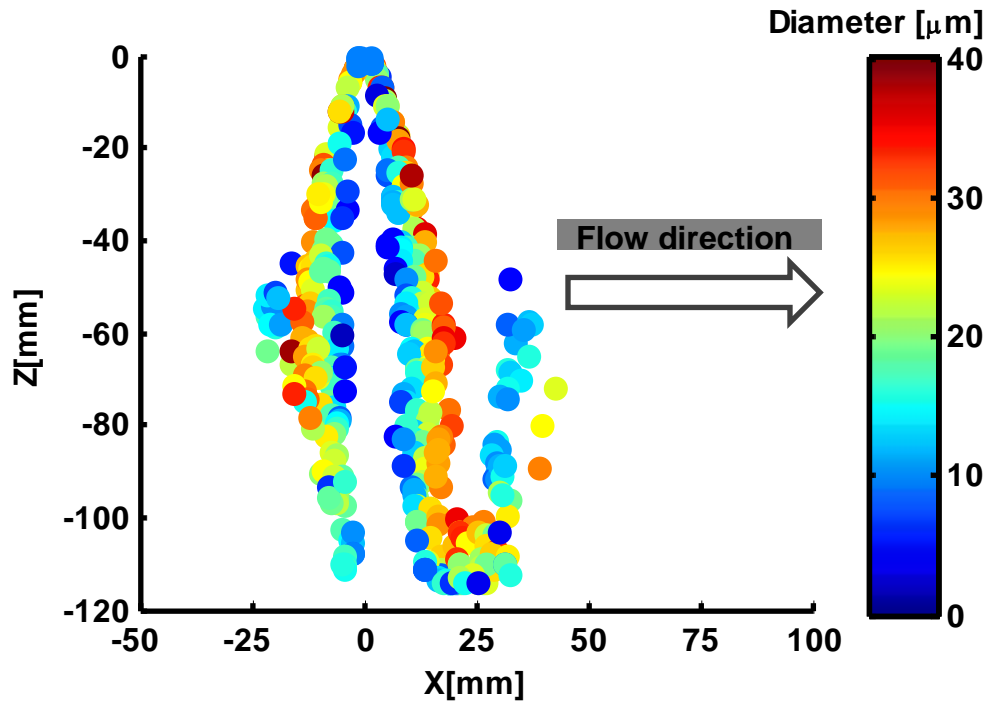


Figure 3.8. Diameter distribution – 15 g/s, 15 ms, 423 K

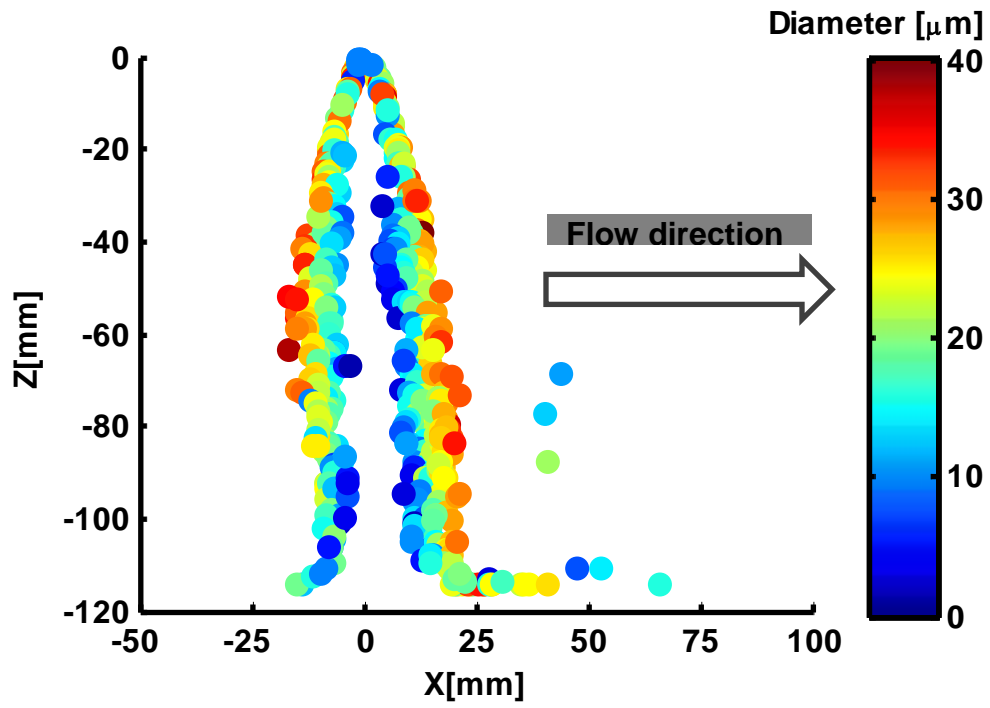


Figure 3.9. Diameter distribution – 15 g/s, 20 ms, 423 K

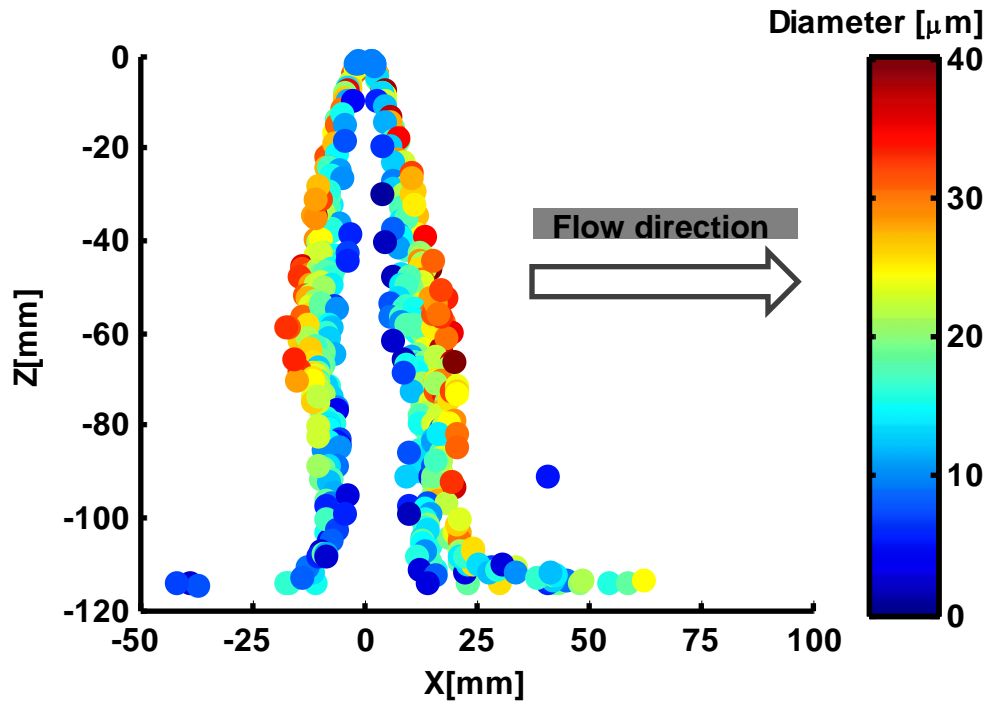


Figure 3.10. Diameter distribution – 15 g/s, 25 ms, 423 K

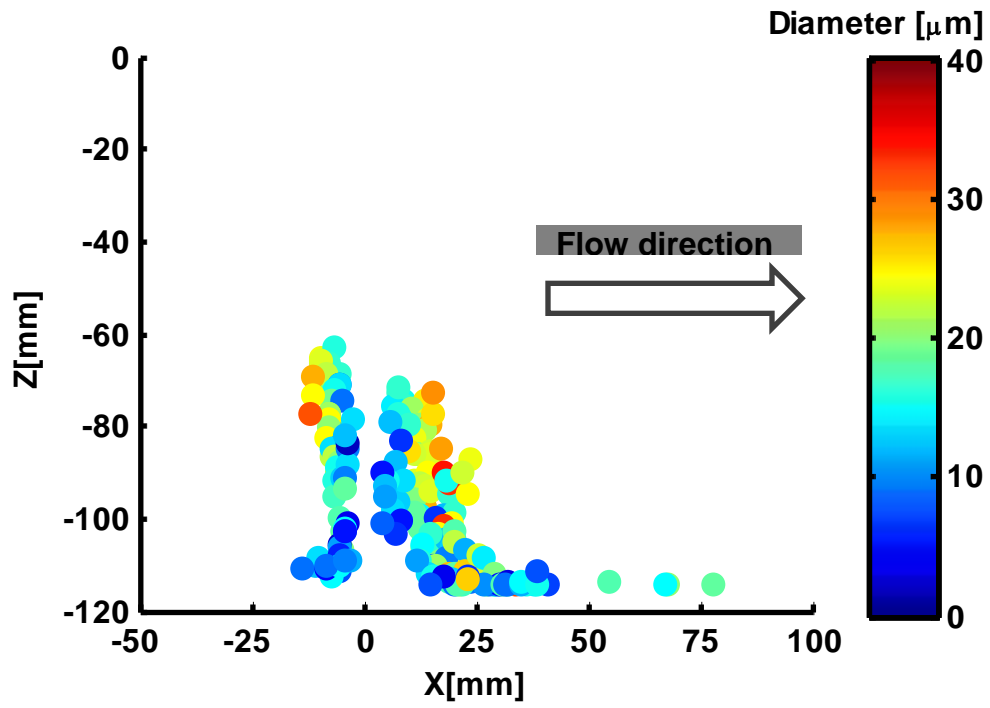


Figure 3.11. Diameter distribution – 15 g/s, 30 ms, 423 K

3.3.3. Effect of increasing temperature

The air flow temperature was increased from 423 (Figure 3.11) to 473 K (Figure 3.12), and finally to 523 K (Figure 3.13). There was a shift of the diameter distribution towards smaller sizes as well as a reduction in the particle count as temperature increased. All plots are at 30 ms time. It was also seen that at 523 K, very few particles remained beyond 50 mm in the positive X-direction. The liquid mass remaining in the chamber with respect to time was calculated as shown in Figure 3.14 which indicated the increase in the overall evaporation with increasing air flow temperature.

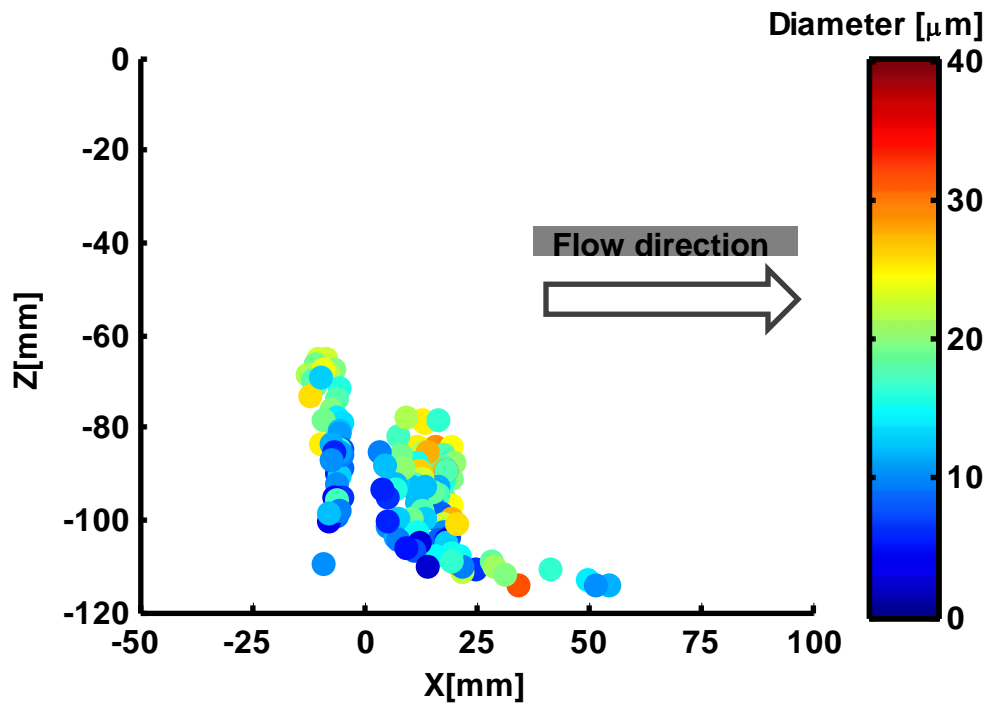


Figure 3.12. Diameter distribution – 15 g/s, 30 ms, 473 K

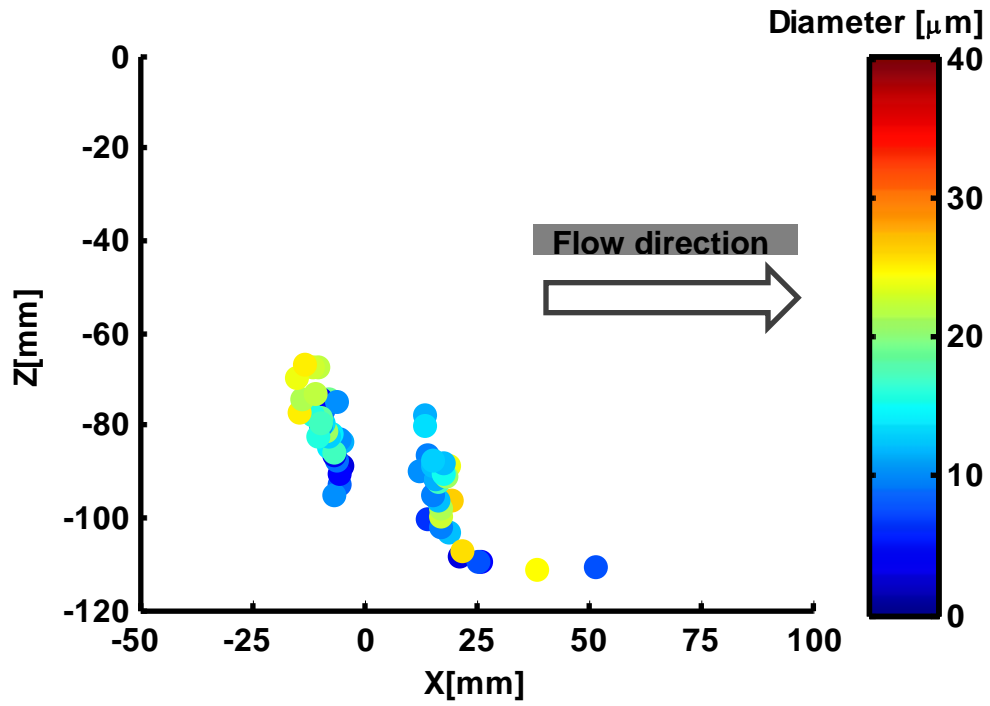


Figure 3.13. Diameter distribution – 15 g/s, 30 ms, 523 K

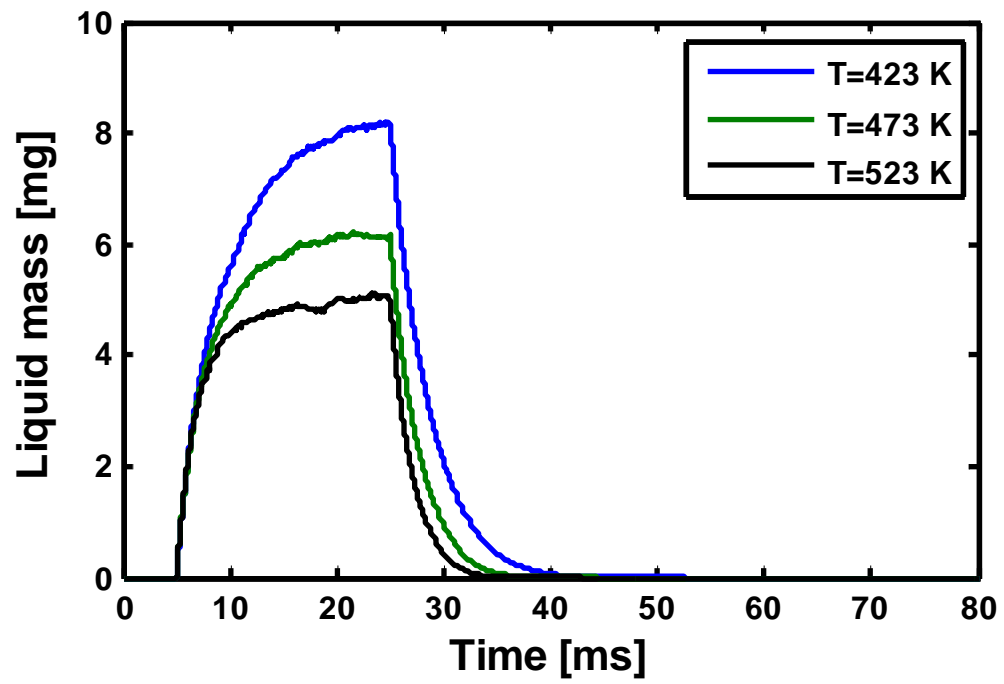


Figure 3.14. Liquid mass in the chamber vs. simulation time

3.3.4. Velocity of droplets

The air velocity in the XZ- plane is shown in Figure 3.15 for 15 g/s at 20 ms and 423 K. The color represents the magnitude of the velocity on this plane – resultant of horizontal (X) and vertical (Z) velocity. The direction and length of the arrow indicate the direction of velocity and the relative magnitude of velocity respectively. The effect of the injection can be seen in the image. The highest velocity (~30 m/s) was inside the center of the hollow cone in the vertically downward direction and decreased horizontally outward from the injector axis. Outside the liquid cone, the air velocity was lowest – equal to the bulk air flow velocity of 1.4 m/s and primarily oriented in the positive horizontal direction.

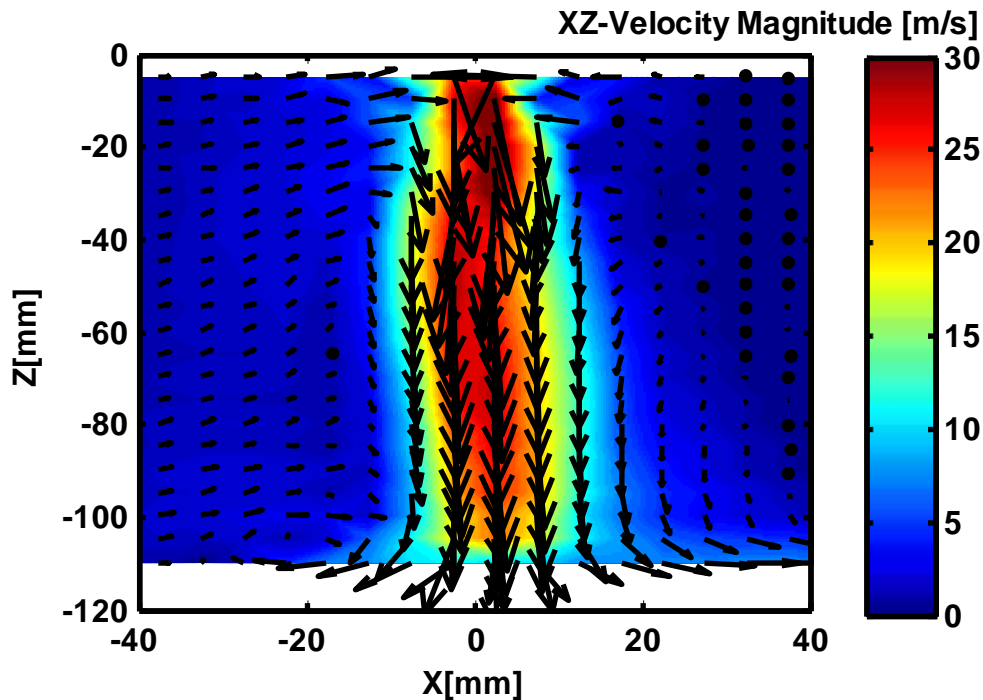


Figure 3.15. XZ-Velocity of air in the chamber – 15 g/s, 20 ms, 423 K

Plots for the magnitude of droplet velocity in the X-direction are shown for air flow rates of 0, 15 and 30 g/s at 15 ms and a temperature of 423 K in Figure 3.16 to Figure 3.18. These correspond to air flow velocities of 0, 1.4 and 2.8 m/s respectively. The maximum velocity of particles was near the injector tip with X or Y components of velocities as high as 38 m/s. But 30 mm below the injector tip, the droplets had slowed down

considerably with most of the particles having speeds between 2-5 m/s. As the air flow velocity increased, the magnitude of droplet velocity remained in the same range. Some high speed particles (10-20 m/s) were observed near the bottom of the chamber.

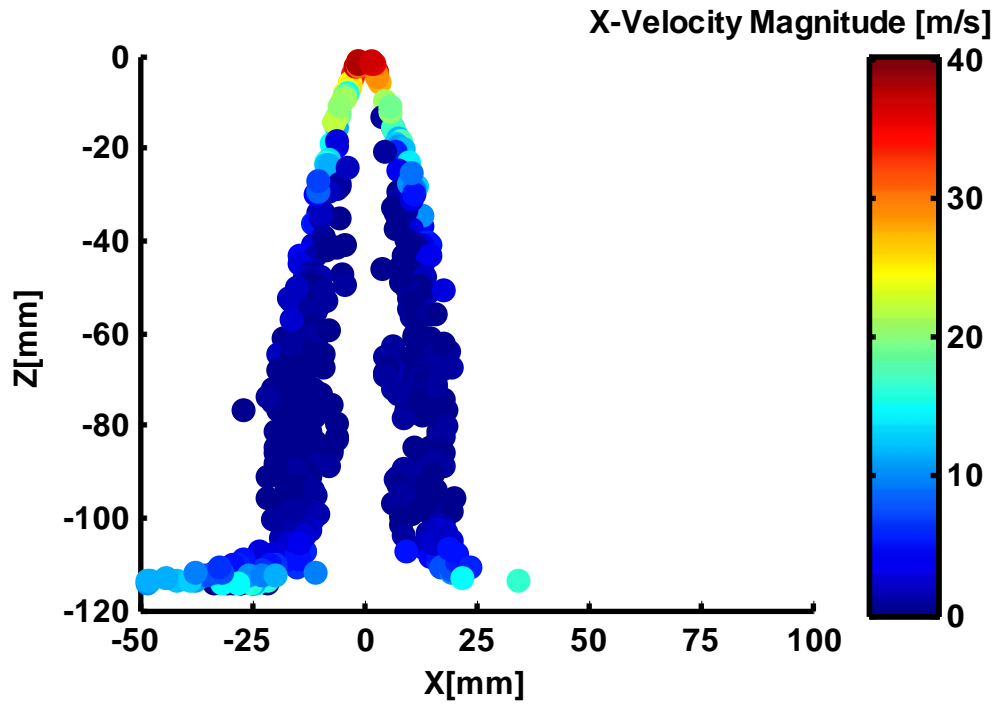


Figure 3.16. X-Velocity magnitude distribution – 0 g/s, 15 ms, 423 K

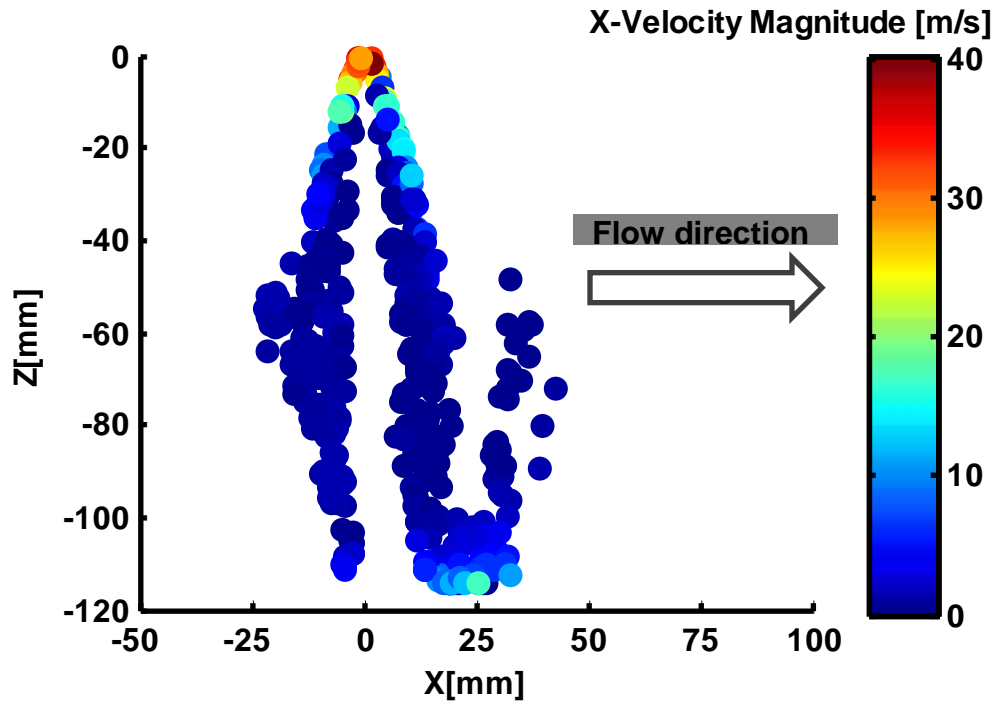


Figure 3.17. X-velocity magnitude distribution – 15 g/s, 15 ms, 423 K

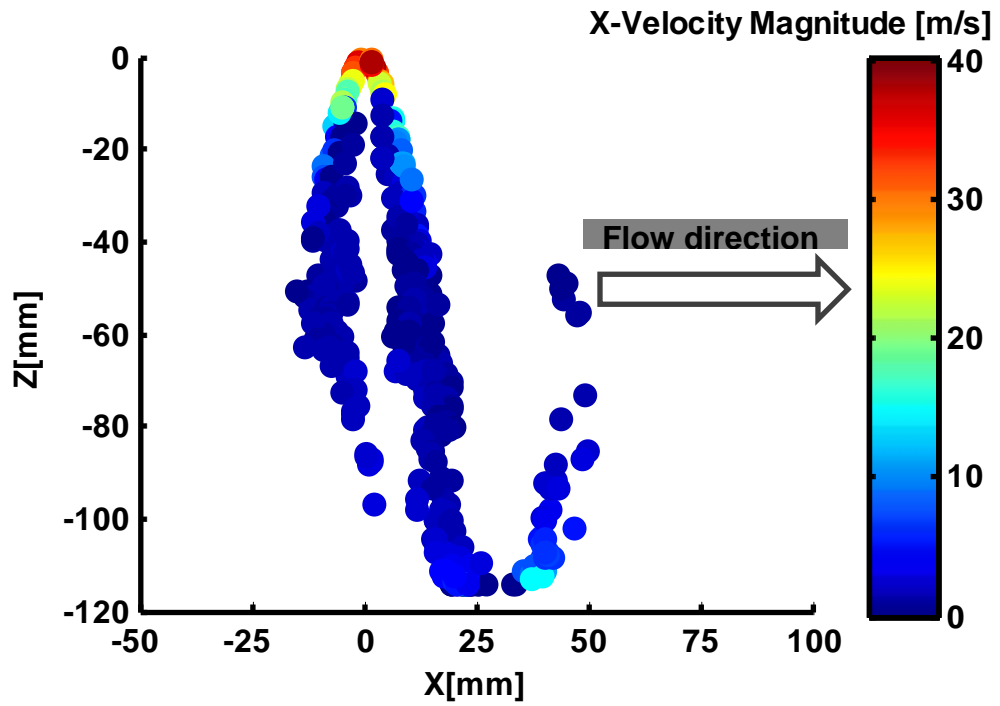


Figure 3.18. X-velocity magnitude distribution – 30 g/s, 15 ms, 423 K

Plots for the magnitude of droplet velocity in the vertical direction (Z-direction) are shown for 0 g/s and 15 g/s at 25 ms and temperature of 423 K in Figure 3.19 and Figure 3.20. The magnitude of the maximum velocity was 40 m/s. The particles with the slowest speed in the Z-direction were outside the cone and had separated from the bulk flow. The particles hit the bottom of the chamber with a mean vertical speed of 9 m/s. Without flow, the particles had fairly symmetrical distribution of speed around the Z-axis ($X=0$). In Figure 3.20, the low vertical speed particles accumulating in the chamber bottom can be seen as well.

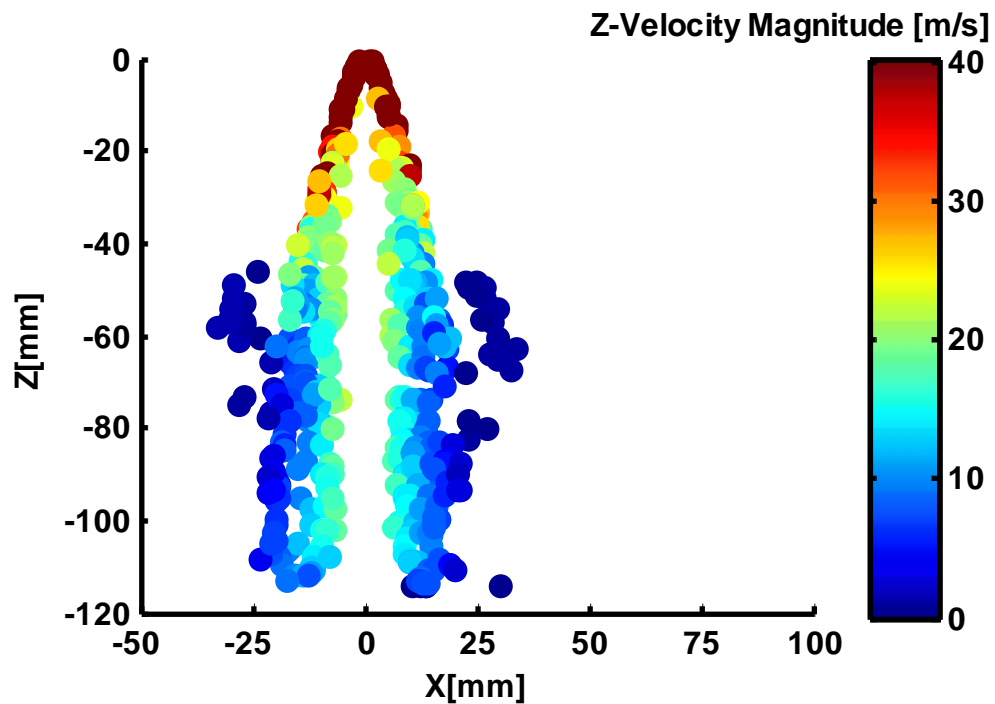


Figure 3.19. Z-velocity distribution – 0 g/s, 15 ms, 423 K

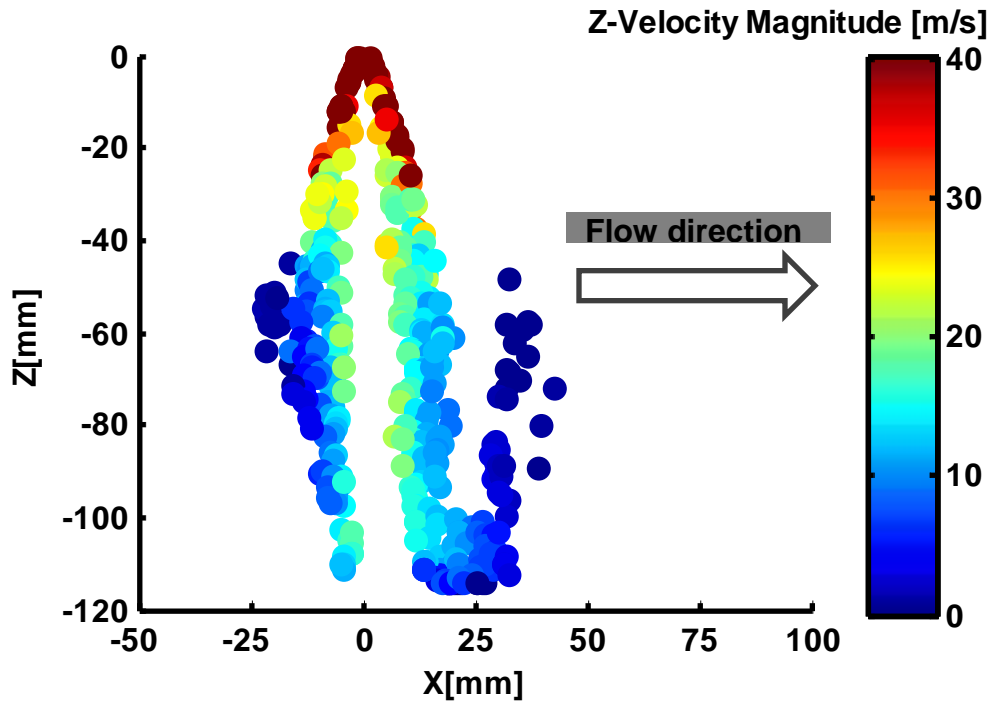


Figure 3.20. Z-velocity distribution – 15 g/s, 15 ms, 423 K

3.3.5. Sauter mean diameter vs. time

The Sauter mean diameter (SMD) is related to the speed of evaporation of the spray. It is the ratio of the total liquid volume to the available surface area of the liquid. The plot of SMD with respect to simulation time is shown for the different air flow rates at 423 K in Figure 3.21. As the air flow rate increased, the SMD reduction became steeper. This indicated two phenomena. The first was the reduction in the liquid volume inside the chamber due to evaporation. The second was the breakup of large droplets into smaller droplets. When the SMD became 0, there was no liquid mass left in the chamber. Within 55 ms, the entire injected mass had evaporated for all the flow rates. A spike was seen near the 50 ms mark for the 30 g/s flow. It was a single particle which remained in the chamber for an extended period of time and finally evaporated. Multiple simulation runs at 30 g/s produced the same result and could be attributed to an anomaly in the code. The predicted trend is shown by the dashed line. Short spikes were seen for the other flow rates as well indicating that a very small number of liquid particles remained in the chamber for an extended period of time till they evaporated.

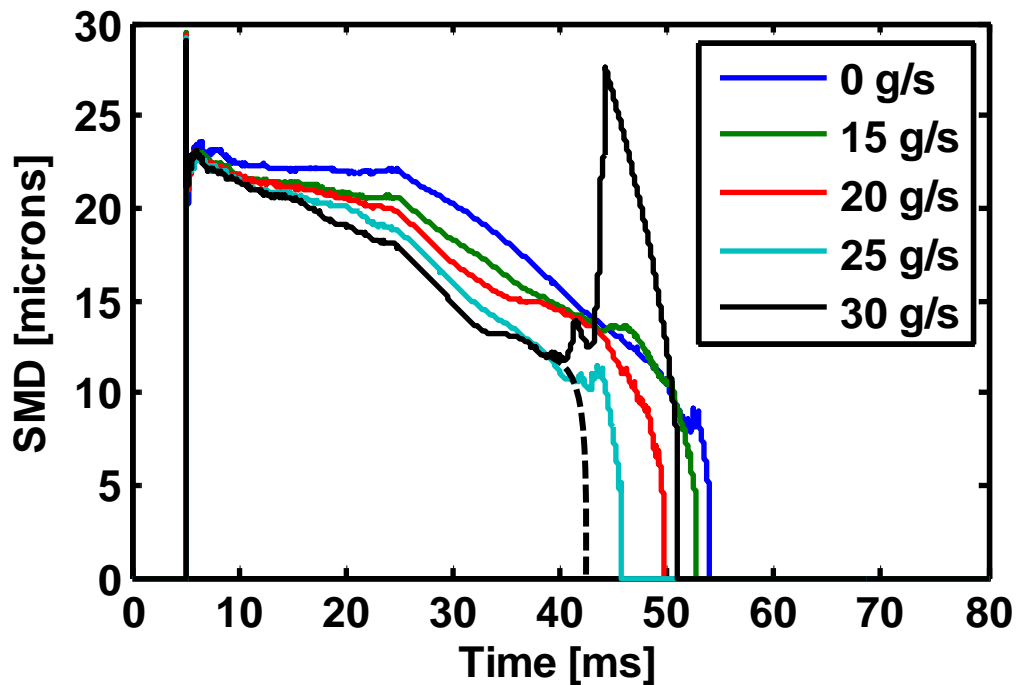


Figure 3.21. Time vs. Sauter mean diameter at different flow rates

4. EXPERIMENTAL SETUP

The experimental setup was designed with the objective to create flow conditions similar to the exhaust of a diesel engine. An after-treatment injection system had to be incorporated into the setup to spray fluid into the flow. Further, the aim was to study the injection for a considerable distance downstream. Adequate optical access was needed for PDA tests and high speed imaging. Finally, the system had to permit flow under elevated temperatures.

Diesel exhaust under low loads without EGR is quite similar in composition to air due to the high concentration of nitrogen and oxygen. Hence, the compressed air supply available in the laboratory was used as the gas medium in the flow tests. The regulated air supply was fed into a heated flow bench consisting of a Leister Hot Air Tool heater [9]. The heater was capable of providing temperatures up to 500 °C. A mass air flow (MAF) sensor was installed before the heater – Bosch model 0281002619. The reading from the MAF sensor was used to monitor the mass flow rate maintained at approximately 15 g/s. The heated feed gas was directed into a test chamber through 31.8 mm (1 ¼ inch) galvanized steel pipes. The pipes were insulated to minimize heat loss. The test chamber was mounted on a bench. The temperature of the gas was measured just prior to entry into chamber and just after the exit. For the results presented in this thesis, the average chamber temperature was set to 150 °C – the lower end of diesel exhaust temperature under idle or low load conditions. The high speed camera was positioned in front of the optical window to capture the injection event. The PDA receiving and transmitting optics were attached to a 3-axis traversing system mounted on the bench, along with the filter and fuel flow control valves for the injection system. Further details of the test chamber, fuel injection system and laser setup for PDA are described in the following subsections.

4.1. Test Chamber – Design and Construction

The test chamber was machined from a single piece of 304 ASTM A-544 stainless steel square tubing with an outer edge length of 127 mm (5 in) and wall thickness of 6.4 mm (¼ in). The length of the tube was 610 mm (24 in). Two drain ports in the bottom facilitated cleaning of the chamber. The flanges on each end were made of hot rolled steel

6.4 mm ($\frac{1}{4}$ in) thick. To maximize the linear distance over which the flow can be studied, there were two options for mounting the injectors. The first option was to fit the injector on one end and traverse the laser optics over the entire length of the chamber. The second option was to limit the travel of the optics to a smaller length and move the injector to make downstream measurements. To minimize complexity of mounting a long window, and given the constraints of the traversing unit, the second option was chosen. Four injector mounting locations were drilled on the top face of the chamber, starting at 50 mm from the inlet side and with 125 mm between each location. 254 mm (10 inch) long and 102 mm (4 inch) wide recesses were milled out on two opposite walls for optical access. 6 tapped holes (M8) were made to fasten the windows on each side (Figure 4.1).

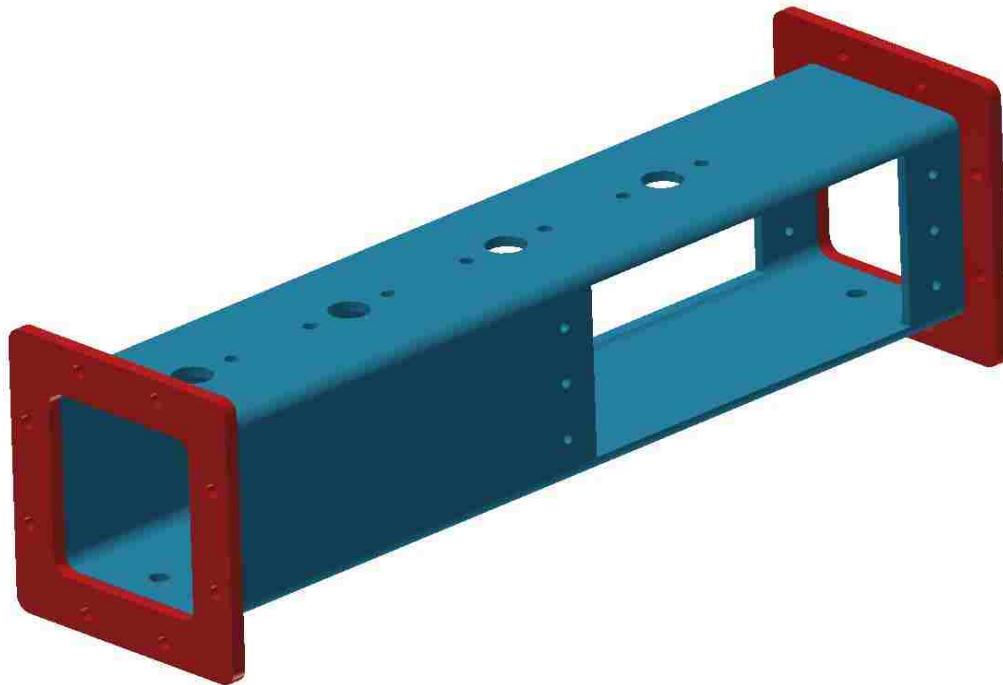


Figure 4.1. CAD drawing of the finished chamber structure

A 3-part frame was used to hold the optical windows of the chamber (Figure 4.2). All the pieces were made of 6061 aluminum 6.4 mm ($\frac{1}{4}$ in) thick and manufactured using abrasive water jet machining. The first two pieces of the frame (represented by orange and magenta colors) were aligned with the chamber main structure using the 6 mounting points. Soda lime silica glass 6.4 mm ($\frac{1}{4}$ inch) thick was glued on the orange piece using

high temperature resistant Loctite 5605 silicone adhesive. The magenta piece framed the glass. Next, the third piece (yellow) was placed on the outside with a gasket (made of heat resistant particle board) and all the three pieces were fastened to the chamber using six bolts as shown in Figure 4.2. The gasket ensured there was no metal-glass contact in the entire assembly. The contact edges between the window frame and the chamber were filled with high temperature resistant sealant to ensure that there was no air leakage. The 10 holes in the top and bottom of the frame were used to provide additional clamping force for the adhesive to set.

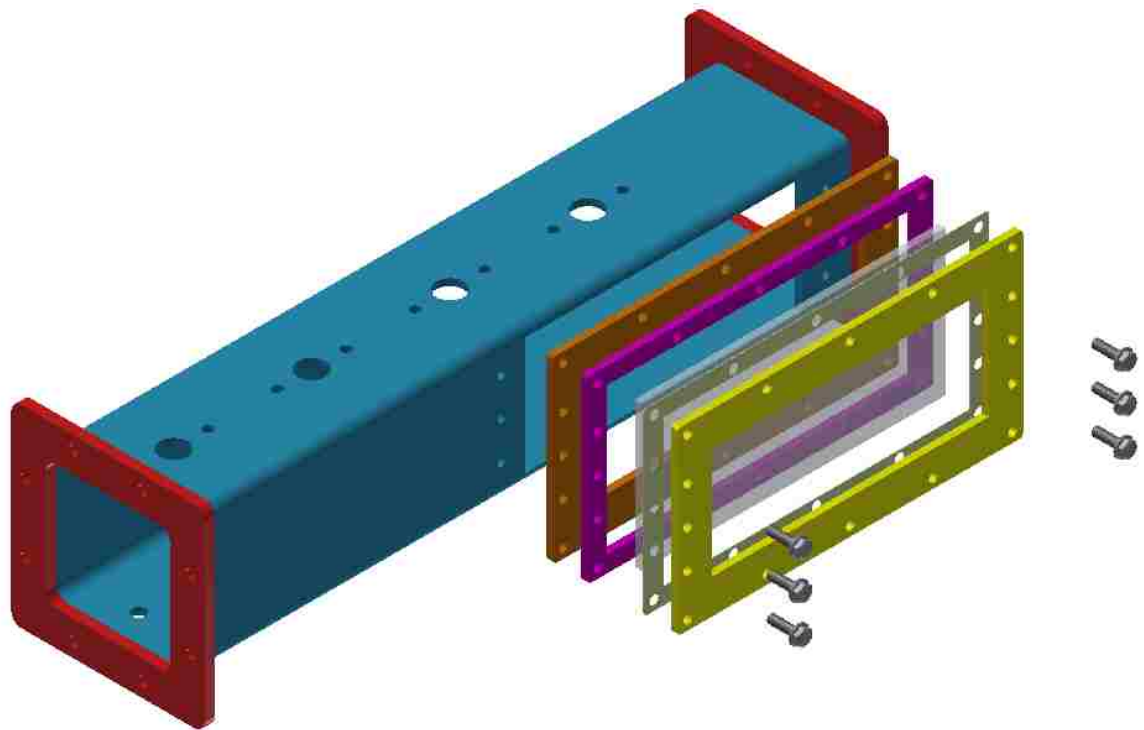


Figure 4.2. Assembly of the optical window

The feed gas was made to travel through a 610 mm (24 inch) long steel tube to partially stabilize the flow before it entered the chamber.

4.2. Injection System Setup

The injection system delivered the test fluid into the chamber. A commercially available Bosch Departronic2 after-treatment injection system [33] was used for injection. The injector (shown in Figure 4.3) was a pressure swirl type atomizer with a minimum pintle

opening pressure of 5 bar gauge. It had cooling channels for operating under high temperatures. In the first phase of PDA tests with heated flow, deionized water was used as the test liquid instead of diesel for two reasons. First, it was desired to validate the experimental system and observe the trends of the spray data safely without the risk of ignition. Second, SCR devices which use water-based urea solution injection systems (for instance, Bosch Denoxtronic 2.2 [34]) use similar injection durations and range of pressures while operating under comparable exhaust gas flow conditions. In the second phase, PDA tests were performed with diesel without gas flow at ambient temperature. The schematic diagram of the water injection system is shown in Figure 4.4. Compressed air was used to pressurize the water in a reservoir. When diesel was used as the test liquid, carbon dioxide was used for pressurization instead of air. The pressure of both test fluids was regulated to 6 bar gauge – the manufacturer recommended operating pressure.

The Departronic system had a metering unit for valve control which consisted of two solenoid valves – a shut-off valve and a dosing valve. The shut-off valve stopped the fluid flow to the injector. The dosing valve controlled the injection. National Instruments (NI) hardware and LabVIEW software were used for the valve control and data acquisition. Each valve was powered through a Pololu MD01B H-bridge driver connected to NI SCB-68 terminal box. The H-bridge circuit for the doser valve is shown in Figure 4.5. It was identical for the shut-off valve. The terminal box was connected to the NI PXI-1031 chassis consisting of a Real Time (RT) processor (model no. PXI-8106), the field-programmable gate array (FPGA) card (model No. PXI-7833R), and data acquisition (DAQ) card (model No. PXI-6070E). The FPGA provided the pulse width modulation (PWM) signals to control the valves and the trigger for syncing either the PDA measurement, or the high speed camera with the start of injection. The DAQ card acquired the mass air flow signal from the MAF sensor of the heated flow bench. The MAF voltage signal was converted into flow rate using calibration tables provided by the manufacturer.



Figure 4.3. Bosch Departronic System (Left: Shut-off and doser valve, Right: Injector)

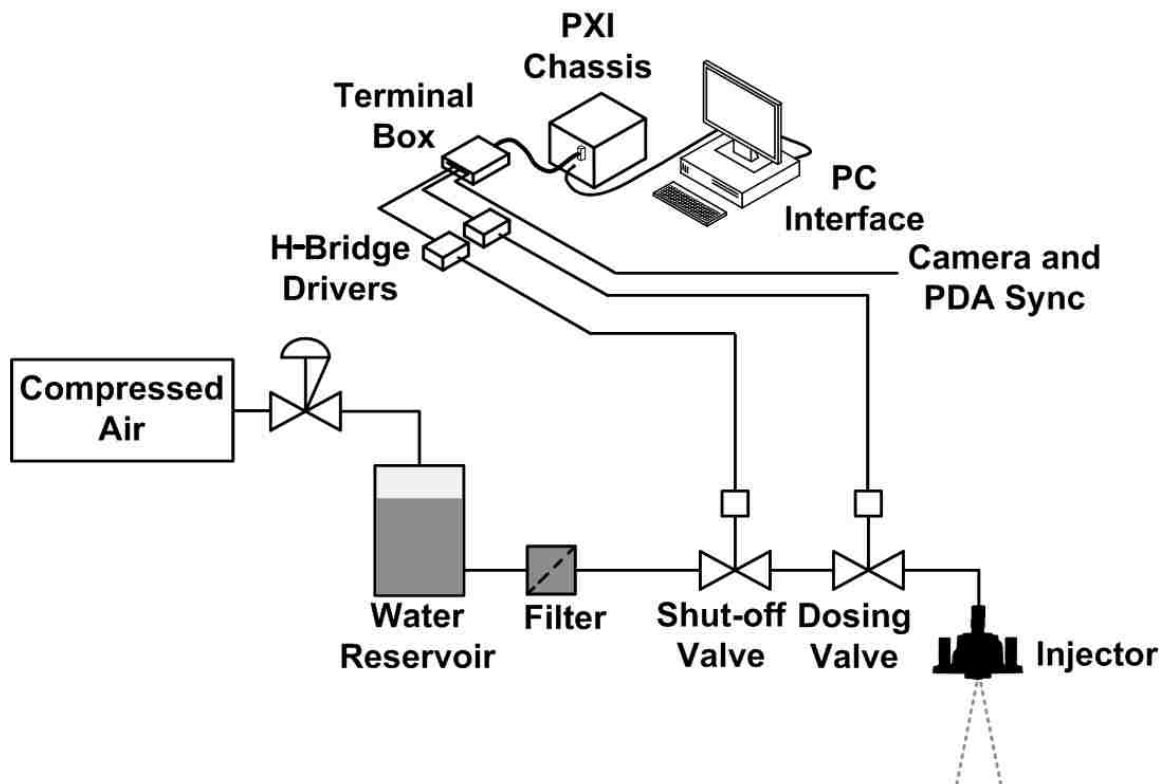


Figure 4.4. Water injection system

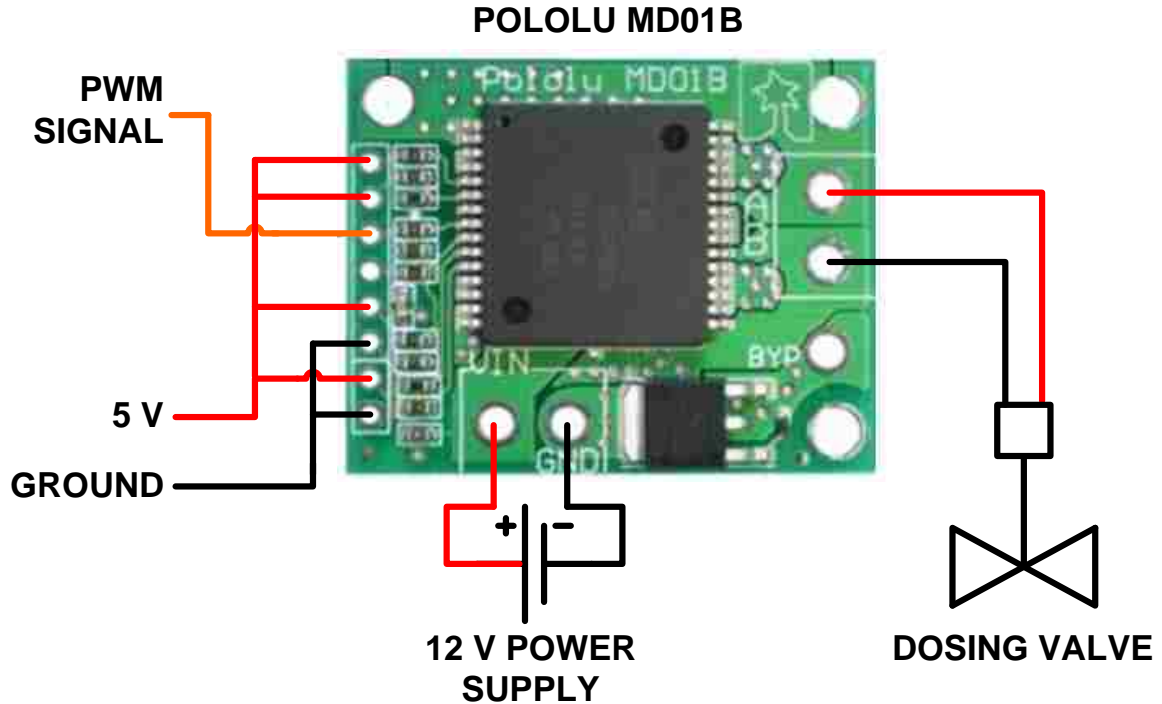


Figure 4.5. Pololu MD01B circuit diagram

The hardware was operated by a LabVIEW 2010 program co-developed by Xiaoye Han, Prasad Divekar and Dr. Shui Yu of the Clean Diesel Engine Laboratory. The LabVIEW program was run on a personal computer with the Windows 7 operating system. The front panel of the program is shown in Figure 4.6. The block diagrams for the control and data acquisition parts of the program can be seen in Appendices B and C respectively.

The injection duration ('DV T-Hold [ms]' in Figure 4.6) was set to 20 milliseconds (ms) and the injection frequency ('DV Inj Freq [Hz]' in Figure 4.6) was 2 Hz. These and the other settings were in keeping with the objective to inject reasonable quantity of liquid into the chamber for statistical analysis. The flow rate with deionized water was measured at different injection durations at 2 Hz injection frequency and 6 bar injection pressure (Figure 4.7). It was observed that the injector delivery linearly increased with the injection duration. At 20 ms / 2 Hz, the flow rate for deionized water was approximately 17 g/min.

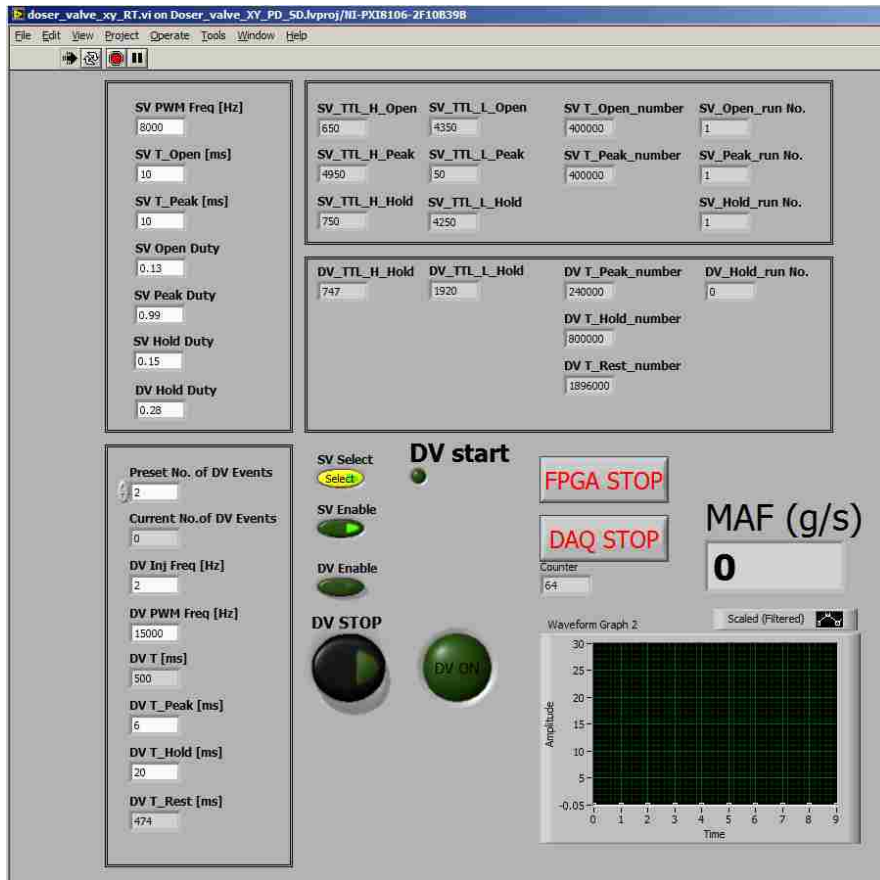


Figure 4.6. LabVIEW front panel of injection control program

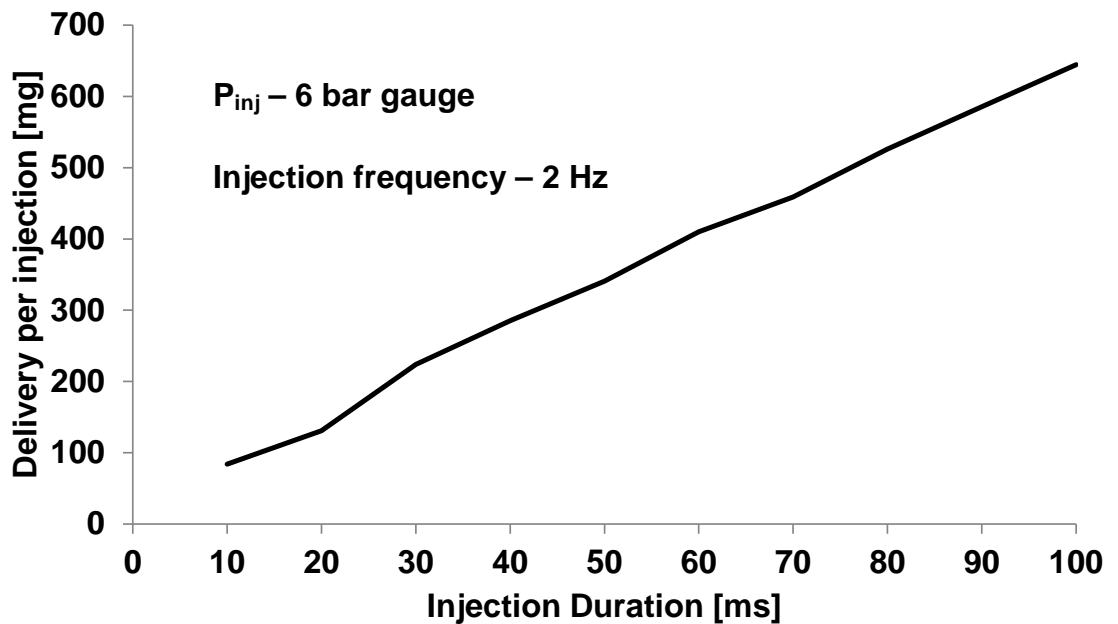


Figure 4.7. Delivery vs. injection duration

4.3. High Speed Imaging

A Vision Research Phantom v7.3 high speed camera was used to study the macroscopic properties of the spray with water as the test liquid. The images were taken under static conditions without flow, and at the standard experimental air flow rate of 15 g/s for comparison. All the images were acquired at room temperature.

The maximum speed of the camera was 6688 frames per second (fps) at full resolution of 800 X 600 pixels [35] in standard mode going up to 500,000 fps at 32 X 32 pixels. The standard image depth was 14-bit. Two resolutions were selected – 512 X 512 at 10,000 fps, and 256 X 512 at 20,000 fps. The exposure was set to 10 μ s and images were in grey scale. The camera control and image processing were performed using the Phantom Camera Control Version 8.5 software.

Two methods of illumination were used to capture the injection – front and back. Together, they enabled a complete visualization of the injection event at the desired level of detail. The illumination was continuous. The start of injection was synchronized with the camera to trigger the image capture. The setup for the two methods was identical except for the type of screen and the location of the light.

4.3.1. Front illumination

An opaque, black screen was installed on the window behind the injector (Figure 4.8). The camera was focused at the tip of the injector pintle. LED arrays were placed on front of the test chamber approximately 10 cm away from the front optical window. The light was directed such that the field of view was uniformly illuminated. The injected liquid appeared as light colored pixels on a dark background.

4.3.2. Back illumination (diffuser screen photography)

A translucent, white screen was installed on the window behind the injector (Figure 4.9). The camera was focused at the tip of the injector pintle. LED arrays were placed behind the test chamber to uniformly light the background. The spray particles appeared as darker pixels on a light background.

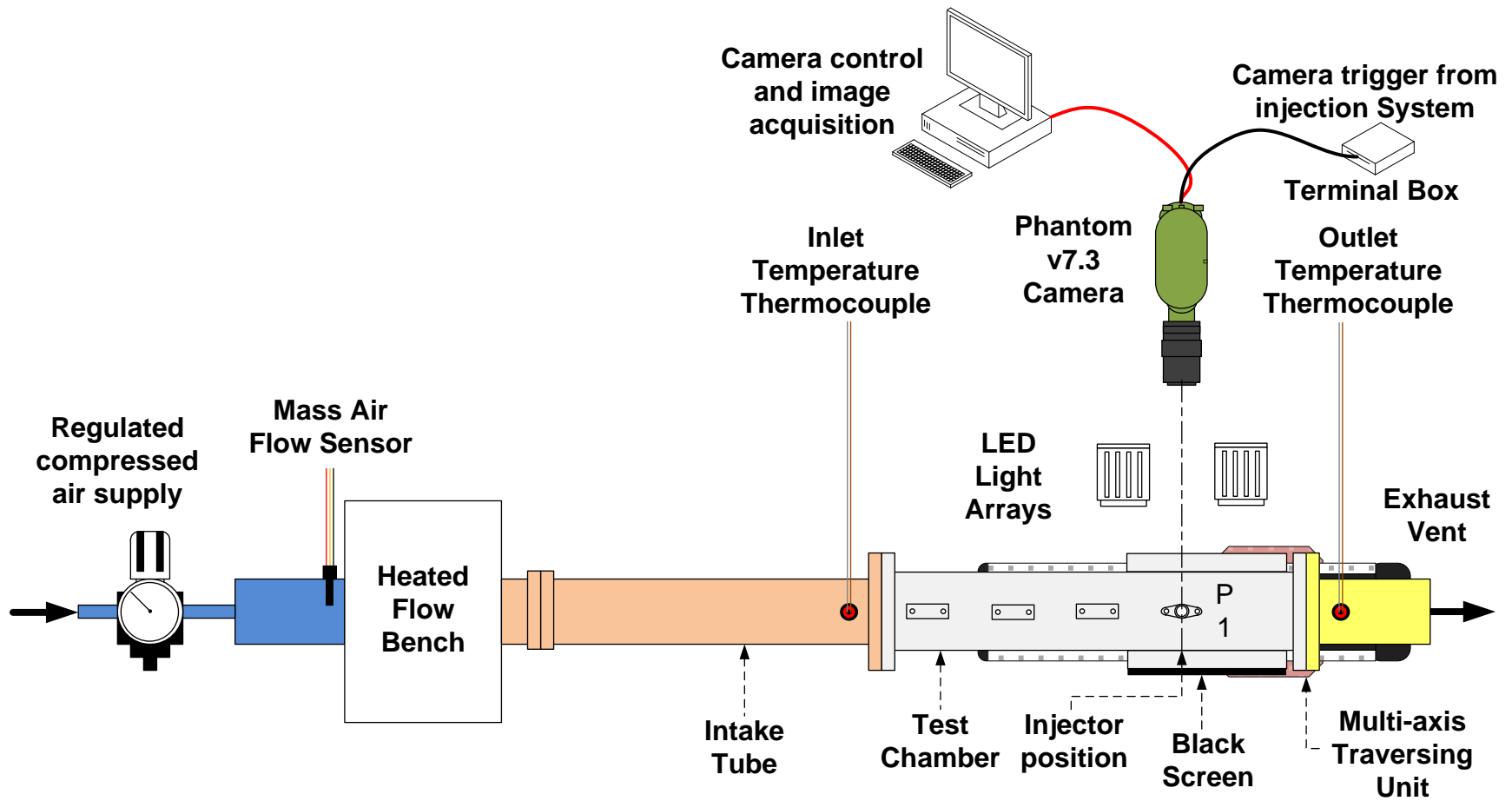


Figure 4.8. Front illuminated high speed imaging

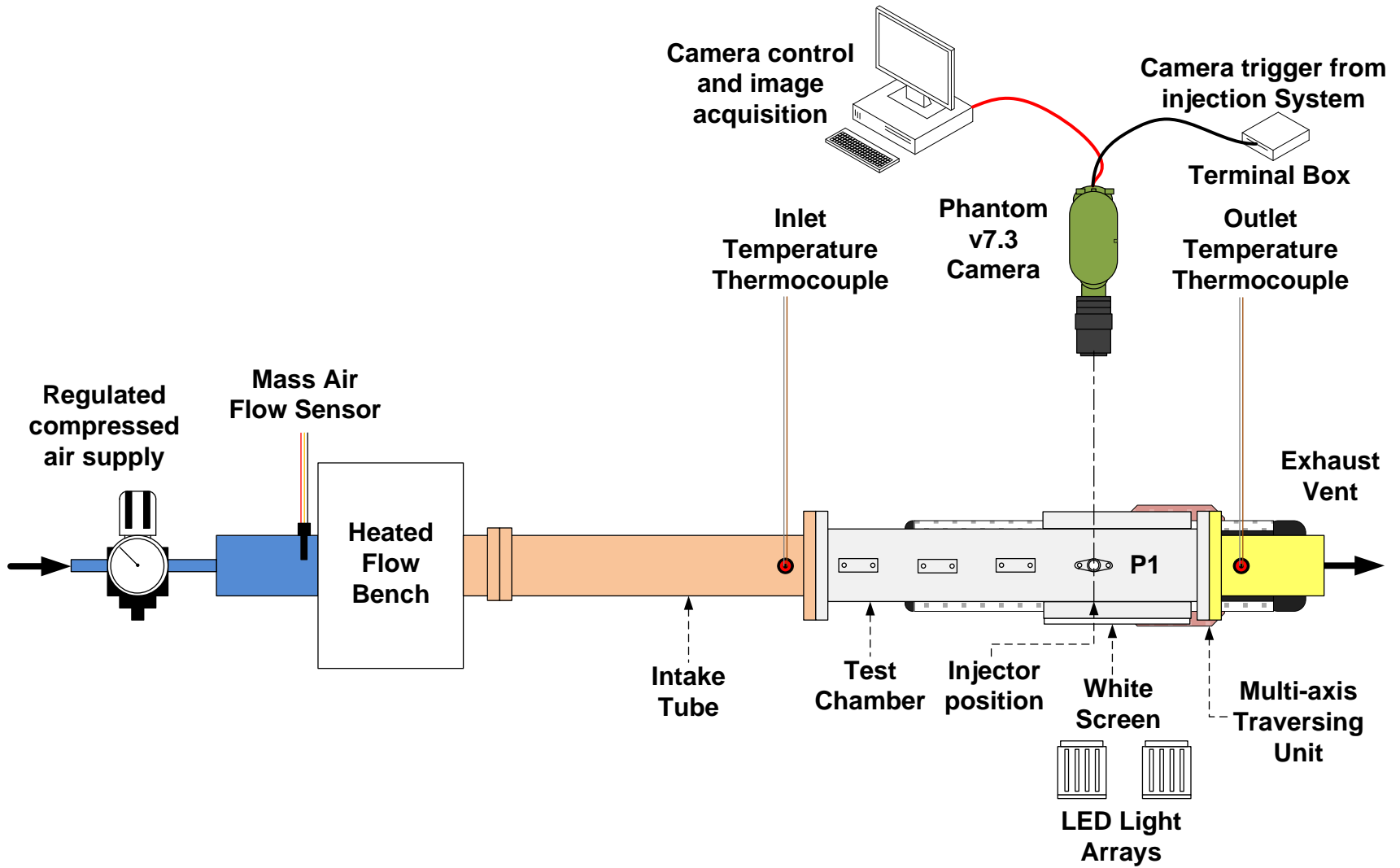


Figure 4.9. Back illuminated high speed imaging

4.4. Coordinate System for PDA Measurement

The PDA measurements were made on a single plane centrally located in the chamber. It is highlighted in pink in Figure 4.10. Hence, the Y-coordinate was zero for all data points. The constraints of the experimental setup do not allow the measurement of Y-component of velocity. P1, P2, P3 and P4 were the injector center positions, set 125 mm apart. The origin was 25 mm below the center of the first injector position, P1. The linear traverse of the optics (X-direction) only operated around the origin over a range of 100 to 130 mm. To gather data further downstream of the injection, the injector was moved upstream to positions P2 and P3. It was assumed that the flow pattern around the injector does not change when it is shifted upstream. Therefore, the total data range spread from 310 mm (60+125+125) downstream from the injector axis to 40 mm upstream of the injector axis with 10 mm between each measurement point. The vertical (Z-direction) travel started from the origin to 70 mm in the positive direction (away from injector) at 10 mm intervals – a total of 8 positions.

The data sweep was performed by first setting the Z-coordinate, then traversing along the X-axis. This was repeated for all Z-coordinates. Then, the transmitting and receiving optics were rotated by 90 degrees to capture the second velocity component, and the data sweep was performed again. Thereafter, the injector was shifted to the next position. It was found that at the last injector position, P4, the data volume was too low for any significant statistical analysis. This was due to the fact that most of the droplets either evaporated or settled on the walls of the chamber. Hence, P4 has been excluded from the results presented in this manuscript.

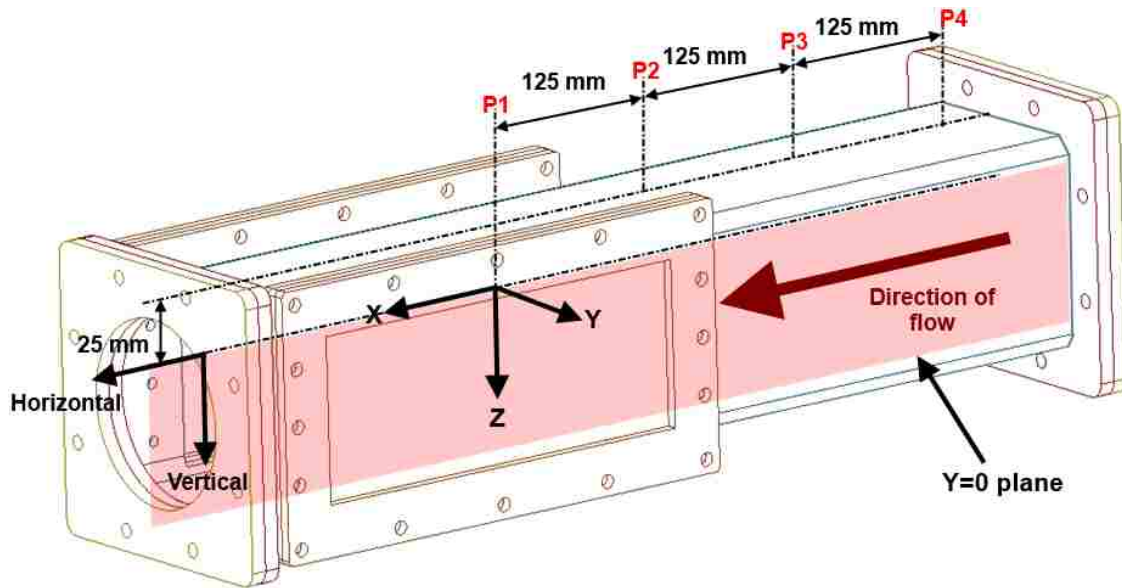


Figure 4.10. Measurement plane and coordinate system

4.5. Laser Setup for PDA and Data Acquisition

The PDA setup used for the tests is shown in Figure 4.11. It consisted of a 5 watt Spectra Physics argon gas laser head unit which provided a continuous laser beam at 514.5 nm. The laser output power was controlled by the input current. A setting of 32 amperes, corresponding to a power of approximately 0.5 W was used. A continuous flow of water maintained the head and control unit at their working temperature. The aperture setting for the head unit was 4. The laser beam from the head was incident into a beam splitter which split it into two coherent beams. The power of each of these beams was approximately 50 mW. Optical fiber bundles transferred the beams from the splitter to the Dantec Dynamics FiberFlow transmitting optics. The measurement volume produced by the beams was nominally 4.08 mm X 0.19 mm (length X width). The scattered light from the spray droplets passing through the measurement volume was captured by a Dantec Dynamics FiberPDA receiving optics. The focal lengths of the front lenses of the transmitting and receiving optics were 400 mm and 310 mm respectively. The scattering angle was set to 30 degrees so that the light scattering is dominated by refraction. The chamber and the optics were aligned accordingly to position the measurement volume on the Y=0 measurement plane (Figure 4.10).

The light signal from the receiving optics was transmitted via optical fiber bundle into the Dantec Dynamics BSA P80 Flow and Particle Processor with Fiber PDA Detector Unit. The three photo detectors converted the light signals into electrical signals. The processor analyzed the signals from the three detectors to calculate the droplet velocity and size in the flow. A synchronization signal from the injection system was used to determine the time period between the start of injection and the particle entering the measurement volume. This was necessary for time based analysis of the flow. The processing and data acquisition was controlled by Dantec Dynamics BSA Flow Software version 5.00 [36] running on a personal computer with a Windows XP operating system. The Flow Software also controlled the travel of the transmitting and receiving optics through an ISEL C142 stepper motor controller coupled with a Dantec Dynamics single axis traversing unit. The maximum range of the traversing unit was 610 mm and the maximum speed was 25 mm/s.

For each measurement position, the scanning time was 50 seconds or 10,000 particles, whichever came first. 100 injections were performed for each measurement position. The traversing system was used to advance the measurement volume in increments of 10 mm as described previously in Section 4.4.

The uncertainty in the droplet size and velocity in PDA depends on the optical configuration, spray composition, sampling and data processing [21]. It is estimated that the measurement accuracy of droplet diameter is 4% and the droplet velocity is 1% [21,36]. To check for zero reading, the PDA system was run in the absence of injection. The alignment between the transmitting optics, test chamber and receiving optics was checked at regular intervals by using a mist of water droplets. A schematic overview of the experimental setup with PDA is shown in Figure 4.12.

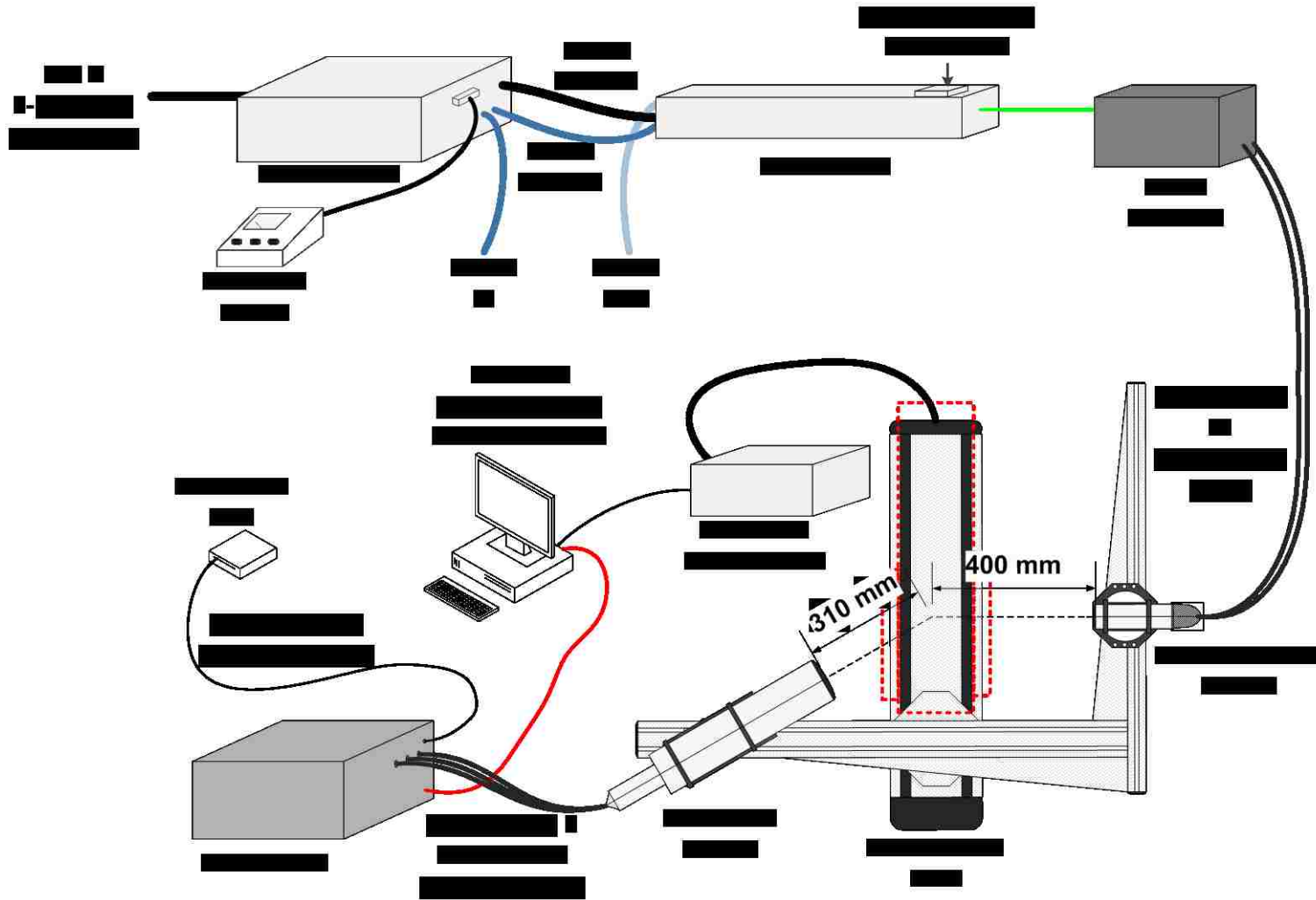


Figure 4.11. Phase Doppler anemometry setup

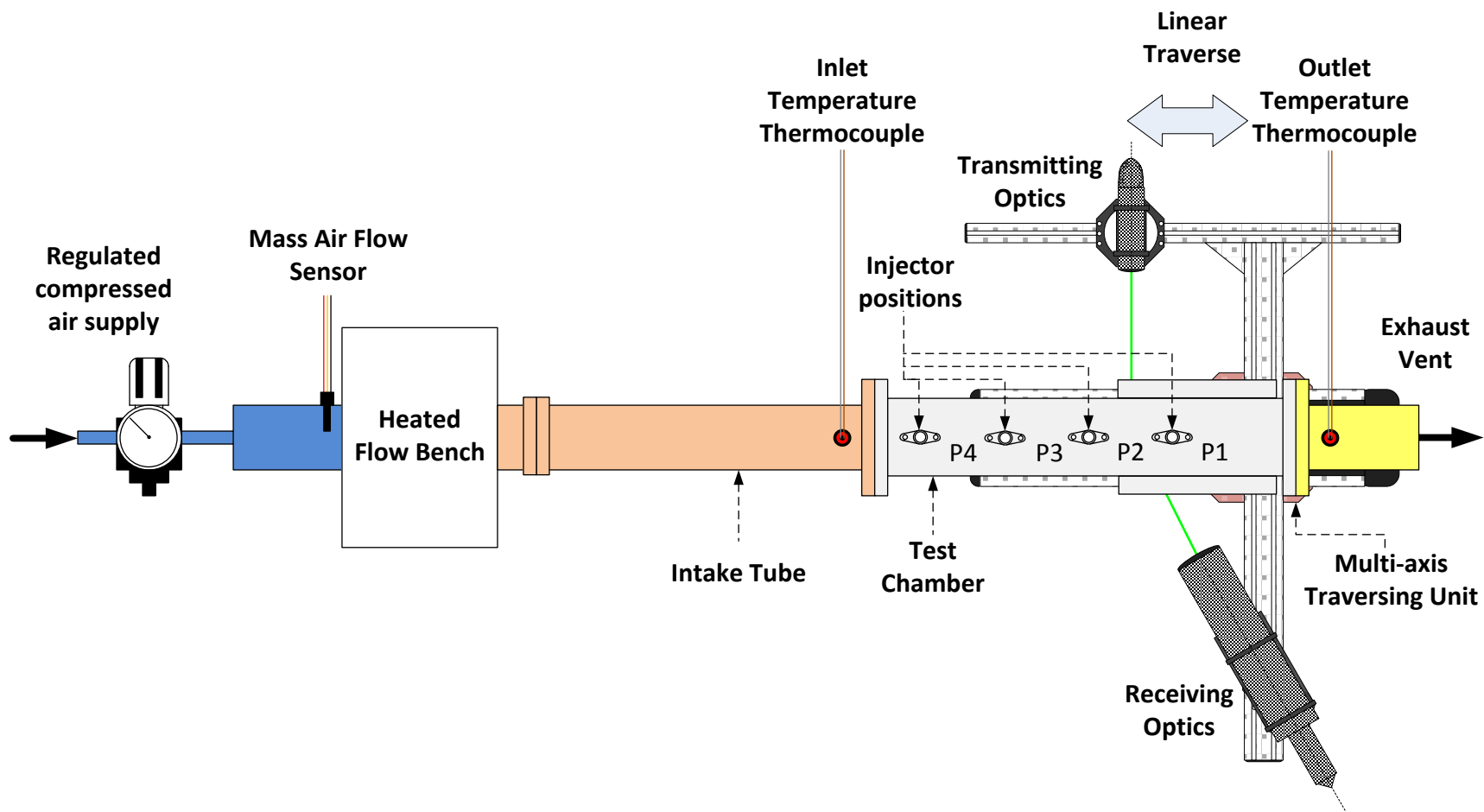


Figure 4.12. Overall experimental setup for PDA

5. RESULTS AND DISCUSSION

The results are divided into three parts. High speed imaging was initially used to view the spray with and without the flow of air. Thereafter, PDA was used to measure the spray of water subjected to air flowing at 15 g/s and heated to 150 °C. Finally, spray of diesel was measured with PDA at static condition and ambient temperature.

5.1. High Speed Imaging

High speed imaging was used to make a visual evaluation of the spray. The primary objective was to study the impact of the cross air-flow. Moreover, a macroscopic view of the spray would provide a better perspective of the PDA results.

The following sub-sections describe the recorded images of the spray with the two types of illumination described in Section 4.3. In this section, each figure consists of two images, each captured at an equal time from the injection trigger. The images on the left were taken under static conditions (without flow), while the images on the right were acquired at the standard experimental air flow rate of 15 g/s. All the images were taken at room temperature with water as the test liquid. The air flow was not heated since it was desired that the liquid particles remain in the chamber for the maximum possible time so that their motion can be observed. In these images, the air flows from right to left.

5.1.1. Front lit imaging

At 6 ms (Figure 5.1), the first of the liquid droplets were visible near the injector tip. At 12 ms (Figure 5.2), the hollow cone had started to develop. The developing cone of liquid was observed to be wider when there was flow. At 18 ms (Figure 5.3), the hollow cone had developed in both cases. A few stray liquid particles were observed to have traveled some distance downstream due to the flow. It was seen that the cone structure collapsed and broke up into droplets at about a quarter of the chamber height. Moreover, the spray had traveled approximately half the height of the chamber. At 24 ms (Figure 5.4) from the injection trigger, the spray had traversed the entire height of the chamber. The cone structure was visible near the injector tip while it had broken up into droplets over the rest of the vertical distance. Droplets were seen near the chamber bottom. Particles were observed upstream of the injector when there was flow. This could be explained by the

velocity of particles on the upstream side of the injector. Particles leaving the nozzle have horizontal as well as vertical velocity component. On the upstream (right) side of the spray, the particles had a horizontal velocity (left to right) against the direction of the air flow velocity (right to left). This meant that the flow would decelerate the particles' horizontal motion. These would eventually settle down closer to the injector axis on the upstream side. By 30 ms (Figure 5.5), the spray had ended and the last few ligaments of liquid had started to break up into particles. From 36-54 ms (Figure 5.6 to Figure 5.9), it was observed that with flow, the visible particles were fewer. The accumulated mass near the bottom of the chamber evaporated faster with flow. However, for both cases, not much visible liquid mass remained. A flow rate of 15 g/s corresponded to a flow velocity of 1.4 m/s. This, when compared to a predicted average droplet X-velocity of ~ 15 m/s would not have a severe impact on the structure and breakup of the spray.

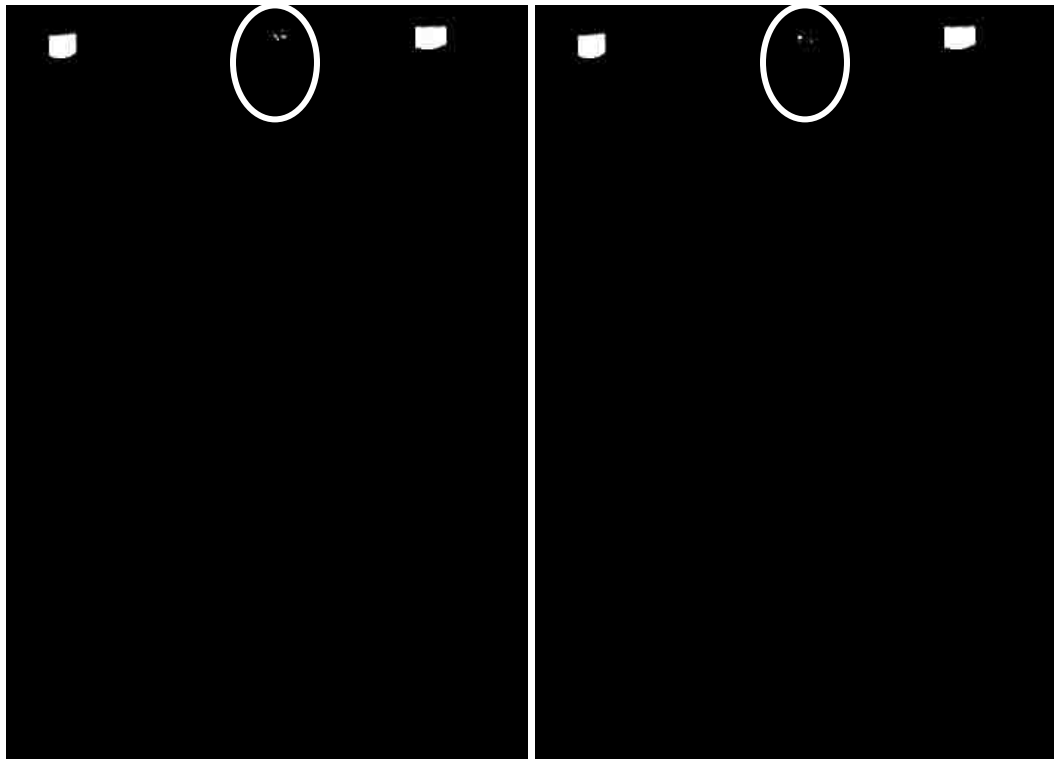


Figure 5.1. 6 ms – First appearance of liquid (Left: Without flow, Right: With flow)

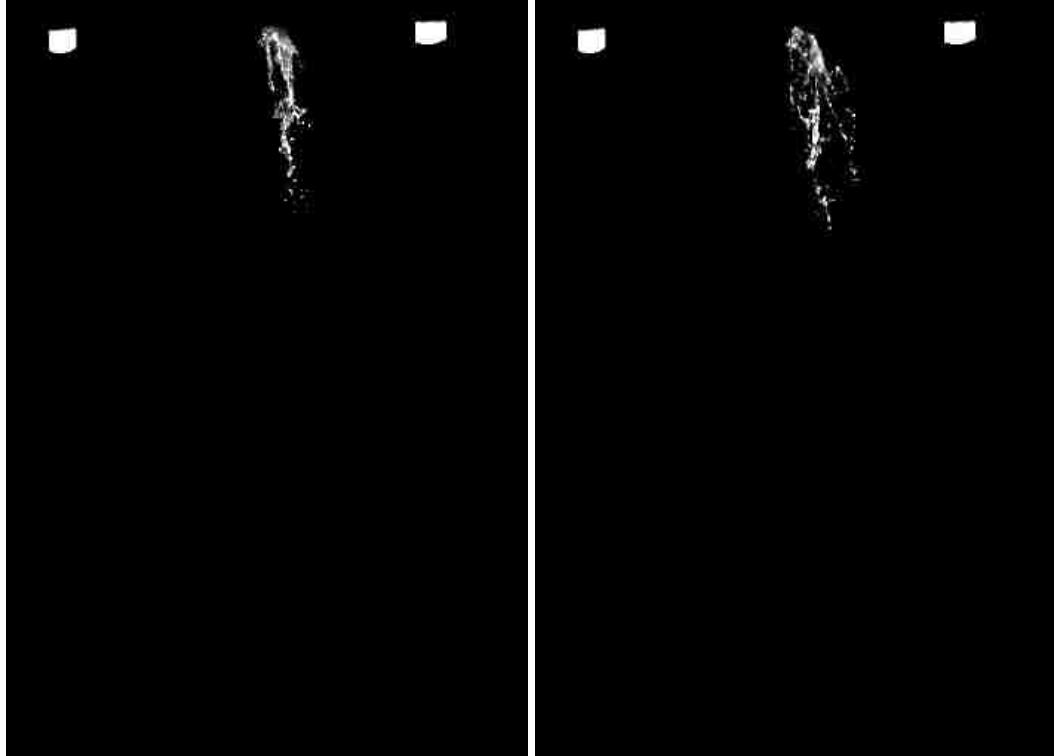


Figure 5.2. 12 ms – Development of Cone (Left: Without flow, Right: With flow)

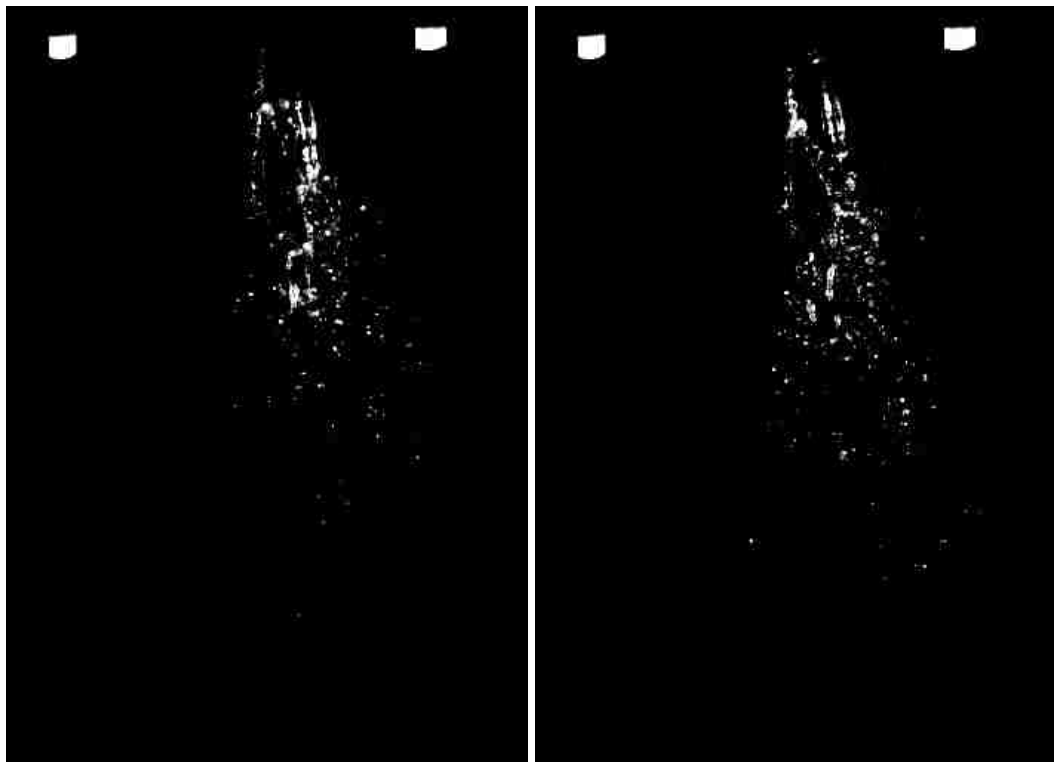


Figure 5.3. 18 ms – Developed cone (Left: Without flow, Right: With flow)

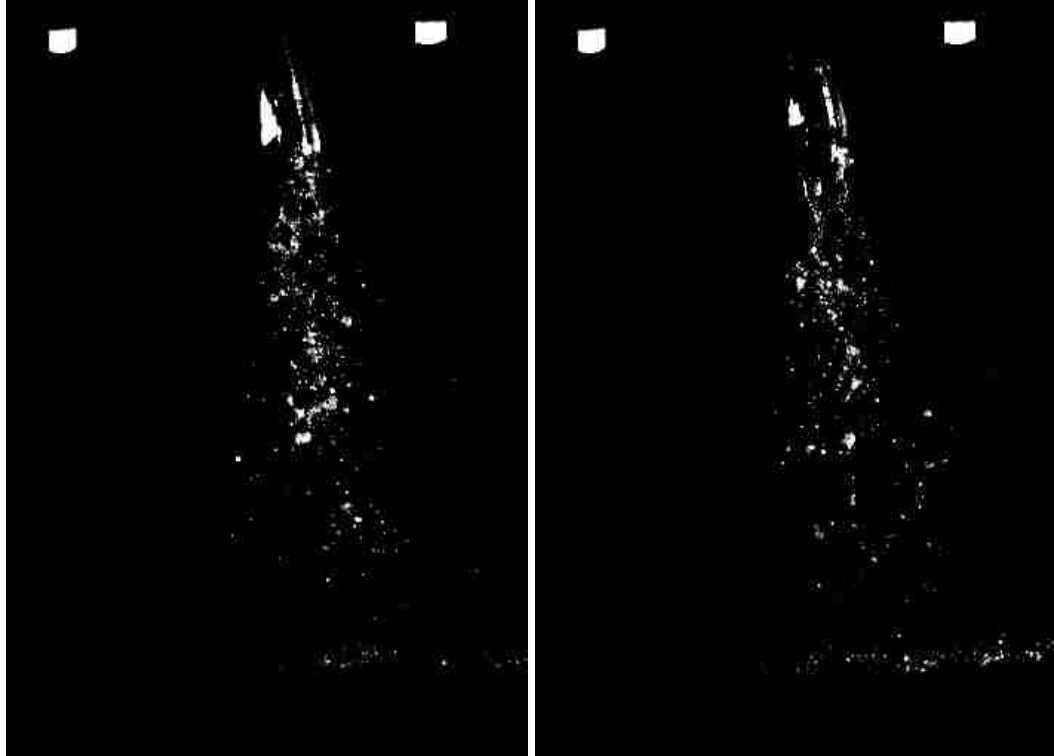


Figure 5.4. 24 ms – Cone breakup (Left: Without flow, Right: With flow)

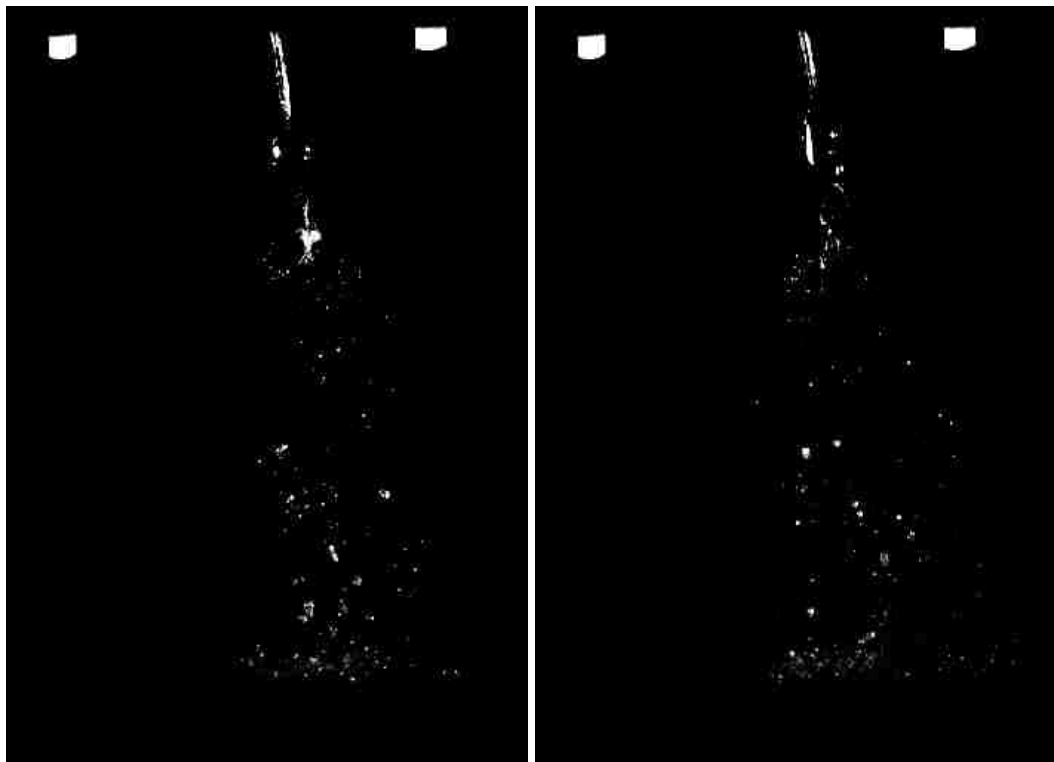


Figure 5.5. 30 ms – Breakup and end of spray (Left: Without flow, Right: With flow)



Figure 5.6. 36 ms – Evaporation (Left: Without flow, Right: With flow)

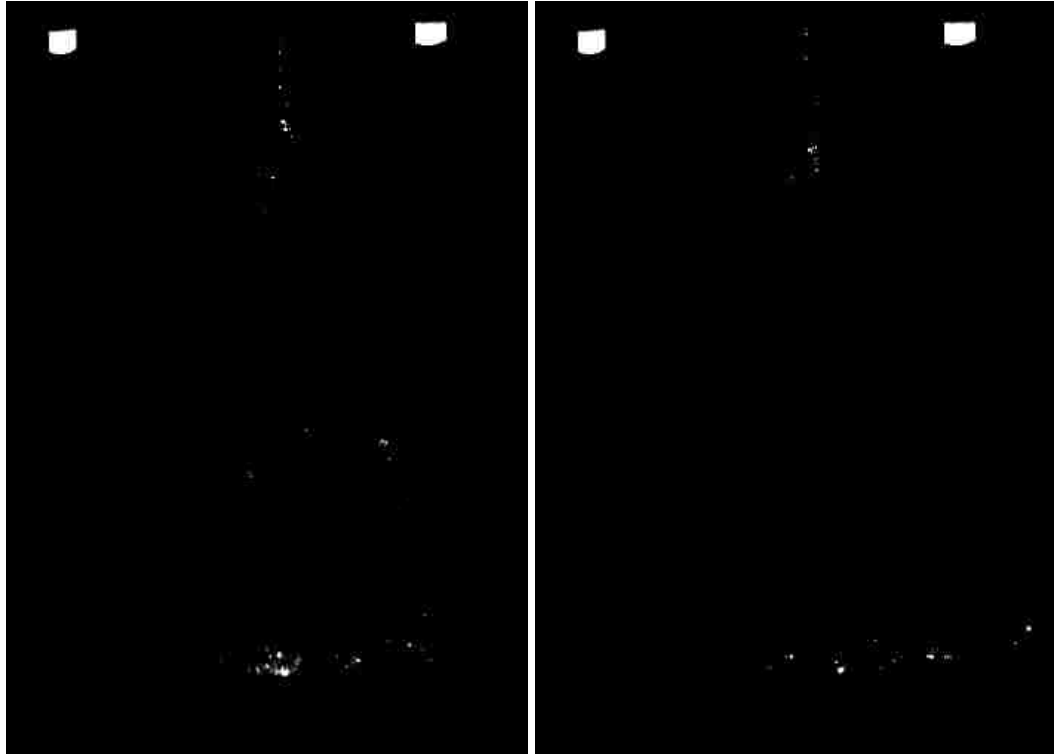


Figure 5.7. 42 ms – Evaporation (Left: Without flow, Right: With flow)

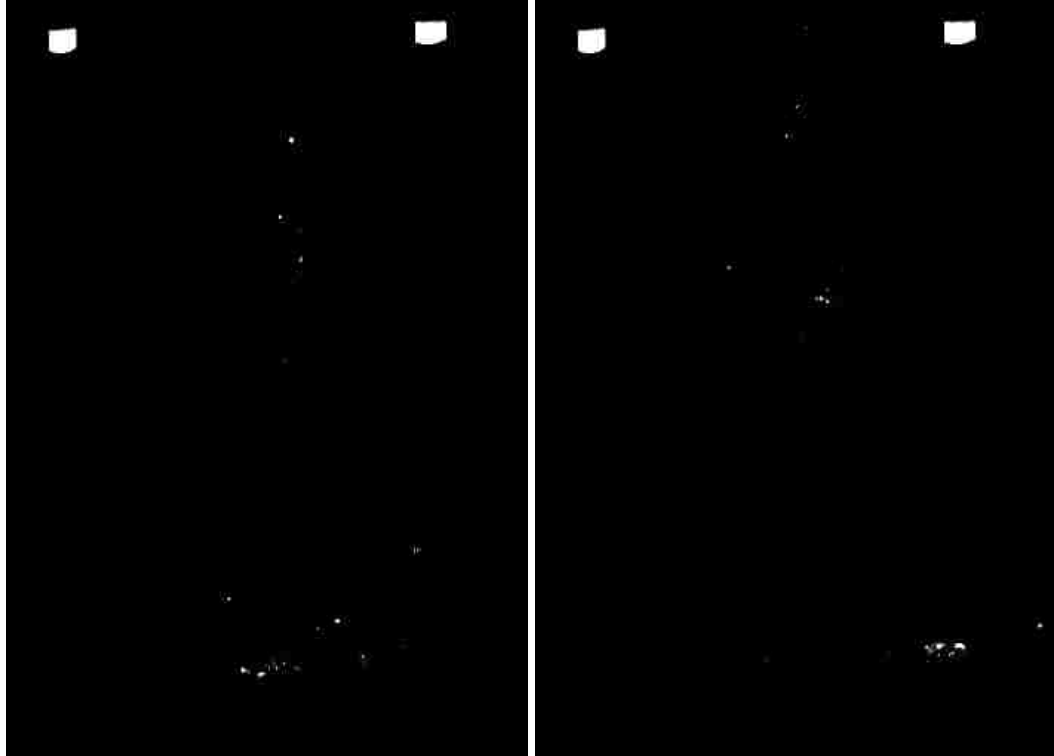


Figure 5.8. 48 ms – Evaporation (Left: Without flow, Right: With flow)

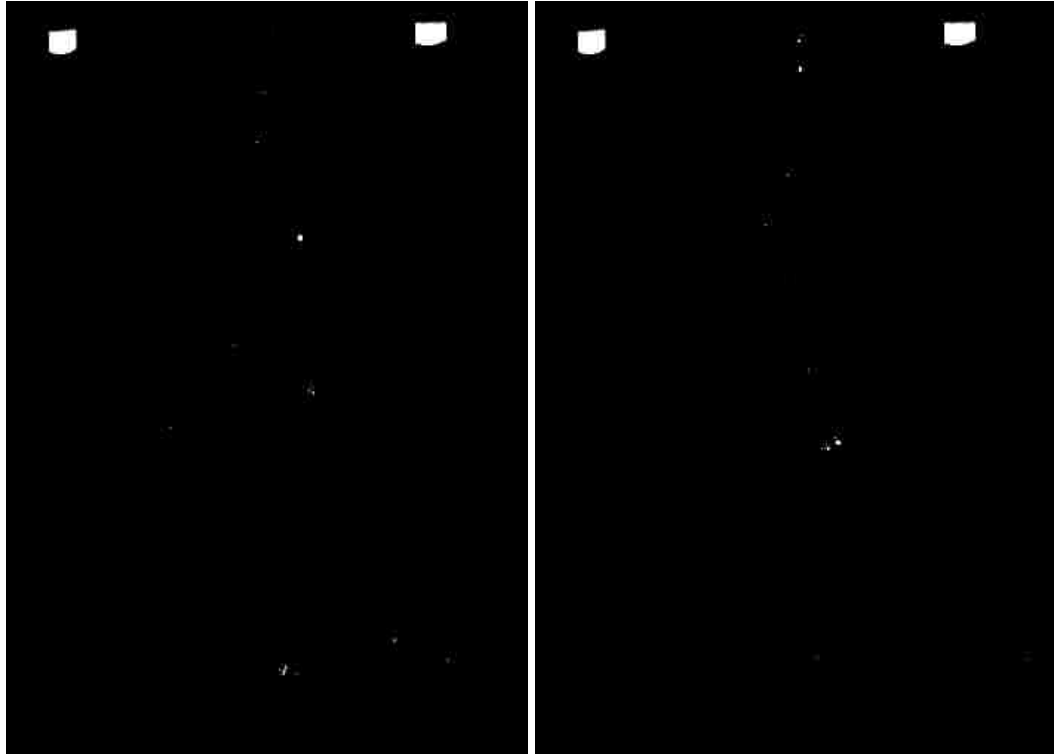


Figure 5.9. 54 ms – Evaporation (Left: Without flow, Right: With flow)

5.1.2. Back lit imaging

Back illumination technique provided a clearer view of the injector tip and the base of the chamber (Figure 5.10 to Figure 5.17). In Figure 5.12 and Figure 5.13, the difference in the shape of the cone with and without the flow can be seen. The breakup began earlier and nearer to the injector tip when there was flow. A significant number of particles were observed near the bottom of the chamber. They were found to be of two types. The first type of particles was part of the original spray breakup and had a downward trajectory of motion. The second type of particles had hit the chamber bottom and bounced back with an upward trajectory. It was also observed that some particles combined to form larger particles. The final breakup of the liquid sheet at the end of the spray was only marginally faster with flow (Figure 5.14).

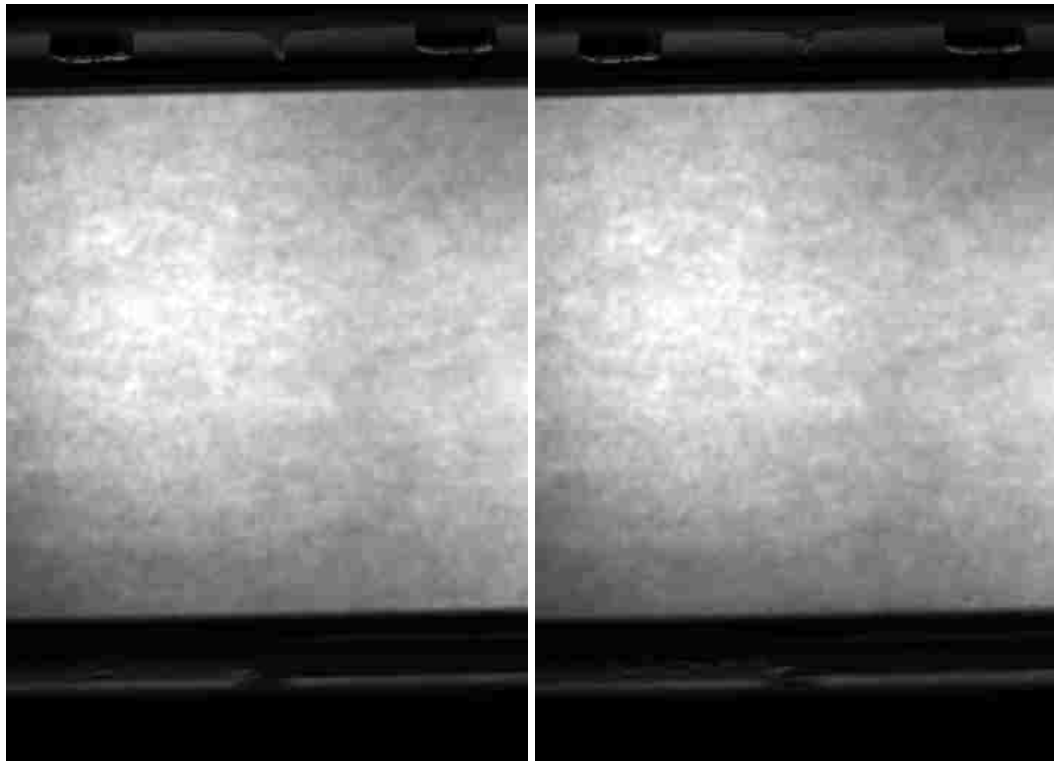


Figure 5.10. 6 ms – First appearance of liquid (Left: Without flow, Right: With flow)

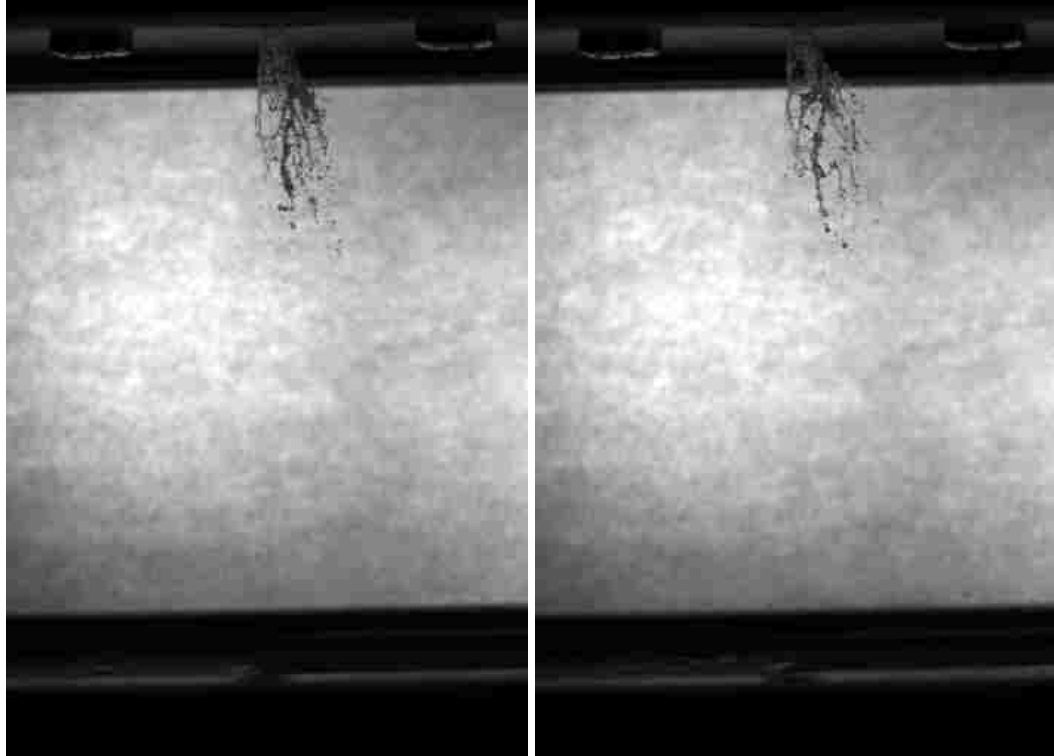


Figure 5.11. 12 ms – Development of cone (Left: Without flow, Right: With flow)

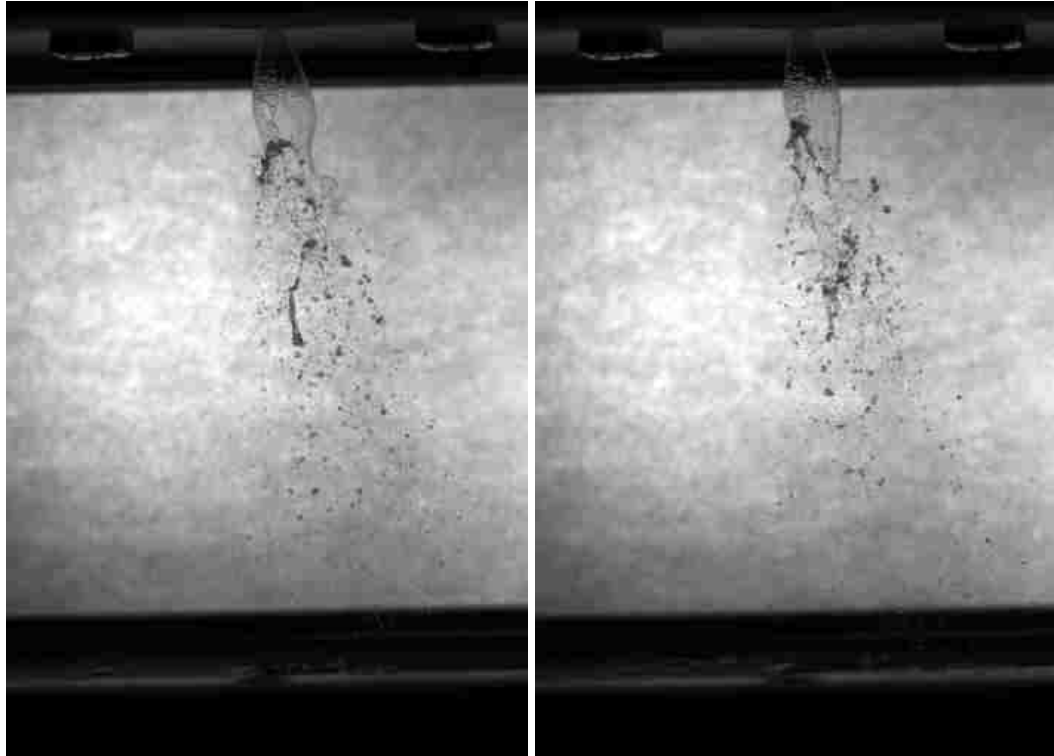


Figure 5.12. 18 ms – Cone formation (Left: Without flow, Right: With flow)

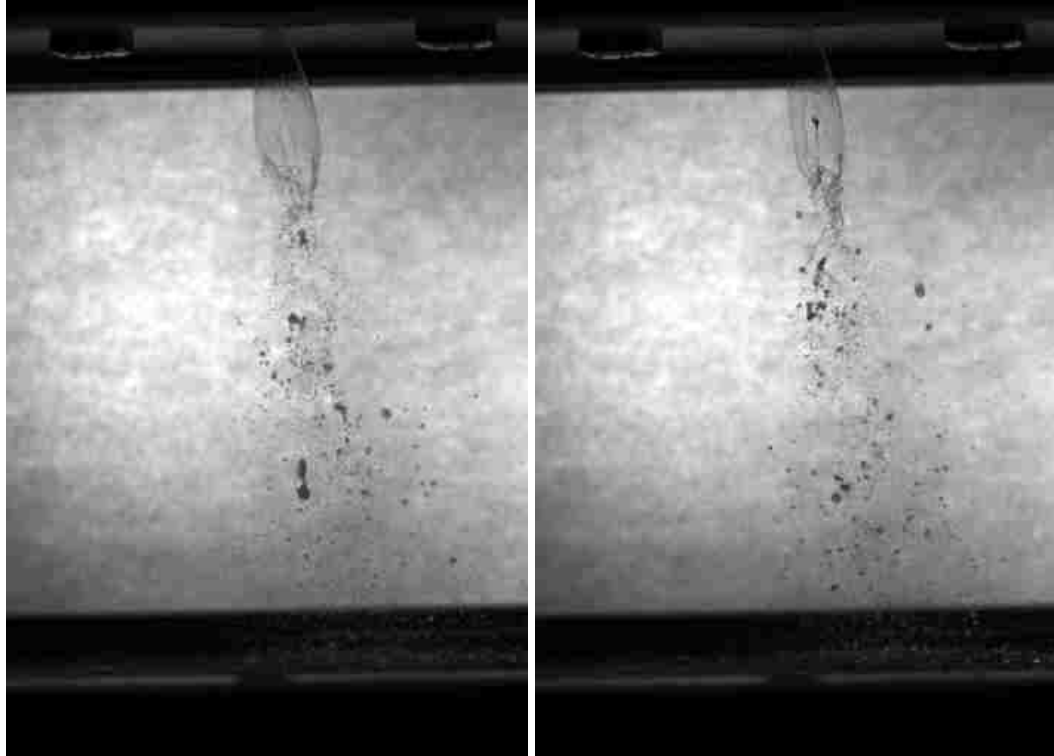


Figure 5.13. 24 ms – Cone breakup (Left: Without flow, Right: With flow)

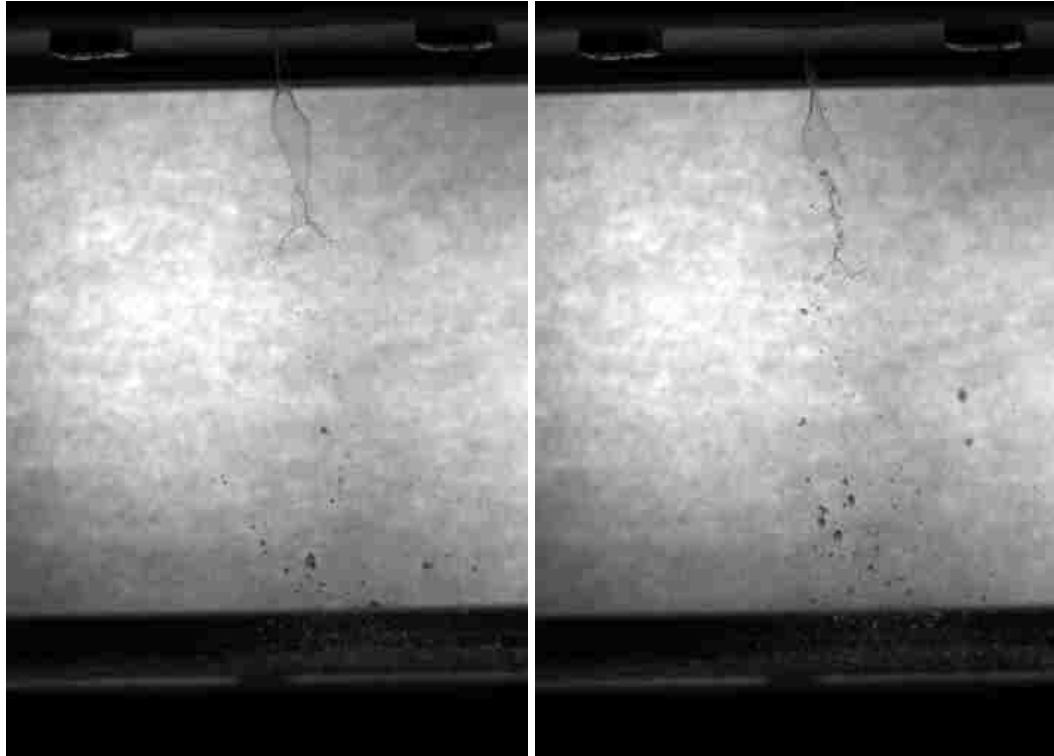


Figure 5.14. 30 ms – Breakup and end of spray (Left: Without flow, Right: With flow)

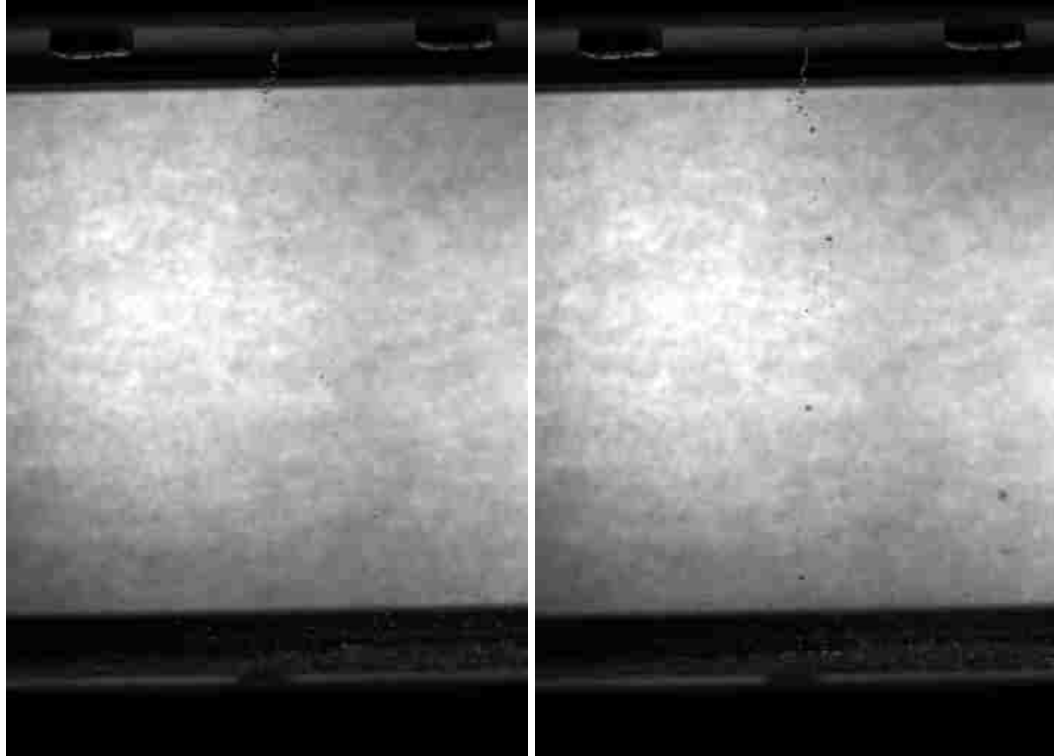


Figure 5.15. 36 ms – Evaporation (Left: Without flow, Right: With flow)

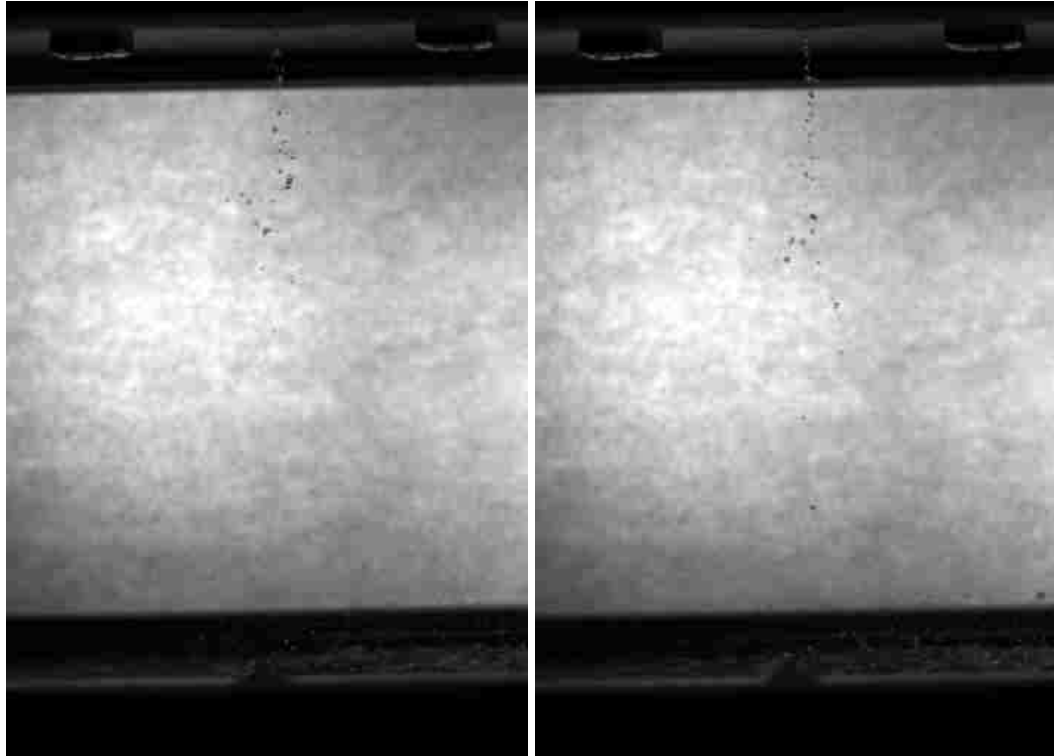


Figure 5.16. 42 ms – Evaporation (Left: Without flow, Right: With flow)

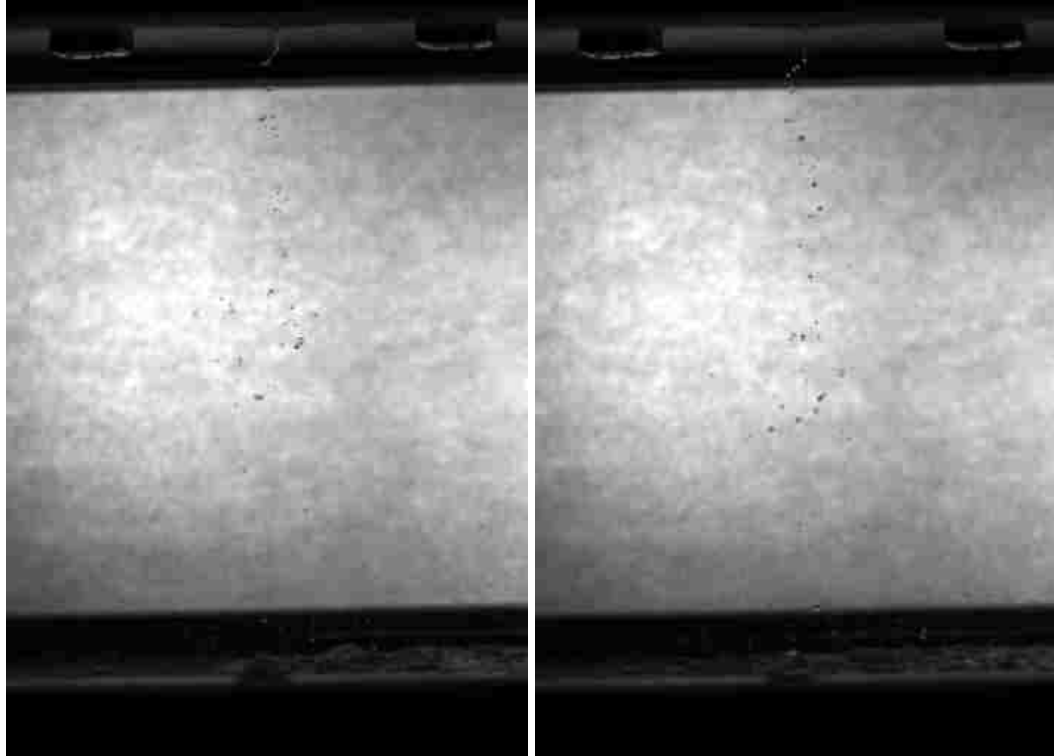


Figure 5.17. 48 ms – Evaporation (Left: Without flow, Right: With flow)

5.2. Phase Doppler Anemometry Tests with Water as Test Liquid

PDA tests with water as the test liquid and heated air flow were performed. The coordinate system for measurement (Section 4.4) is briefly described once again. Measurements were made at the center of the chamber on the injector axial plane with $Y=0$ (Figure 4.10). The X-coordinate corresponded to the direction of flow with the center of the injector at $X=0$. Measurement points were located from $X=-40$ (40 mm upstream from the injector) to 310 mm downstream from the injector at every 10 mm interval. The vertical travel was from $Z=0$ (25 mm from injector tip) to $Z=70$ (95 mm from the injector tip) at every 10 mm interval. The data has been represented in two ways. First is the time based analysis. When a droplet passes through the measurement volume, apart from the velocity and the diameter, it also gets a time stamp. This time stamp is the time period between the injection trigger and the droplet entering the measurement volume. The frequency of the injection is 2 Hz, so the time stamp resets every 500 ms with the start of each injection. By using the start of the injection as the trigger, the liquid

flow could be characterized into discrete time bins of 25 ms each with 20 time bins in total. The mean diameter and mean velocity for each bin could be determined. The second way was to analyze the particle diameter or velocity in a given time bin of interest.

5.2.1. Time based results for X-direction sweep

For the X-direction sweep, the Z-coordinate was fixed and two or more X-components were compared.

Figure 5.18 shows the particle count for Z=30 which is approximately the center height of the chamber. It was observed that as the horizontal distance from the injector increased, the particle count went down. The peak particle count also shifted later in time since the spray took longer to reach the measurement volume.

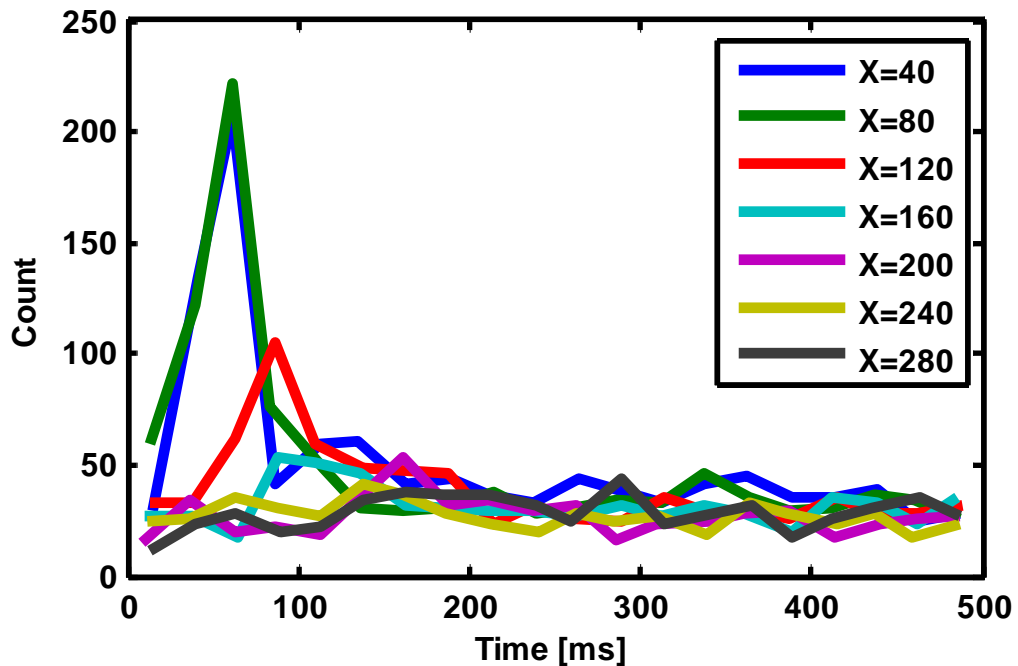


Figure 5.18. Particle count at Z=30

The particle count was plotted for Z=0, the closest vertical distance to the injector (Figure 5.19). Three bands of increasing particle count can be identified. The first is at X=40 which is the closest horizontal distance from the injector, where the particle count was very low. This was due to the conical shape of the spray, with few particles expected just

downstream of the injector near the top. The second band with slightly higher count from $X=80$ to $X=160$ indicated more particles moving towards the top of the chamber with increasing horizontal distance from the injector. The third band from $X=200$ to $X=280$ showed similar trend. The variation of particle count with respect to time was small which led to the conclusion that the particles measured near the top of the chamber are background particles from earlier sprays.

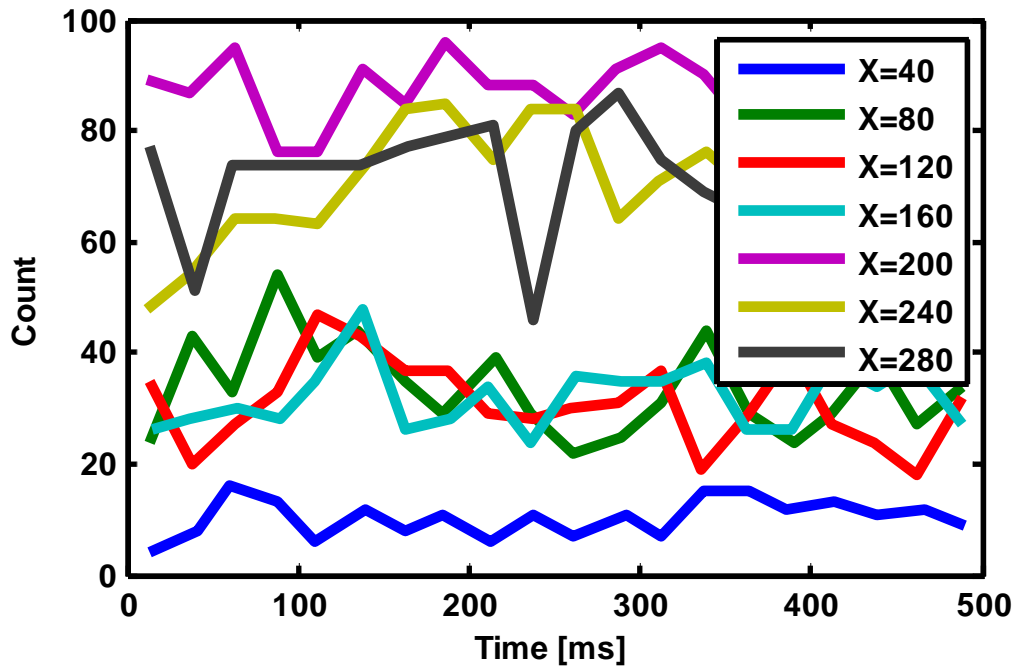


Figure 5.19. Particle count at $Z=0$

Near the bottom of the chamber, at $Z=70$, the same X -coordinates were studied (Figure 5.20). It was found that with increasing horizontal distance from the injector, the particle count increased rapidly, reaching a maximum at $X=120$, then subsequently decreased. CFD results and high speed imaging had led to a prediction of a region of high particle density near the bottom of the chamber as well. It was concluded that the region $X=120$ to $X=160$, near the bottom of the chamber, is the region of highest particle density. The peaks also indicate that the spray reaches this region between 50 to 100 ms after the start of injection. At $X=280$, there was relatively little variation of particle count with respect to time but more importantly, the particle count itself was very small, in the range of 20

to 80 over the entire vertical span. It can be concluded that at this distance most of the particles had either evaporated or settled on the chamber walls.

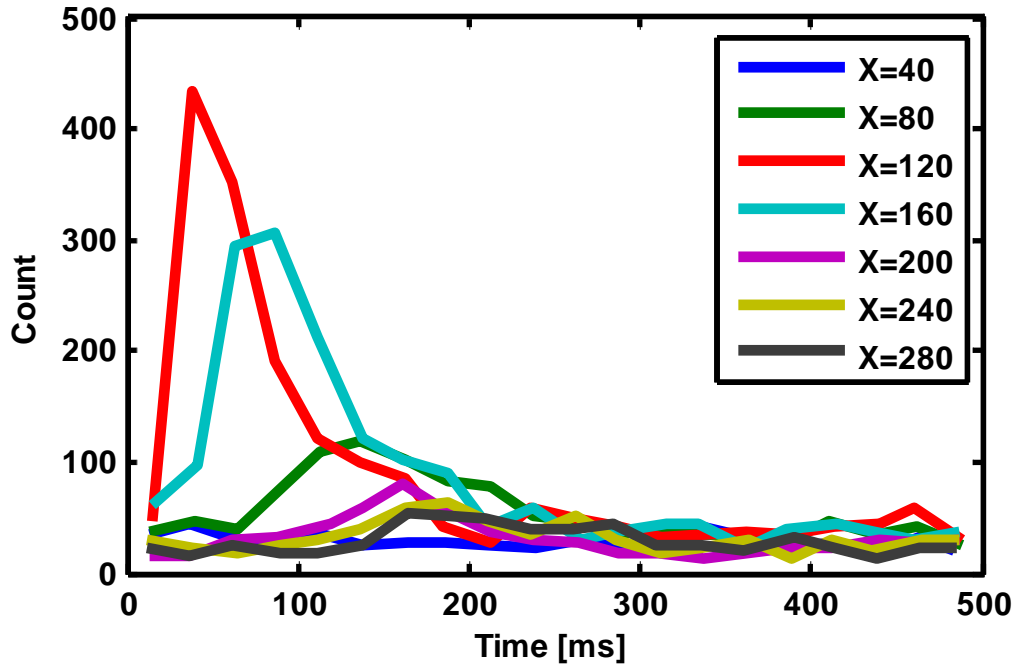


Figure 5.20. Particle count at Z=70

In Figure 5.21, the mean diameters for three X-coordinates with particle counts higher than 100 near the bottom of the chamber (Z=70) have been plotted over time. It was found that most of the droplets reach this region between 40 -120 ms after the start of injection. The mean diameter reduced with increasing horizontal distance from the injector to as low as 30 μm in the 50-100 ms time period. The mean velocity of the particles in the same time period was in the range of 2-8 m/s showing an initial decreasing trend with increasing horizontal distance (Figure 5.22). After that, the values of mean diameter and velocity increased, and all X-coordinates had similar values at the later time bins. This was deemed to be caused by the background particles. The background would be made of particles which can remain suspended for the longest time – that is, these particles are expected to have a high momentum. Consequently, the diameters would be higher. Particles having horizontal velocities in the direction of the air flow would be expected to slow down even less. The maximum velocity in the

horizontal direction (positive X-direction) was 40 m/s. This was of the order of the maximum velocities predicted by the simulations. It was believed that these high speed particles did not lose much of their original velocity or mass, and became part of the background. However, the number of such background particles was very low. Their effect became more pronounced in the later time bins (450-500 ms) when the statistical implication of the injection event was expected to be lowest. In this time period, for all coordinates, the horizontal velocity plots seemed to converge in the 15-20 m/s range and the diameter plots seemed to converge in the 150 μm range. The approximate mean speed of the particles – 15 m/s, was much higher than the air flow velocity of 1.4 m/s, since these particles retained most of the kinetic energy from the injection. The two possible reasons for increasing diameter with time could be particle coalescence or selective evaporation of smaller particles. However, there was insufficient evidence to conclusively prove either. So, it was inferred that the background particles have a mean diameter of 150 μm and mean velocity of 15 m/s. The statistical analysis of the flow at a particular point on the measurement plane should be limited to the time bin in which the peak particle count was observed so as to disregard the effects of the background particles.

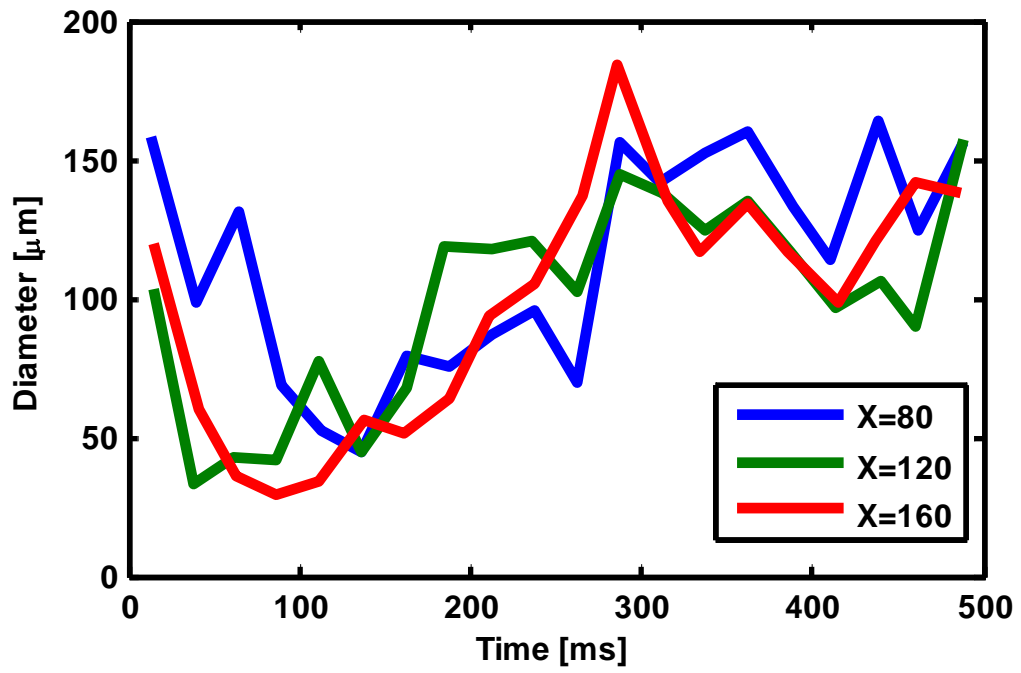


Figure 5.21. Particle mean diameter at $Z=70$

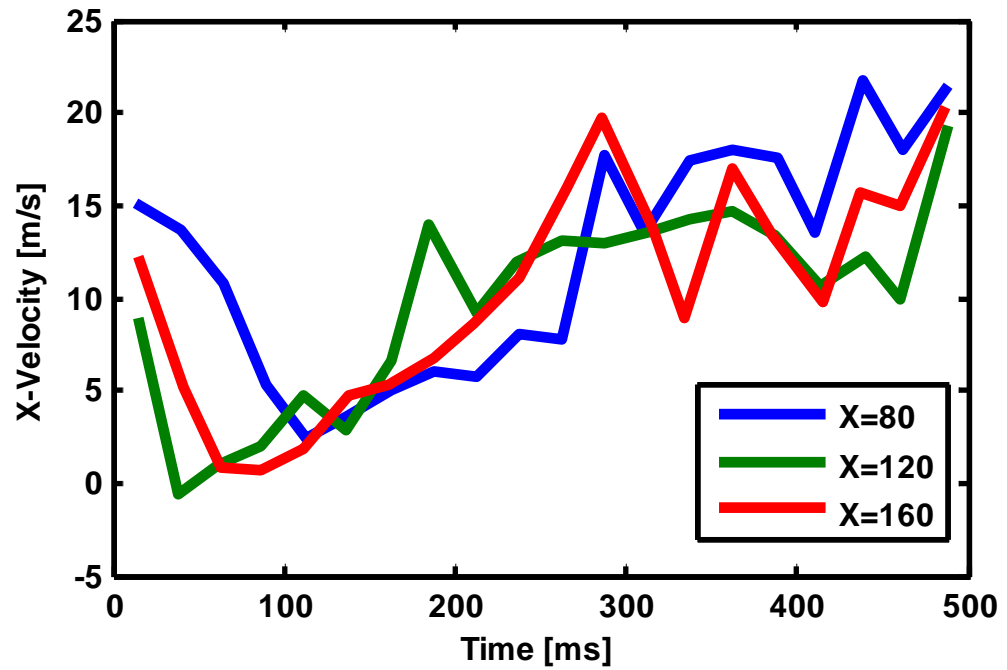


Figure 5.22. Particle mean horizontal velocity at $Z=70$

5.2.2. Time based results for Z-direction sweep on the injector axis

Measurements were made on the injector axis ($X=0$) and the results here show the two extreme Z-coordinates. In Figure 5.23, the arrival of the spray can be determined by the sharp rise in particle count at approximately 32 ms after the start of injection. At $Z=70$, the count was much lower and the diameter was uniformly distributed over time (around $150\ \mu\text{m}$, Figure 5.24) suggesting presence of background particles discussed earlier. One reason for the initial low count near the bottom of the chamber was the hollow conical nature of the spray. Most of the particles on the axis were near the center of the chamber as seen in Figure 5.25, between $Z=10$ to $Z=50$

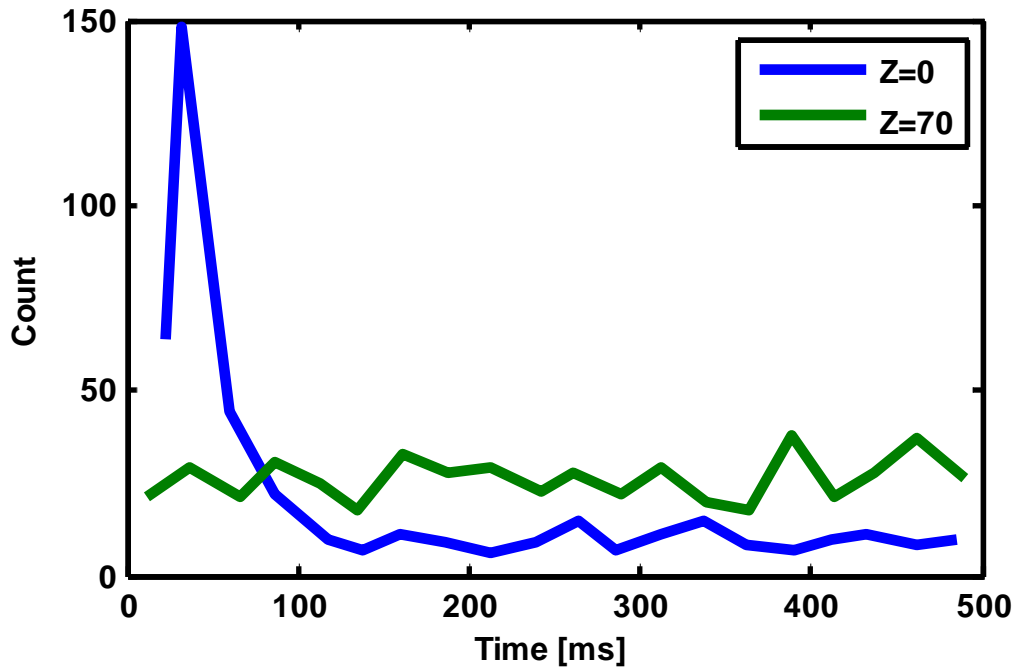


Figure 5.23. Particle count at $X=0$ for $Z=0$ and $Z=70$

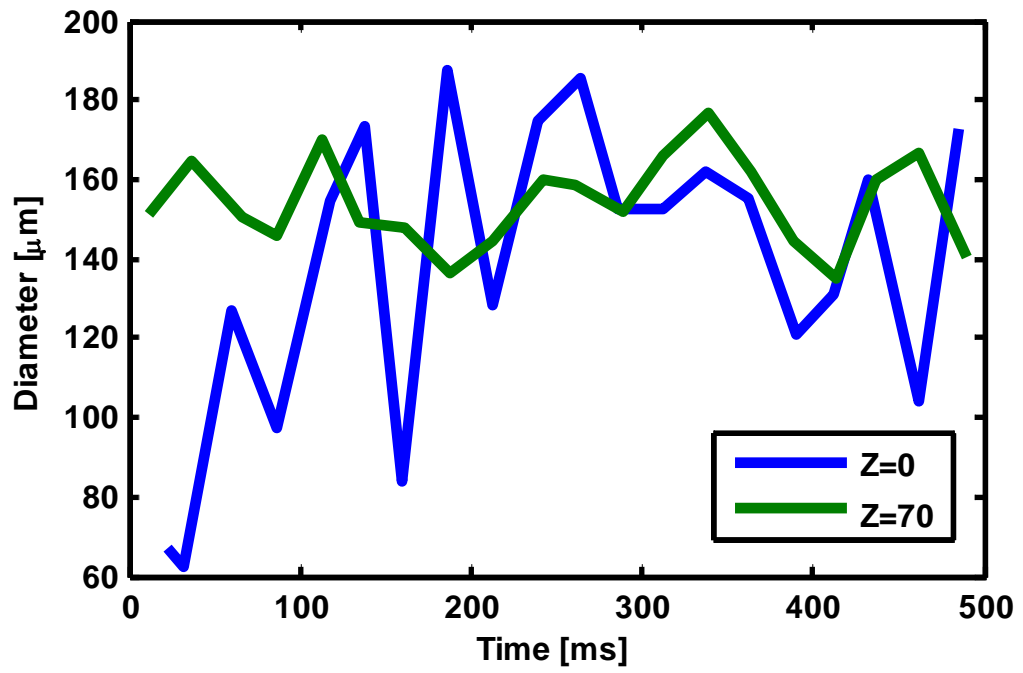


Figure 5.24. Particle mean diameter at X=0

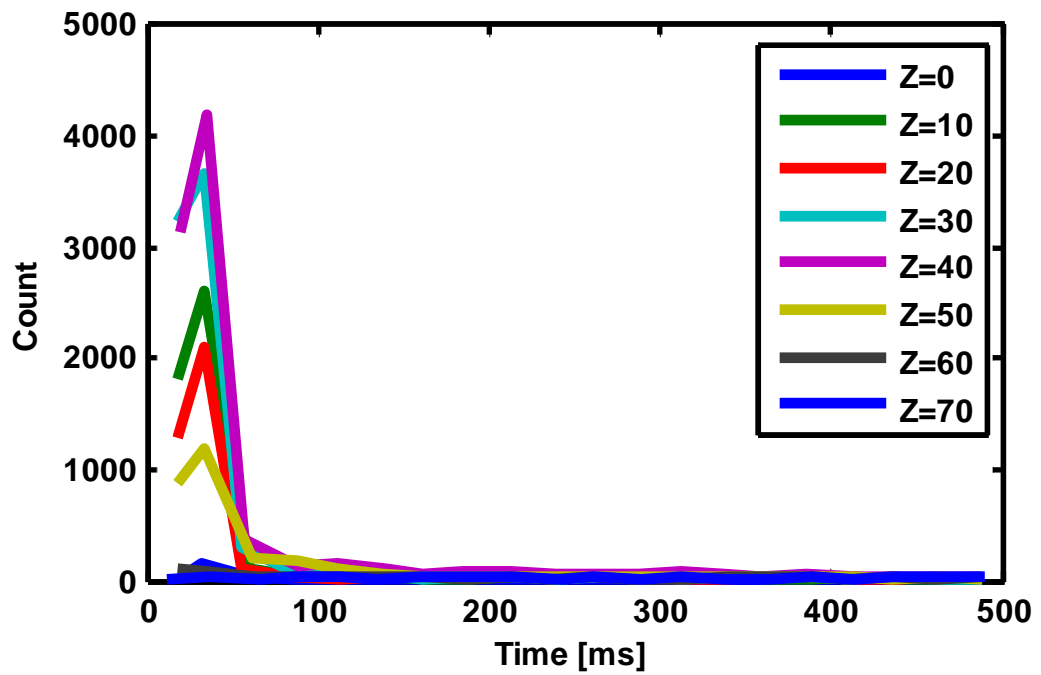


Figure 5.25. Particle count at X=0

5.2.3. Velocity distribution

The analyses in Sections 5.2.1 and 5.2.2 were used to identify the time bins in which the spray reaches a particular measurement point. In the following figures, the ‘Fraction of Particles’ is the ratio of the number of particles in one particular velocity bin divided by the total number of particles and expressed as a percentage. The velocity bin size is 1 m/s.

By 24 ms, it could be seen, in Figure 5.13 (high speed image) and Figure 5.25, that there were a large number of particles in the center of the spray. The velocity of the particles in the horizontal direction (X-direction) at the injector axis (X=0) was analysed for the first time bin of 0-25 ms at three vertical positions (Figure 5.26) with high particle count. The mean velocities at the three locations were approximately 3.3 m/s, 3 m/s, and 3.9 m/s.

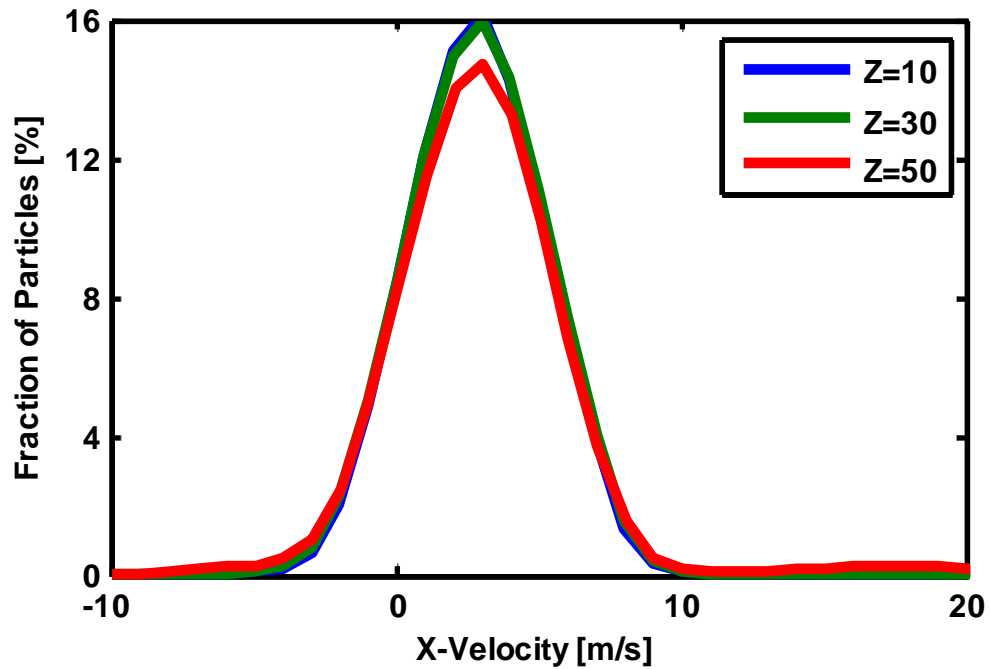


Figure 5.26. Horizontal velocity distribution at X=0 and time bin #1

The spray reached X=40 at the third time bin of 50-75 ms (Figure 5.18). The velocity of particles in the horizontal direction was analysed at the third time bin for three Z-positions at X=40 (Figure 5.27). The mean horizontal velocities at the three locations were approximately 5.3 m/s, 3.7 m/s, and 5.5 m/s.

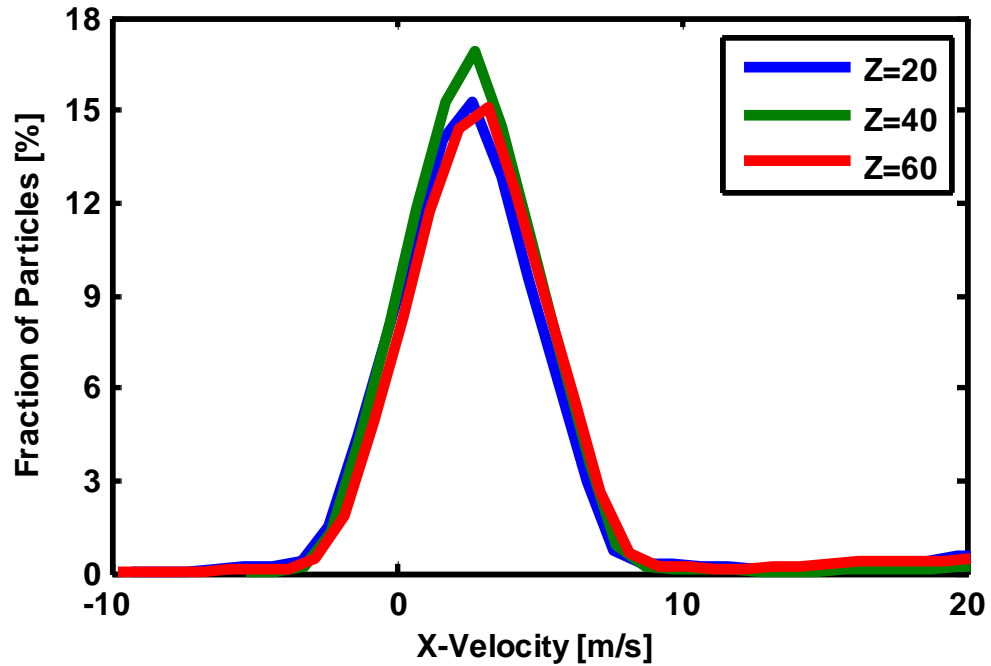


Figure 5.27. Horizontal velocity distribution at X=40 and time bin #3

The spray reached X=80 in the third time bin (50-75 ms) as well (Figure 5.18). The mean horizontal velocity with increasing X-coordinate is shown in Figure 5.28 in the third time bin. With increasing vertical distance from the injector, the mean velocity decreased. This could be the effect of the boundary layer of gas near the bottom of the chamber moving slower and not accelerating the particles as much. With increasing horizontal distance, the mean velocity increased at Z=20, since the particle count decreased with the shift of particles from the top of the chamber to the bottom. From X=80 to X=90, the drop in mean velocity at Z=40 indicated a rise in particle count, but X=90 onwards, started increasing, signaling a further vertical shift in particles in the chamber. Consequently, at Z=60 level, there was a sharp drop in mean velocity beyond X=100 to approximately 4 m/s. In Figure 5.29, the distribution of mean horizontal velocity at X=80, X=120 and X=160 is shown for Z=70 at the fourth time bin (75-100 ms). The mean velocity was 8.5, 5.5 and 4.1 m/s respectively.

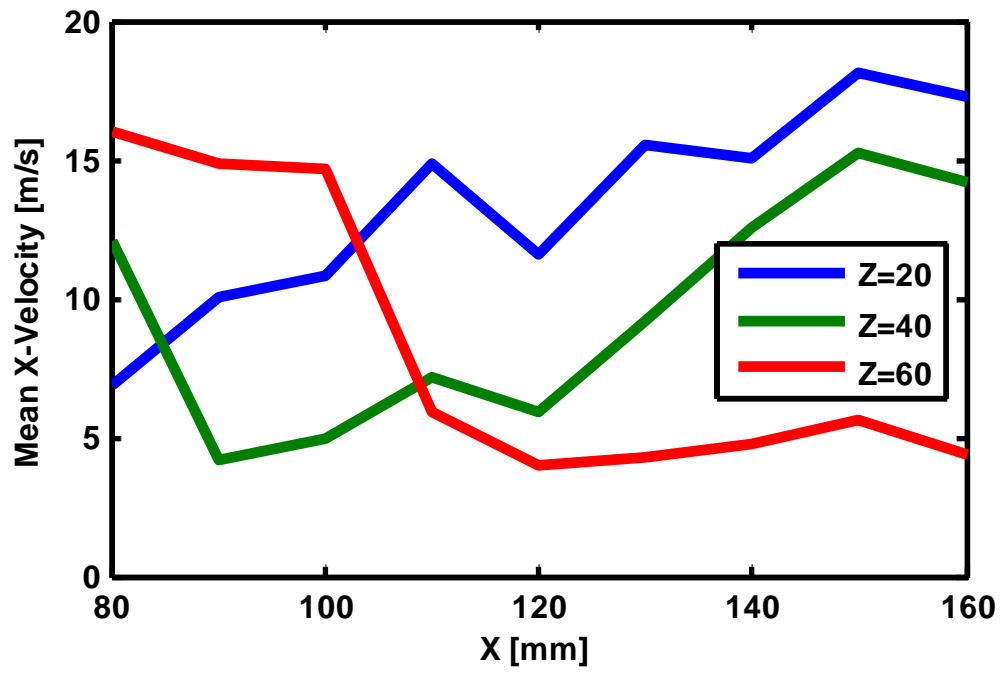


Figure 5.28. Mean horizontal velocity vs. X-coordinate at time bin #3

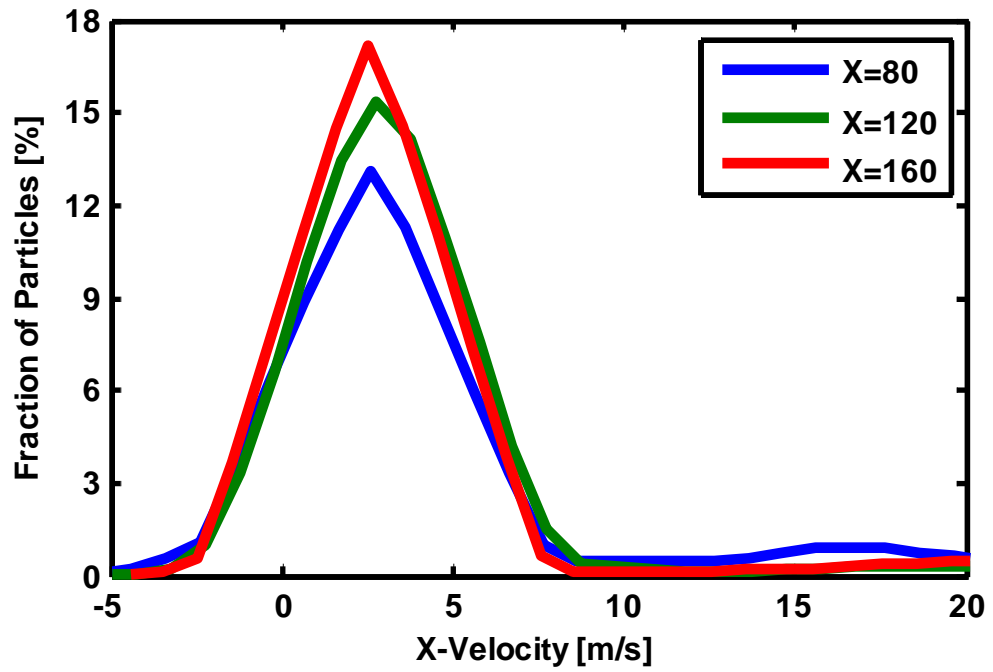


Figure 5.29. Mean horizontal velocity distribution at Z=70 and time bin #4

5.2.4. Diameter distribution

Figure 5.30 to Figure 5.32 show the change in particle mean diameter with increasing horizontal distance from the injector axis at three vertical distances from the injector ($Z=20$, $Z=40$ and $Z=60$). The time bins were chosen based on the estimated arrival of spray at that horizontal distance (Figure 5.18). From $X=0$ to $X=40$, the mean particle size was approximately $30\ \mu\text{m}$ for the two upper levels. At that height, points inside or outside the cone had very few particles and most of them were small particles that were part of the background. For $Z=60$, the mean diameter of particles closest to the bottom of the chamber reduced in diameter from 160 to $55\ \mu\text{m}$. However, these particles were most likely part of the background as well owing to the low count (Section 5.2.2).

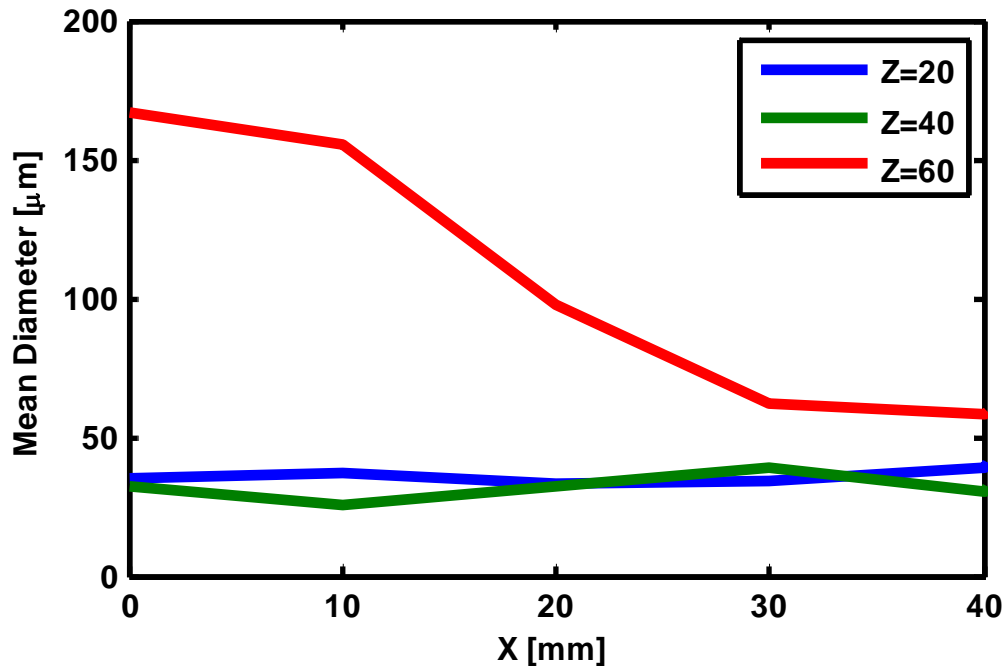


Figure 5.30. Particle mean diameter vs. X-coordinate at time bin#3

From $X=40$ to $X=100$, the particles of the spray were numerous enough to be considered in the statistical analysis. This led to an initial increase in the particle diameters. The overall change in mean diameters for the three Z -coordinates was minimal. Mean particle diameters were of the order of $100\ \mu\text{m}$ and $30\ \mu\text{m}$ respectively.

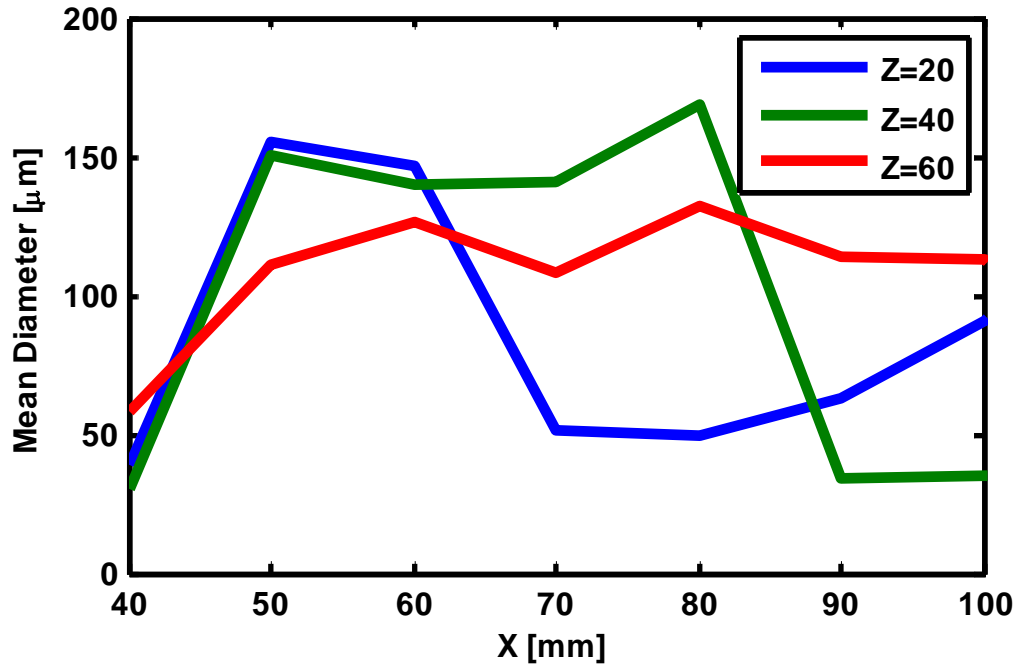


Figure 5.31. Particle mean diameter vs. X-coordinate at time bin#3

In Figure 5.32, the reduction in mean diameter can be observed for all Z-coordinates from X=100 to X=130. The lowest mean diameters observed for Z=20, Z=40 and Z=60 are 70, 40 and 40 μm respectively. The mean diameter was found to increase with increasing horizontal distance. However, the particle count dropped considerably after X=130. So, the increase in the mean diameter was attributed to the statistical deviation produced by the background particles and should be disregarded.

It can be concluded that evaporative effects were responsible for the reduction in particle size of approximately 22% at Z=20 (90 to 70 μm), 33% at Z=40 (60 to 40 μm), and 55% at Z=60 (90 to 40 μm) between the horizontal distance of 100 and 130 mm. The time bin, the particle count and the mean diameter were used to estimate the liquid mass remaining at a particular vertical level from X=100 to X=130. It was found that approximately 18%, 80% and 33% of liquid mass remained at Z=20, Z=40 and Z=60 respectively. Beyond X=200, the particle count was too low for analysis.

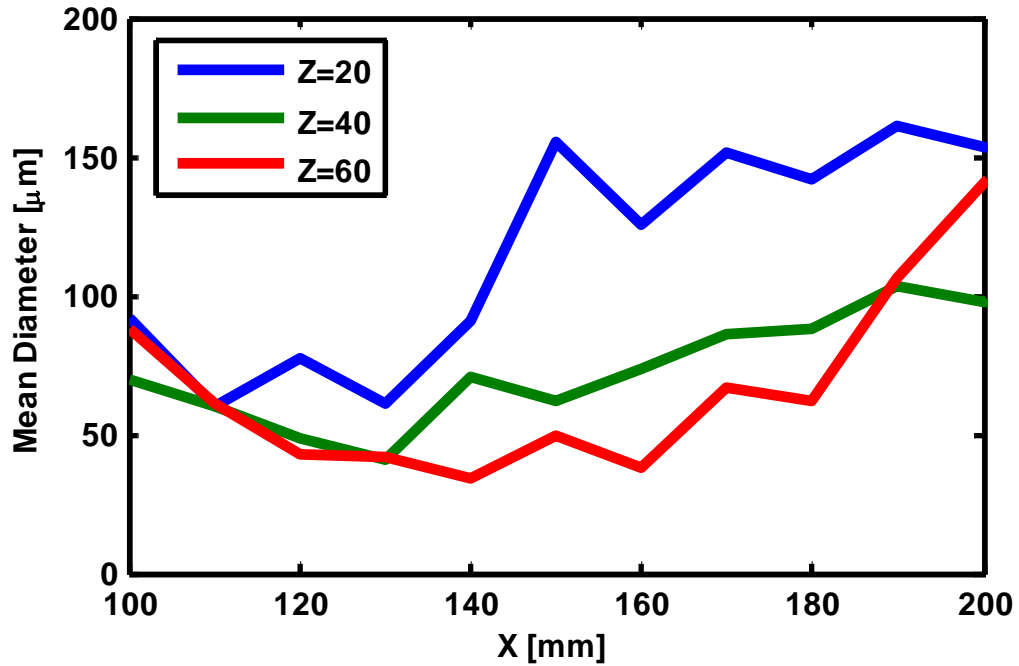


Figure 5.32. Particle mean diameter vs. X-coordinate at time bin#4

5.2.5. Vertical velocity

The vertical velocity (in the Z-direction) was measured as well. However, beyond X=120, the number of particles travelling in the Z-direction were too few for statistical analysis (Figure 5.33).

The Z-velocity distribution at X=30 for three vertical positions is plotted in Figure 5.34 at the third time bin of 50-75 ms. The mean velocities were approximately 4.3 m/s, 4.6 m/s, and 5 m/s. At X=60, in the third time bin (Figure 5.35), the mean velocities were approximately 4.3 m/s, and 4.4 m/s. The Z=20 level was disregarded due to the low particle count. For both Figure 5.34 and Figure 5.35, the plots were drawn using a velocity bin size of 1 m/s. Till X=60, the same trend of increasing velocity, or particle acceleration was observed with increasing vertical distance from the injector. Park *et al.* observed a similar phenomenon of increasing vertical mean velocity with increasing vertical distance from the injector [25]. They identified the flow field of the air in the

cross-flow direction as the cause. Furthermore, as the Z-coordinate increased, the measurement volume was further outside the hollow cone structure and captured more recently formed particles and higher velocity background particles.

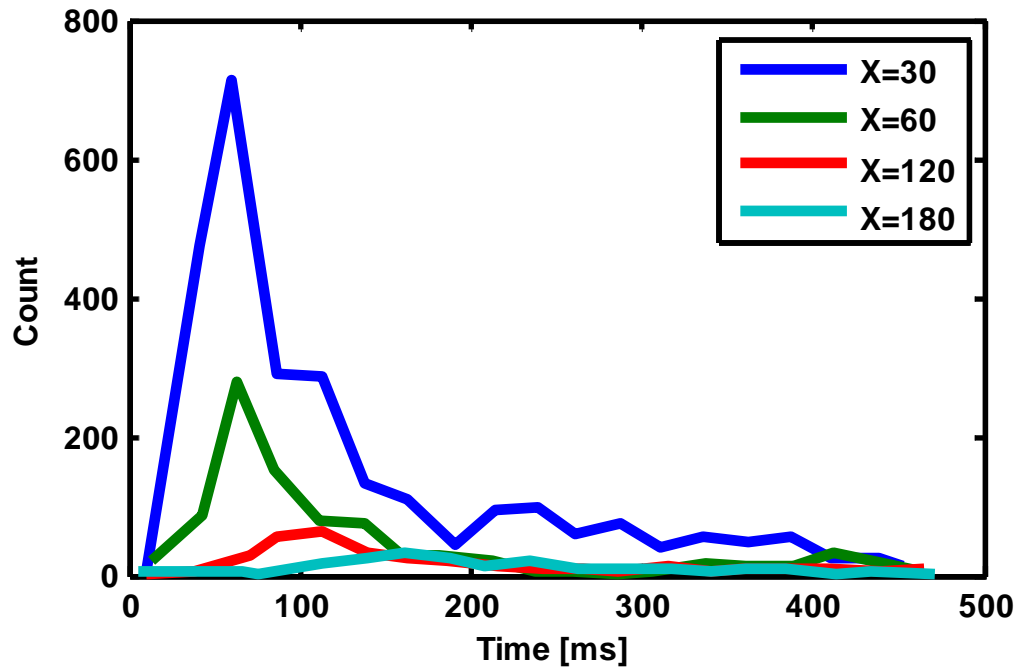


Figure 5.33. Particle count for Z-component at Z=50

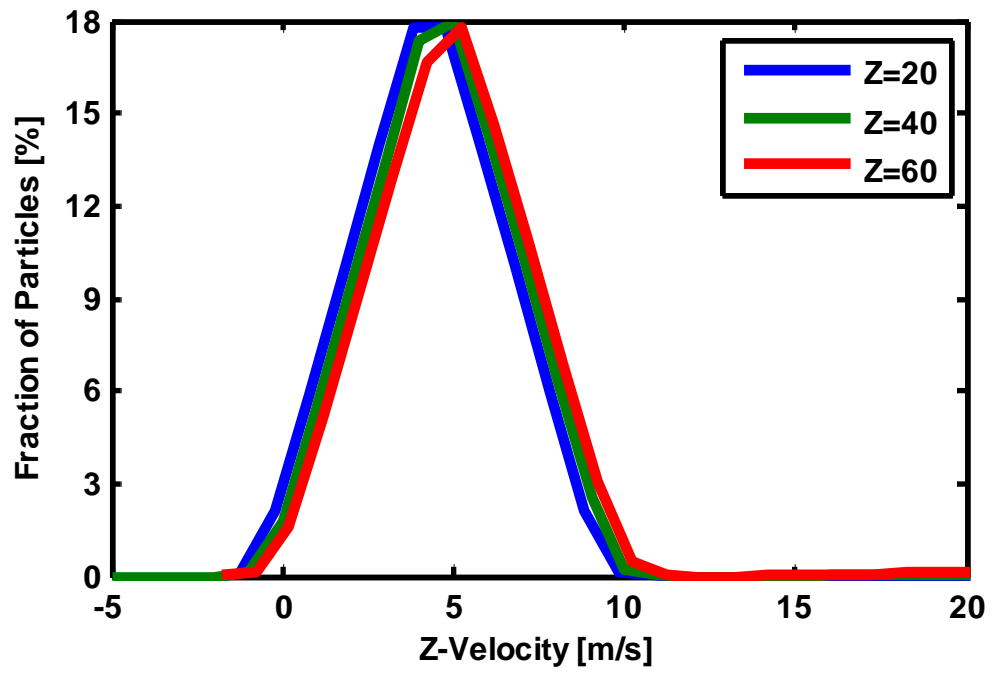


Figure 5.34. Z-velocity distribution at X=30 and time bin #3

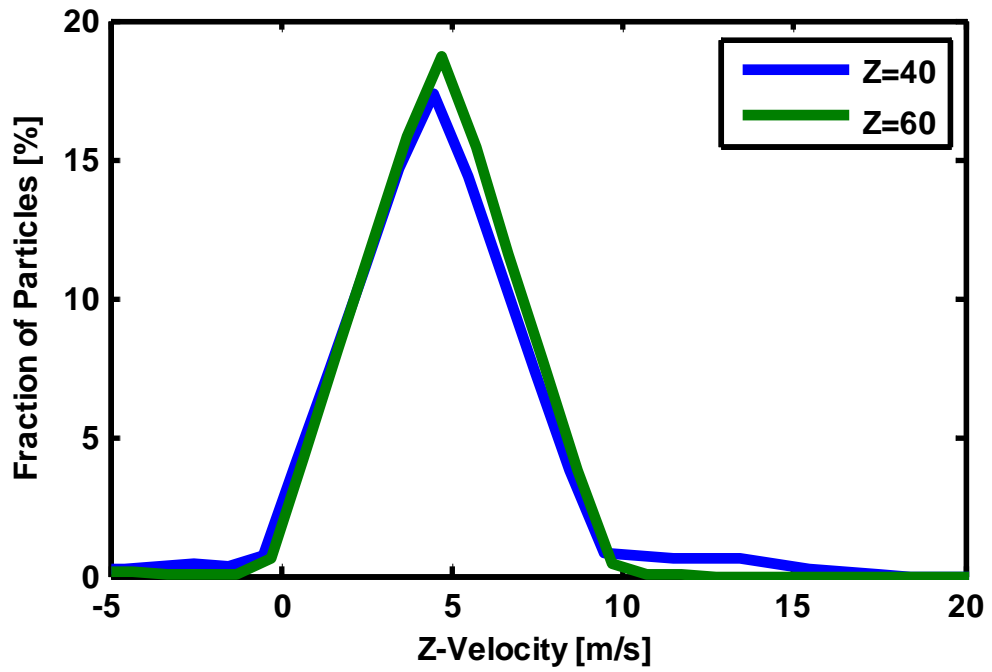


Figure 5.35. Z-velocity distribution at X=60 and time bin #3

5.3. Phase Doppler Anemometry Tests with Diesel as Test Liquid

Injection tests were performed under static conditions at an injection pressure of 6 bar gauge without air flow. PDA measurements were made at $Z=75$ (100 mm from the injector tip) on the injector axis ($X=0$). The diameter and vertical velocity distributions are shown in Figure 5.36 and Figure 5.37 respectively. The plots were drawn with a bin size of 1 μm and 1 m/s respectively. The mean diameter of particles was 77 μm and the SMD was 150 μm . These were substantially higher than the simulation predictions (Figure 3.3 and Figure 3.21). This could be attributed to the fact that the tests were conducted at room temperature which would decrease the rate of evaporation significantly. The simulation velocity predictions were higher, with a mean vertical velocity as measured by the PDA at 3.5 m/s (compared to Figure 3.19). Most particles had a vertical velocity in the 2-8 m/s range which was consistent with the simulation calculations.

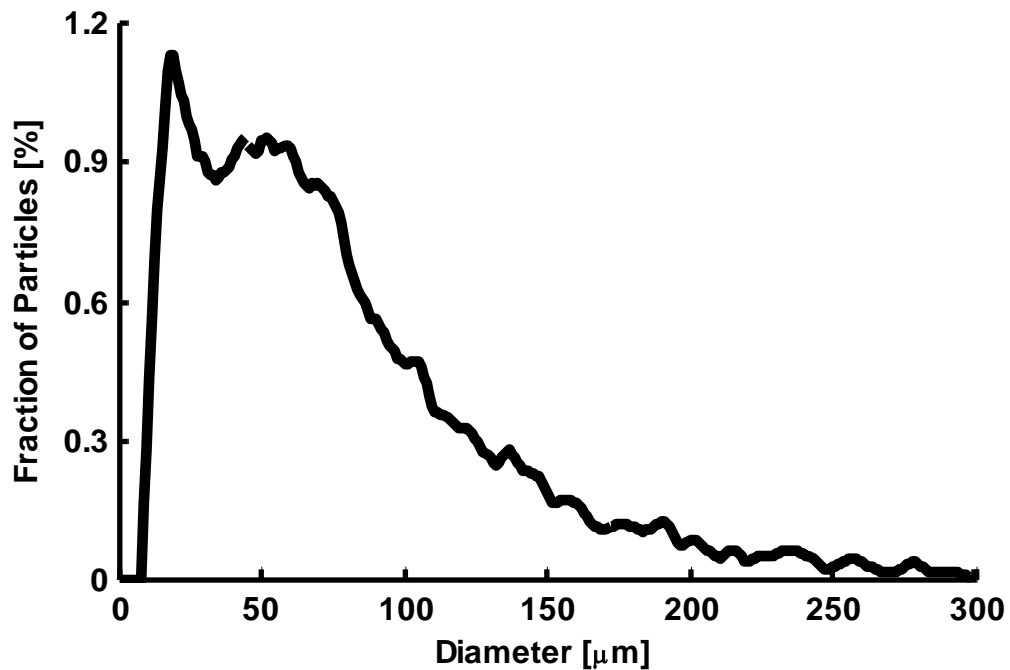


Figure 5.36. Diesel PDA result – particle diameter distribution

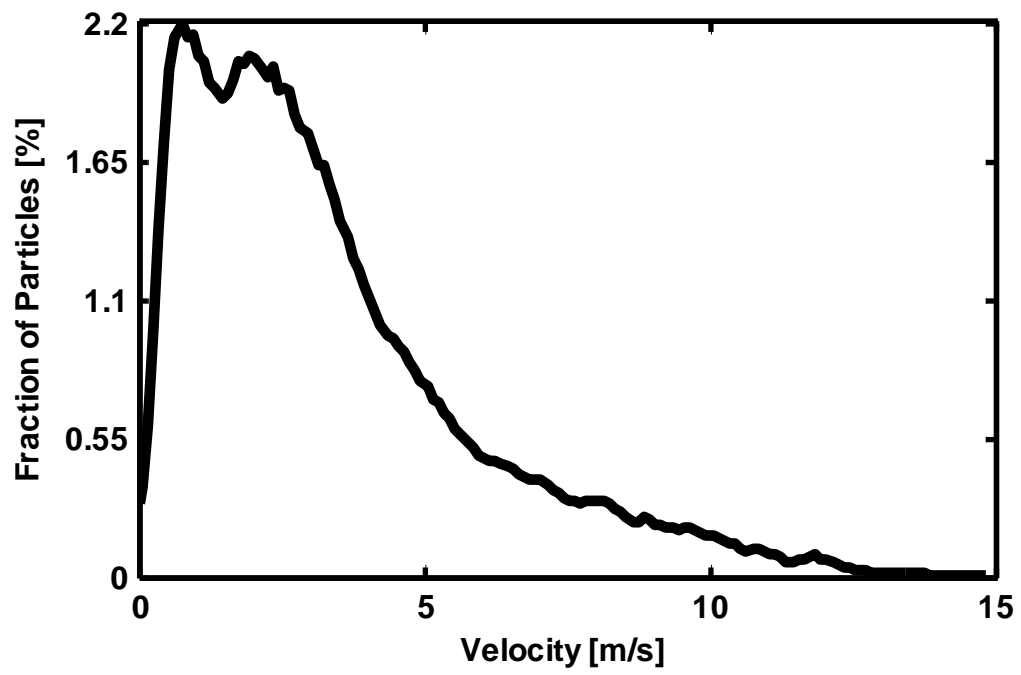


Figure 5.37. Diesel PDA result – particle Z-velocity distribution

6. CONCLUDING REMARKS

6.1. Summary of Results

The effect of the cross-flowing exhaust on the spray breakup, dispersion and evaporation on an after-treatment fuel injector was investigated. A numerical analysis and simulation studies were performed to get an estimate of the droplet lifetime, diameters and velocities. High speed imaging was used to study the spray breakup and dispersion, due to the effect of the cross-flow of gas. Phase Doppler anemometry was used to study the spray diameter and velocity distribution. The results are summarized below.

Numerical analysis using classic evaporation model –

- The evaporation constant for two given hydrocarbon fuels – n-heptane and diesel fuel-2 (DF-2) under different ambient temperatures was calculated. With increasing temperature, the value of the steady state evaporation constant increased. For n-heptane, the droplet lifetime (for the drop to lose 90% of its initial mass) reduced by approximately 45% when the temperature increased from 423 to 523 K. For DF-2, the reduction in droplet lifetime was approximately 78% over the same temperature range.
- The droplet lifetime was used to estimate the distance over which a droplet would evaporate given the flow velocity.

Simulation study using CONVERGE –

- With increasing mass flow rates, a change in the spray pattern was predicted but there was no significant change in the droplet diameter distribution.
- For all the simulation conditions, the entire liquid mass was predicted to have evaporated 100 mm downstream from the injector axis.
- With increasing temperature, the mean diameter and the number of spray particles reduced.
- The fastest particles were near the injector tip followed by a few near the chamber bottom. By the time the spray reached the middle of the chamber, most of the particles had lost 60-80% of the velocity in the horizontal flow direction.

- The Sauter Mean Diameter (SMD) showed a predictive trend of decreasing SMD with increasing air mass flow rate – indicating faster evaporation.

High speed imaging –

- Two illumination techniques were used to view the injection event without and with flow. There were distinct differences in the spray breakup and dispersion. The liquid sheet formed a hollow cone which collapsed and broke up into smaller particles. The breakup was observed to be faster with flow.
- Particles were observed near the bottom of the chamber which had bounced off the base.

PDA tests with water –

- PDA flow tests with water showed the expected trend of decrease in number of particles with increasing distance from the injector in both horizontal and vertical direction outside the spray cone.
- Regions of high particle density in the center and bottom of the chamber were identified.
- A reduction in particle diameters was observed with increasing distance from the injector axis in both horizontal and vertical directions.
- It was found that particles had negligible vertical velocities beyond 120 mm horizontal distance from the injector axis.
- The vertical velocity of the particles was found to increase marginally with increasing vertical distance from the injector tip.

PDA tests with diesel –

- Tests with diesel fuel, but without flow, showed diameters were greater than the simulation results using the diesel surrogate n-heptane. The velocity measurements were in better agreement with the simulation results.

6.2. Future Scope of Work

The following investigations were suggested to take this study forward –

- Use diesel as the test liquid for flow tests
- Quantify the evaporation of diesel
- Investigate the spray under higher temperatures and higher flow rates to simulate greater engine loads
- Explore different injector mounting designs to enhance evaporation
- Adapt the experimental setup for Schlieren imaging so as to enable viewing of the liquid vapors.

REFERENCES/BIBLIOGRAPHY

1. “CAFE - Fuel Economy,” National Highway Traffic Safety Administration, Accessed from <http://www.nhtsa.gov/fuel-economy>, July 24, 2013
2. “2017–2025 Model Year Light-Duty Vehicle GHG Emissions and CAFE Standards: Supplemental Notice of Intent,” NHTSA–2010–0131, Federal Register / Vol. 76, No. 153 / Tuesday, August 9, 2011 / Proposed Rules, Accessed from <http://federal.eregulations.us/rulemaking/document/NHTSA-2010-0131-0093>, July 24, 2013
3. “Light-Duty Vehicle, Light-Duty Truck, and Medium-Duty Passenger Vehicle -- Tier 2 and Interim Non-Tier 2 Supplemental Federal Test Procedure Exhaust Emission Standards,” United States Environmental Protection Agency, Accessed from <http://www.epa.gov/otaq/standards/light-duty/tier2interimstds.htm>, July 24, 2013
4. “Zero Emission Vehicle (ZEV) Program,” California Air Resources Board, Accessed from <http://www.arb.ca.gov/msprog/zevprog/zevprog.htm>, August 22, 2013
5. “Heavy-Duty Highway Compression-Ignition Engines And Urban Buses -- Exhaust Emission Standards,” United States Environmental Protection Agency, Accessed from <http://www.epa.gov/otaq/standards/heavy-duty/hdci-exhaust.htm>, July 24, 2013
6. Zheng, M., & Reader, G. T., “Energy Efficiency Analyses of Active Flow After-treatment Systems for Lean Burn Internal Combustion Engines,” *Energy Conversion and Management*, 45(15-16), 2473–2493, 2004
7. Johnson, T. V., “Diesel Emission Control in Review,” SAE International, 2009-01-0121, 1–12, 2009
8. Ward, J., “DOE’s SuperTruck Analysis,” SAE Government Industry Meeting, Accessed from http://www.sae.org/events/gim/presentations/2013/ward_jacob.pdf, August 15, 2013

9. Jeftic, M., “A Long Breathing Lean NO_x Trap for Diesel After-treatment Supplemental Energy Reduction,” Master of Applied Science Thesis, Department of Mechanical, Automotive and Materials Engineering, University of Windsor, 2011
10. Russell, A., & Epling, W. S., “Diesel Oxidation Catalysts,” *Catalysis Reviews*, 53(4), 337–423, 2011
11. Mathieu, O., Lavy, J., & Jeudy, E., “Investigation of Hydrocarbons Conversion Over a Pt-Based Automotive Diesel Oxidation Catalyst: Application to Exhaust Port Fuel Injection,” *Topics in Catalysis*, 52(13-20), 1893–1897, 2009
12. Neeft, J. P. A., Makkee, M., & Moulijn, J. A., “Review article – Diesel Particulate Emission Control,” *Fuel Processing Technology*, 47(96), 1–69, 1996
13. Konstandopoulos, A. G., & Papaioannou, E. , “Update on The Science and Technology of Diesel Particulate Filters,” *KONA Powder and Particle Journal*, 26, 36–65, 2008
14. Birkhold, F., Meingast, U., & Wassermann, P., “Analysis of the Injection of Urea-Water-Solution for Automotive SCR DeNO_x-Systems : Modeling of Two-Phase Flow and Spray / Wall-Interaction,” *SAE International*, 2006-01-06, 1-13, 2006
15. Yi, Y., “Development of a 3D Numerical Model for Predicting Spray , Urea Decomposition and Mixing in SCR Systems,” *SAE International*, 2007-01-3985, 1–13, 2007
16. Nakatsuji, T., Yasukawa, R., Tabata, K., Ueda, K., & Niwa, M., “Catalytic Reduction System of NO_x in Exhaust Gases from Diesel Engines with Secondary Fuel Injection,” *Applied Catalysis B: Environmental*, 17(4), 333–345, 1998
17. Bamber, D. W., Ambrose, S. L., & McCarthy, J. E., Jr, “Fuel Injector Optimization for Diesel After-treatment Systems Coupled with Exhaust After-treatment System Performance on a Heavy-duty Diesel Engine Powered Vehicle,” *SAE International*, 2010-01-1940, 1-19, 2010
18. “Converge 1.4.1 User Guide & Reference,” Convergent Science Incorporated, Middleton, Wisconsin, USA

19. "Measurement Principles of PDA," Dantec Dynamics, Accessed from <http://www.dantecdynamics.com/Default.aspx?ID=1058>, August 15, 2013
20. Lefebvre, A. H., "Atomization and Sprays," Hemisphere Publishing Corporation, New York, USA, ISBN 0-89116-603-3, 309-366, 1989
21. Husted, B. P., Petersson, P., Lund, I., Holmstedt, G., "Comparison of PIV and PDA Droplet Velocity Measurement Techniques on Two High-pressure Water Mist Nozzles," *Fire Safety*, 44, 1030-1045, 2009
22. Nishida, K., Gao, J., Manabe, T., & Zhang, Y., "Spray and Mixture Properties of Evaporating Fuel Spray Injected by Hole-type Direct Injection Diesel Injector," *International Journal of Engine Research*, 9(4), 347–360, 2008
23. Daviault, S. G., Matida, E. A., Karakolis, M. M., Webster, G. D., "Droplet Size and Velocity Characteristics of the Ignition Quality Tester (IQTTM) Fuel Spray," *SAE International*, 2011-01-1816, 2011
24. Kitamura, Y., & Takahashi, T., "Stability of a Liquid Jet in Air Flow," *Journal of Chemical Engineering of Japan*, (6), 282–286, 1975
25. Park, S. W., Kim, S., & Lee, C. S., "Breakup and Atomization Characteristics of Mono-dispersed Diesel Droplets in a Cross-flow Air Stream," *International Journal of Multiphase Flow*, 32(7), 807–822, 2006
26. Jeong, H., Lee, K., & Ikeda, Y., "Investigation of the Spray Characteristics for a Secondary Fuel Injection Nozzle Using a Digital Image Processing Method," *Measurement Science and Technology*, 18(5), 1591–1602, 2007
27. Chin J. S., Durrett R. R., & Lefebvre A. H., "The Interdependence of Spray Characteristics and Evaporation History of Fuel Sprays," *Journal of Engineering for Gas Turbines & Power*, 106(3), 639-644, 1984
28. Abramzon, B., & Sirignano, W. A., "Droplet Vaporization Model for Spray Combustion Calculations," *International Journal of Heat and Mass Transfer*, 32(9), 1605–1618, 1989

29. Chrigui, M., Sadiki, A., Janicka, J., Hage, M., Dreizler, A., “Experimental and Numerical Analysis of Spray Dispersion and Evaporation in a Combustion Chamber,” *Atomization and Sprays*, 19(10), 929-955, 2009
30. Kryukov, A. P., Levashov, V. Y., & Sazhin, S. S., “Evaporation of Diesel Fuel Droplets: Kinetic Versus Hydrodynamic Models,” *International Journal of Heat and Mass Transfer*, 47(12-13), 2541–2549, 2004
31. Godsave, G. A. E., “Studies of the Combustion of Drops in a Fuel Spray: The Burning of Single Drops of Fuel,” *Proceedings of the Combustion Institute* 4, 818-830, 1953
32. Spalding, D. B., “The Combustion of Liquid Fuels,” *Proceedings of the Combustion Institute* 4, 847-864, 1953
33. “Bosch Departronic 2,” Accessed from http://www.bosch-automotivetechnology.com/media/db_application/downloads/pdf/antrieb/en_3/DS_Sheet_Departronic2_Diesel_Dosing_System_20120718.pdf, June 25, 2013
34. “Bosch Denoxtronic 2,” Accessed from http://www.bosch-automotivetechnology.com/media/db_application/downloads/pdf/antrieb/en_3/DS_Sheet_Denoxtronic2-2_Urea_Dosing_System_20120718~1.pdf, June 25, 2013
35. “Phantom v7.3,” Accessed from <http://www.visionresearch.com/Products/High-Speed-Cameras/v73/>, August 15, 2013
36. “BSA Flow Software v5.00 User’s Guide,” Dantec Dynamics

APPENDIX A: MATLAB code for calculation of steady state evaporation constant

```

clear all
a=15.52;
b=5383;
P=101.33; %amb pressure in Kpa
Ma=28.97; %mol. mass of air in g/mol
Mf=198; %mol. mass of fuel in g/mol
Tinf=2000; %ambient temp in K
Tcrf=725.9; %critical temperature of fuel
Tbnf=536.4; %boiling temperature at normal atmospheric pressure
Lt_bn=254000; %latent heat of vaporization at normal boiling
temperature
rho_f0=846; %density of fuel
data=zeros(1,1); %data storage array defined
i=1; %counter
for Ts=300:0.1:Tbnf %surface temp of fuel in K
% BM (mass transfer number) calculation
Pf_s=exp(a-(b/(Ts-43))); %vapor pressure from Clausius-Clapeyron in Kpa
Yf_s=(1+(((P/Pf_s)-1)*(Ma/Mf)))^(-1); %fuel mass fraction surface
Bm=Yf_s/(1-Yf_s); % mass transfer number

% BT (heat transfer number) calculation
Yf_r=(2/3)*Yf_s; %fuel mass fraction reference
Ya_r=1-Yf_r; %air mass fraction reference
Tr=Ts+((1/3)*(Tinf-Ts)); %reference temperature
cp_a=k_air_calculation(Tr); %specific heat of air, call function i,
Kelvin
cp_v=(363+(0.467*Tr))*(5-(0.001*rho_f0)); %specific heat of fuel vapor
in J/kgK
cp_g=(Ya_r*cp_a)+(Yf_r*cp_v); %specific heat of air-vapor mixture at
constant pressure
L=Lt_bn*((Tcrf-Ts)/(Tcrf-Tbnf))^-0.38; %latent heat
Bt=(cp_g*(Tinf-Ts))/L; % heat transfer number
data(i,1)=Ts;
data(i,2)=Bm;
data(i,3)=Bt;
i=i+1;
end

%plot figure to get the intersection point of Bm and Bt
figure(1);
plot(data(:,1),data(:,2))
hold all
plot(data(:,1),data(:,3))
%%

T=520.9; %intersection point obtained from plot
Ts=T;
Pf_s=exp(a-(b/(Ts-43))); %vapor pressure from Clausius-Clapeyron in Kpa
Yf_s=(1+(((P/Pf_s)-1)*(Ma/Mf)))^(-1); %fuel mass fraction surface
Bm=Yf_s/(1-Yf_s); %transfer number

```

```

% BT calculation
Yf_r=(2/3)*Yf_s; %fuel mass fraction reference
Ya_r=1-Yf_r; %air mass fraction reference
Tr=Ts+((1/3)*(Tinf-Ts));
cp_a=k_air_calculation(Tr); %specific heat of air, call function i,
Kelvin
cp_v=(363+(0.467*471))*(5-(0.001*rho_f0)); %spec heat of fuel vapor in
J/kgK
cp_g=(Ya_r*cp_a)+(Yf_r*cp_v); % specific heat of vapor-gas mixture
L=Lt_bn*((Tcrf-Ts)/(Tcrf-Tbnf))^-0.38; %latent heat
Bt=(cp_g*(Tinf-Ts))/L;

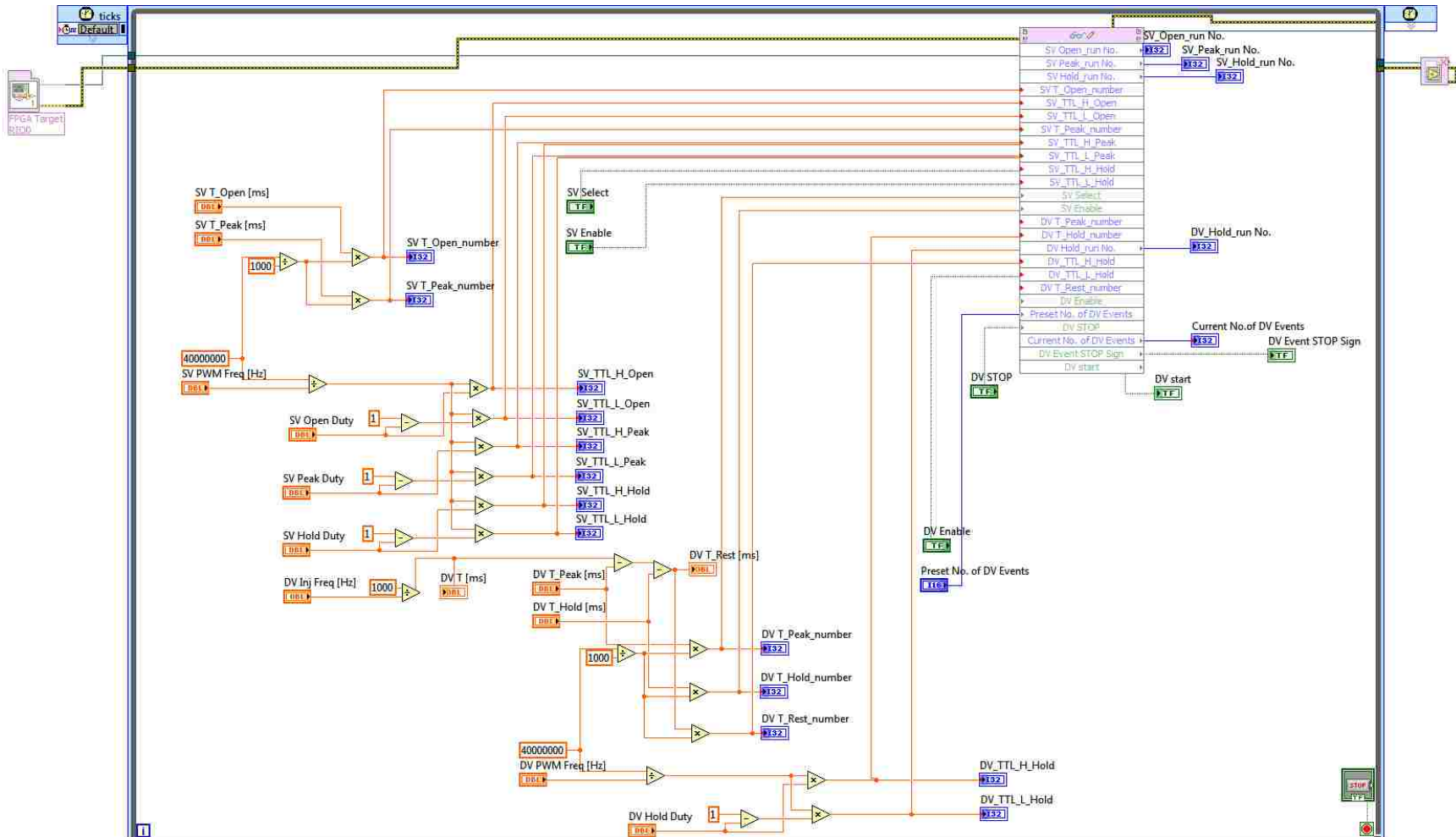
B=Bm;
C_ex=8.24e-4; %coefficient of thermal expansion
%calculate fuel density
rho_ft=rho_f0*(1-(1.8*C_ex*(T-288.6))-(0.090*((T-288.6)^2)/((Tcrf-
288.6)^2)));

n=2-(0.0372*((Tr/Tbnf)^2));
kv_t=(10^-3)*(13.2-(0.0313*(Tbnf-273)))*((Tr/273)^n); %thermal
conductivity of fuel
ka_t=conduct_calculation(Tr); %thermal conductivity of air
kg=(Ya_r*ka_t)+(Yf_r*kv_t); % thermal conductivity of vapor-gas mixture

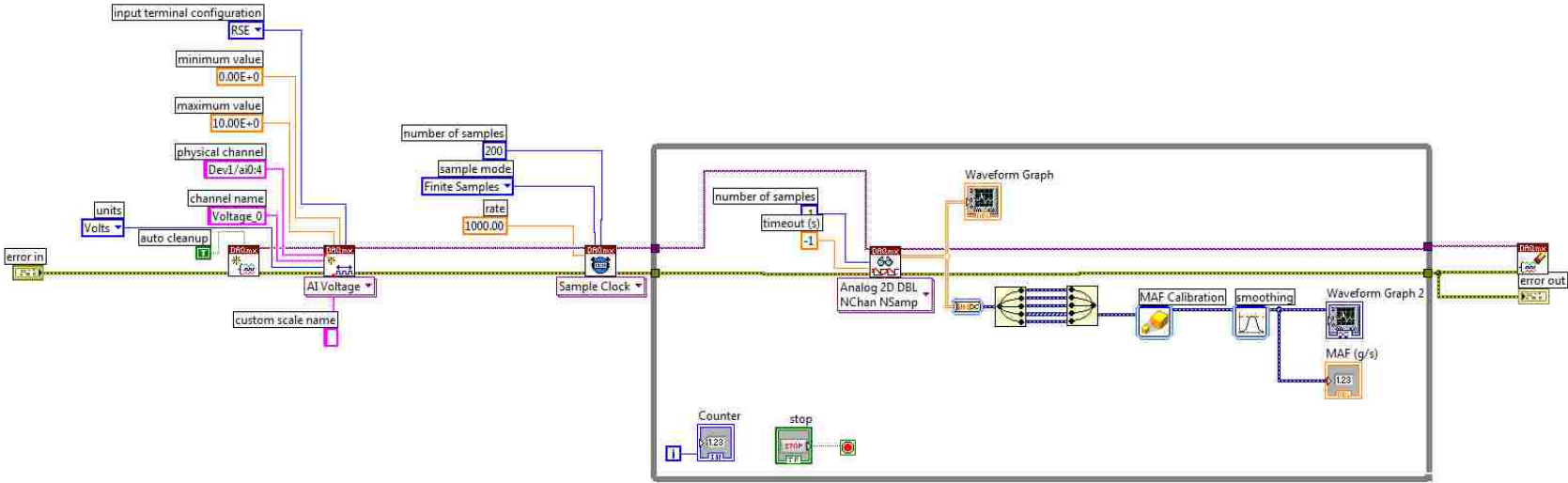
% Evaporation constant
lambda_st=(8*kg*log(1+B))/(cp_g*rho_ft)

```

APPENDIX B: Injector Driver and PDA Sync Program in LabView™



APPENDIX C: Data Acquisition Program in LabView™



VITA AUCTORIS

NAME: Shouvik Dev

PLACE OF BIRTH: Kolkata, India

YEAR OF BIRTH: 1986

EDUCATION: Bhavan's Gangabux Kanoria Vidyamandir
High School
Kolkata, India, 2004

Jadavpur University
Bachelor of Engineering
Kolkata, India, 2008

LIST OF PUBLICATIONS

Papers in Non-refereed Conference Proceedings

1. **Dev, S.**, Han, Q., Xie, K., Zheng, M., Henshaw, P., “A Study of Diesel Engine Intake Flow Field to Improve In-cylinder Air Motion,” Proceedings of Combustion Institute – Canadian Section Spring Technical Meeting, Quebec City, QC, 2013.

Poster Presentations

1. Han, Q., Divekar, P., **Dev S.**, “2nd Generation Biofuels for Sustainable Transportation,” AUTO21 HQP Conference, Montreal, QC, May 29-31, 2012
2. Divekar, P., **Dev, S.**, Grignion, D., “Flexible Operation of HCCI Combustion Using Intelligent Control,” AUTO21 HQP Conference, Montreal, QC, May 29-31, 2012
3. **Dev, S.**, Han, Q., Xie, K., “Measurement of Engine Intake Flow Field,” Green Auto Power Train –Annual General Meeting, University of Windsor, November 16, 2012
4. **Dev, S.**, “CFD Simulation to Support Diesel Engine Experimental Research,” Green Auto Power Train –Annual General Meeting, University of Windsor, November 16, 2012